A Study of Gas Hydrates with Ocean-Bottom-Seismometer data on the East Coast of Canada

by

Angela Schlesinger
Diplom, Christian-Albrechts University of Kiel, 2006

A Dissertation Submitted in Partial Fulfillment of the
Requirements for the Degree of

DOCTOR OF PHILOSOPHY

in the Department of Earth and Ocean Sciences

University of Victoria

A Study of Gas Hydrates with Ocean-Bottom-Seismometer data on the East Coast of Canada

by

Angela Schlesinger
Diplom, Christian-Albrechts University of Kiel, 2006

Supervisory Committee

Dr. Roy D. Hyndman, Co-Supervisor
(School of Earth and Ocean Sciences, University of Victoria)

Dr. George D. Spence, Co-Supervisor
(School of Earth and Ocean Sciences, University of Victoria)

Dr. Michael Riedel, Departmental Member
(School of Earth and Ocean Sciences, University of Victoria)

Dr. John Cassidy, Departmental Member
(School of Earth and Ocean Sciences, University of Victoria)

Dr. Jody Klymak, Outside Member
(Department of Physics & Astronomy, University of Victoria)

Supervisory Committee

Dr. Roy D. Hyndman, *Co-Supervisor*

(School of Earth and Ocean Sciences)

Dr. George D. Spence, *Co-Supervisor*

(School of Earth and Ocean Sciences)

Dr. Michael Riedel, *Departmental Member*

(School of Earth and Ocean Sciences)

Dr. John Cassidy, *Departmental Member*

(School of Earth and Ocean Sciences)

Dr. Jody Klymak, *Outside member*

(Department of Physics and Astronomy)

ABSTRACT

This dissertation presents a study on velocity modeling using ocean-bottom seismometer data (OBS) collected in 2004 and 2006 on the western Scotian slope. Gas hydrate and free gas concentrations and their distribution along the Scotian margin were derived based on the velocity results modeled with two different OBS data sets. A strong velocity increase (140-300 m/s) associated with gas hydrate was modeled for a depth of 220 m below seafloor (bsf). At the base of that high velocity zone (330 mbsf) the velocity decreases with 50-130 m/s. This depth is associated with the depth of the bottom-simulating reflector (BSR) observed in previous 2-D seismic reflection data. The gas hydrate concentrations (2-18 %) based on these velocities were calculated with an effective medium model. The velocity modeling shows that a sparser OBS spacing (~1 km) reveals more velocity uncertainties and smaller velocity contrasts than a denser (100 m) spaced OBS array. The results of the travel-time inverse modeling are applied in a waveform inverse modeling with OBS data in the second part of the thesis. The modeling tests were performed to obtain information on OBS instrument spacings necessary to detect low-concentration gas hydrate occurrences. The model runs show that an increase in instrument spacing leads to an increasing loss of model smoothness. However, large instrument spacings (> 500 m) are beneficial for covering a wide target region with only using a few instruments, but decreasing the lateral resolution limits of the subsurface targets. In general half of the instrument spacing defines the lower boundary for the lateral width of the target structure. Waveform modeling with the 2006 OBS data has shown that low frequencies (< 8 Hz) in the source spectrum are necessary to recover the background velocity of the model. The starting model derived from travel-time inversion of the 2006 data is not close enough to the true model. Thus the first-arrival waveforms do not match within half a cycle. Modeling with a starting frequency of 8 Hz and and applying data with a low signal-to-noise ratio (1.25) introduces artifacts into the final model result without updating the velocity.

Contents

List of Tables

List of Figures

ACKNOWLEDGEMENTS

This thesis would not have been accomplished without the help and encouragement of a number of people. First of all, I would like to thank George Spence and Roy Hyndman for taking me on as PhD student at the University of Victoria. I am thankful for their permanent support and dedication toward the completion of this work. I am grateful for the opportunities I had to visit the East coast of Canada and meet with David Mosher, Keith Louden, and Janette Cullen who were very supportive and gave me access to the data for this research study. During my first years I got enormous help in understanding Seismic UNIX and C-shell programming from Ross Haacke, who was a Postdoctoral Research Fellow with the Pacific Geoscience Center (PGC) during that time. I met many interesting people at the PGC to whom I express my profound gratitude, especially Michael Riedel and Andreas Rosenberger. Special thanks to Matthias Delescluse for helping me in the initial phase for the waveform inverse modeling. I would like to thank Gerhard Pratt and his students for offering the waveform tomography course in July 2012 and for the permission to work with the waveform inversion algorithm.

During the last six years I met people who became wonderful friends: Lionel Esteban, Iulia Stoian, Romina Gehrmann, Subbarao Yelisetti, Jane Gao, Ian Daykin, Wiebke Imsel, Bettina Müller, and Barbara Ehlting. Thank you all!

Last but not least I would like to thank my parents, Hans-Jürgen and Silvia Schlesinger, for their love and support.

My last words are to you, Martin. I am so thankful to have you by my side.

1. GENERAL INTRODUCTION

1.1 Importance of gas hydrates

Gas hydrates are ice-like configurations of water and gas molecules. The "frozen" water produces a lattice framework with open cages in which gas molecules can be trapped during the crystallization (ice formation) (e.g. *Sloan*, 1998). Interest in gas hydrates started in the early 19th century, when scientists discovered this clathrate structure of various natural gases (e.g., methane, ethane, butane; reviewed in *Ripmeester*, 2000). During the last 40 years the number of gas hydrate discoveries increased.

The formation and stability of gas hydrates are controlled by specific pressure- and temperature conditions. Natural gas hydrates are found mainly in arctic permafrost regions and in deep-sea marine areas that provide the required low temperature and high pressure stability limitations.

Why is it important to study natural gas hydrates? Natural gas hydrates have significant impacts on the human life. (1) They are a potential source of a cleaner fossil fuel when compared to burning coal or oil. (2) Gas hydrates play a significant role in global climate change, because methane acts as an important greenhouse gas. (3) Due to their stability conditions and occurrences in marine environments, they are a potential marine Geo-hazard.

(1) Since the mid 1960's discovery of natural gas hydrate accumulations in the former USSR (reviewed in *Makogon*, 1981), its potential as a natural resource came to the attention of researchers in many countries, particularly those with limited conventional hydrocarbon

resources. The attraction of gas hydrates as a potential energy resource developed, because gas hydrates contain highly concentrated amounts of natural gases, i.e. 1 m^3 of methane hydrate can contain the equivalent of 164 m^3 of methane at standard atmospheric temperature and pressure (STP, *Sloan*, 1998). However, detection, mapping, and exploration were difficult due to the lack of appropriate methodology and available techniques at that time. Despite significant effort in the last 40 years, still little is known about how to extract methane gas out of the natural hydrate state.

The first industrial-scale gas hydrate production test was completed in 2002 at the Mallik site in the Mackenzie Delta (reviewed in *Dallimore and Collett*, 2005). The test provided significant insight into the formation response and geotechnical changes during gas hydrate dissociation. A second test using reservoir depressurization was conducted in 2007/2008 at the same site (*Dallimore et al.*, 2008; *Kurihara et al.*, 2008). The test was successful in producing gas from the reservoir at considerable flow rates of up to 3000 m^3 per day and is seen as proof of concept for future industrial development. Economic extraction procedures in marine environments are still in the testing stage but significant efforts and progress have been made. The recently completed production test on the Alaska North Slope included a novel CO_2-Methane exchange experiment (*Schoderbek and Boswell*, 2011). A first short-term production test is planned for 2013 in the Nankai trough (e.g. *Kurihara et al.*, 2011).

(2) Methane is a very strong greenhouse gas that has a 72 times stronger global warming potential than carbon dioxide for a 20-year time period (*Forster and Ramaswamy*, 2007). Rapid dissociation of seafloor gas hydrate is one possible source of methane release into the atmosphere that could have a strong impact on the atmospheric composition (e.g. *Kennett et al.*, 2003; *Reagan and Moridis*, 2008; *Archer et al.*, 2009). However, studies by e.g. *McGinnis et al.* (2006) have shown that significant methane release into the atmosphere is only possible from shallow (<100 m) water depth. Most of the methane that reaches the

sea-surface is dissolved into the water column. Recent studies by *Archer* (2010) show that the impact of methane gas from oceanic gas hydrate sources is much less compared to methane gas released from onshore natural and artificial wetlands.

(3) Hydrate dissociation processes can increase the risk of seafloor failures (*Kastner and MacDonald*, 2006; *Grace et al.*, 2008; *Collett et al.*, 2009b). When hydrate dissociates, the resulting volume and density change in the sediment can contribute to local destabilization of the continental slope and result in submarine slides, collapses, and slump failures. These structural collapses can be accompanied by massive releases of natural gas that further accelerate the circuit of destabilization. Locally, gas hydrate dissociation due to pressure and temperature changes induced by heat transfer during petroleum production may lead to high rates of methane gas production, which may result in blowouts and collapses of sediments, as well as gas leakage (e.g. *Rutqvist and Moridis*, 2010).

Not only offshore-drilling sites are at risk when sediment failures and slumps occur close to the coast line. Submarine landslides caused by gas hydrate dissociation processes can affect the continental shelf region and therefore onshore populated areas as well. There is a potential risk of damaging tsunamis generated in the process of gas hydrate destabilization (e.g. *Micallef et al.*, 2008; *Brown et al.*, 2006).

Gas hydrate occurrences in different regions in Canada have been well surveyed and studied, especially at the convergent margin offshore Vancouver Island (e.g. *Hyndman and Davis*, 1992; *Riedel et al.*, 2006a) and in the arctic permafrost regions (e.g., in the Mackenzie Delta, *Dallimore et al.*, 1999, 2008). The eastern passive margin of Canada with its thick clastic sediment sections is another potential location for gas hydrate occurrences. Conventional natural hydrocarbons have already been discovered and produced at the eastern Canadian margin. However, the distribution and quantities of gas hydrates at the Canadian margin are still poorly understood. No gas hydrates have been recovered on the Canadian Atlantic margin, and there has been limited interpretation of gas hydrate occurrence based on geophysical downhole logs (e.g. *Neave*, 1990) that has not been confirmed or calibrated by analysis of recovered hydrate.

1.2 Thesis objectives

Gas hydrate increases the seismic velocity of sediments so that the concentrations can be determined from enhanced seismic velocities, if an adequate no-hydrate reference velocity can be obtained. Seismic studies directed at detection and mapping of gas hydrates off Canada's east coast have been carried out over the last 15 years. The first part of the thesis focuses on velocity analysis utilizing travel-time inverse modeling of two different ocean-bottom-seismometer (OBS) data sets combined with 2-D single-channel seismic (SCS) reflection data. This is the first study on utilizing both data sets in a combined travel-time inversion approach with data from the eastern Canadian margin. The results from the travel-time inverse modeling provide new constraints to estimate gas hydrate and free gas concentrations within the study area. Previous results from studies by *LeBlanc et al.* (2007); *Cullen et al.* (2008); *Mosher* (2011); *Delescluse et al.* (2011) are discussed and compared to the results of this thesis study.

In the second part of this thesis, the main objective is to investigate OBS survey acquisition geometries and seismic source requirements in order to detect velocity anomalies associated with gas hydrate and free gas occurrences for areas such as the passive Scotian margin. Some constrains are provided by a comparison of velocity models obtained with two different OBS data sets using different survey geometry parameters. Further constraints are provided by generating synthetic seismograms for a known model containing gas hydrate and free gas, and applying a waveform inversion modeling approach to the synthetic data.This research study is the first of its kind to apply frequency-domain waveform inversion techniques to OBS data to investigate marine natural gas hydrate occurrences at the eastern Canadian margin. The waveform inversion modeling with synthetic OBS data provides new information about resolution limits of OBS surveys, signal-to-noise (S/N) ratios of OBS data, and acquisition geometries for future OBS surveys.

In the last part of this thesis study the waveform modeling approach is applied to the real OBS data from the 2006 survey and the final velocity model obtained through travel-time inversion. Results of this study will show the significance of the source signal strength and acquisition geometry of real OBS surveys.

1.3 Regional geology of the Scotian margin

This section gives a general overview of the geological and sedimentation history of the Scotian margin from the Mesozoic rifting and opening phase of the Atlantic Ocean through the Cenozoic sedimentary basin evolution and sedimentary history to the current state. Understanding the geological and sedimentation history of the margin is ultimately linked to understanding gas hydrate distributions. Gas hydrate distribution is related to the sediment grain size as it is a well-known fact (e.g. *Ginsburg et al.*, 2000) that naturally-occurring gas hydrate has a tendency to accumulate in coarser-grained sediments (e.g., turbidite sands or silts).

In the absence of sand or silts (i.e., in a mud-dominated system with low permeability) gas hydrates have the tendency to form in a grain-displacing mode either as nodules or fine veins or fractures (e.g., as observed on Hydrate Ridge during ODP Leg 204, *Trehu et al.*, 2004). The detailed sedimentation history of the study area in this thesis can only be inferred through seismo-stratigraphic analysis.

1.3.1 Mesozoic evolution: Continental rifting and seafloor spreading

The Scotian margin was created during the opening of the Atlantic in the Early Jurassic (~175 Ma ago; Appendix 6.1) due to the diverging African-North American plate motions and represents rifting of Paleozoic platform rocks (e.g. *Royden and Keen*, 1980; *Funk et al.*, 2004). The initial rifting of the eastern Canadian margin started in the lower Mesozoic and continued with a slow spreading rate of 1cm/yr. Around 35 Ma the rifting stopped in the Labrador Sea (*Keen and Piper*, 1990), but continued along the remainder of the North American margin.

The Scotian margin is underlain by a number of connected platforms and depocenters referred to as the Scotian basin (e.g. *Grist et al.*, 1991). The Scotian basin extends over an area of 300,000 km^2 and half of the basin lies beneath the continental shelf in water depths of less than 200 m. The other half under the continental slope is in water depths of up to 4000 m (e.g. *Wade and MacLean*, 1990).

The oldest preserved syn-rift sediments are middle Triassic non-marine clastics (*Wade and MacLean*, 1990) that were followed by early Jurassic salt formations when the initial ocean was narrow and likely closed to circulation with the global oceans (~120 Ma ago). Those salt formations were ~2 km thick (locally exceeding 3 km) and where mobilized, salt rises as 10 km diapirs into the overlying strata (e.g. *Keen and Piper*, 1990; *Grist et al.*, 1991). These evaporites may play an important role in focusing upward migrating fluids and hydrocarbon gases into the hydrate stability field. The regional thermal regime, which is an important stability factor for gas hydrates, may be also affected by the high thermal conductivity of the salt (e.g. *Lewis and Hyndman*, 1976).

The evaporites are covered by thick sequences of marine sediments that were deposited in the late Jurassic and early Cretaceous accompanied by carbonates that filled the initial rift basins. The carbonate deposition was followed by the onset of seafloor spreading, representing the continental break-up of America and Africa. The subsidence that followed was caused by two processes; first from crustal extension while rifting and thinning, and later by thermal subsidence that started immediately after the initial break-up (e.g. *Royden and Keen*, 1980)

The subsidence was magnified by the effect of sediment loading with large amounts of Cenozoic clastic sediments. These fluvial-deltaic sands contain high concentrations of organic matter (e.g. *Wade and MacLean*, 1990). Further offshore marine carbonates and marine muds containing pelagic organic material were also deposited. These sediments are the source-rocks for most of the conventional hydrocarbons found in this area.

1.3.2 Cenozoic sedimentation history

The formation of substantial natural gas hydrates requires a combination of a number of factors, including a thick sedimentary section and adequate organic materials that break down to form natural gas, mainly methane. The breakdown is commonly through low-temperature methanogenesis, but also by high temperature thermal cracking. Upward fluid flow and lateral focusing of natural gases or fluids to form localized high concentrations of hydrate within the stability field are also required.

The late Cretaceous sediments that are over-pressurized due to rapid burial of the low permeable Tertiary shales may be the reservoir rocks for the substantial natural gas that probably contributes to the formation of gas hydrates in the subseafloor gas hydrate stability field.

Accumulation of hemipelagic sediments on the continental slope during the Tertiary off southeastern Canada was locally terminated by Miocene sealevel low-stands (*Piper and Normak*, 1989). These low sealevel stands are often seen as a prominent reflection in seismic data sets. One of these is the Mid-Miocene-Unconformity (MMU), which is probably due to an increase in sand content in the overall clay-rich formation (*Hansen et al.*, 2004).

With the beginning of the Late Pliocene, the sedimentation style changed in part to coarser grained sediments and accumulation rates increased due to the onset of terrestrial glaciation (*Piper and Normak*, 1989; *Mosher et al.*, 2004). Due to the increase in sediment burden, pressure in the deeper sequences increased, probably leading to fluid expulsion and upward migration into the shallower sediments using existing fracture systems.

The Scotian slope was mainly affected by glaciation during the middle Pleistocene and especially by the latest glaciation (Wisconsin). The maximum glacial extent was reached 18,000 years ago- often referred as the Last-Glacial-Maximum (LGM) - and the maximum extent of the ice-sheet was up to 600 m water depth, affecting the sedimentation of the upper slope (*Piper et al.*, 1990; *Gauley*, 2001). However, the deeper slope areas, including those of the study area, were not directly covered with ice during that time. Sedimentation rates were about half in times of non-glaciation periods compared to glaciation periods (*White*, 2005).

Submarine canyons are commonly observed on the central and eastern Scotian slope (*Mosher et al.*, 2004; *Keen and Piper*, 1990), whereas canyons are absent from the western Scotian slope (*Campbell*, 2011). These canyons (e.g., Logan Canyon, Dawson Canyon, Verril Canyon, and Mohican Channel) were mainly active during glaciation periods and they cut through the shelf and the slope during sealevel low-stand periods. Organic material mixed in the sediments were transported in those canyons into the deposition centers that were located on the foot of the continental slope. These deposition areas were buried with time and their organic matter later decomposed under bacterial activity to form natural hydrocarbon gases. The Mohican channel is located within the study area on the central-western Scotian slope and was an active major outwash channel during the LGM in the late Pleistocene (*White*, 2005).

As mentioned above, sedimentation increased during the Pleistocene resulting in a sequence estimated to be more than 500 m thick (*Piper and Normak*, 1989; *Mosher et al.*, 2005). The gas hydrate stability field extends into those sediments with the base of the gas hydrate stability zone (BGHSZ) calculated to be around 400 to 450 m below seafloor (bsf) in the study area (e.g. *LeBlanc et al.*, 2007; *Mosher*, 2011). The thickness of the Pliocene sedimentation does not vary much over the slope region, which indicates very uniform deposition. The sediments associated with the Holocene are a few tens of meters thick hemipelagic reworked glacial shelf deposits that were transported by wave and current activity (*Swift*, 1987).

1.3.3 Tectonic influences on the Scotian Slope

Post-rift sediments in the whole basin were cut by large syn-sedimentary faults (*Hansen et al.*, 2004). Most of these faults were active until the late Cretaceous. These faults are normal and planar and extend from approximately 500 mbsf down to 1200 mbsf (*Bennet*, 2000). Listric faults can be identified as well, but they are not as abundant and are mainly restricted to greater depths (~5 to 10 km) and some of these faults cease in the Jurassic formations (*Wade and MacLean*, 1990).

Studies by *Hansen et al.* (2004) at the Sable subbasin, show the development of small-scale polygonal faults in the Cenozoic formations. The density of the fault distribution decreases above the Miocene unconformity, which is possibly linked to an increase in sand content (*Hansen et al.*, 2004). The large-scale tectonic faults that were identified by *Bennet* (2000) have probably influenced the organization of those small-scaled polygonal faults in their near vicinity. The polygonal faults terminate against the larger tectonic faults.

Tectonic faults as well as some polygonal faults can either act as pathways or as traps for hydrocarbons. Here, different sediment lithologies are displaced and this change in physical properties (e.g., porosity) can effect the migration of fluids and gases. *Cullen et al.* (2008) defines the Miocene-Eocene unconformity at approximately 1200 m bsf as lower boundary for a distinct polygonal fault pattern. Geological structures (vents) that may act as conduits for fluids and gases are believed to originate in the same depth range and occasionally reach up to the sea floor (*Cullen et al.*, 2008).

1.4 Review of gas hydrate research

This chapter provides a brief review of the current state of worldwide research in gas hydrates including a more detailed summary of previous gas hydrate studies from eastern Canada. The historical evolution research in gas hydrates, the properties and generation of gas hydrates are emphasized for those aspects relevant to this study.

1.4.1 Natural gas hydrate

Gas hydrates are ice-like clathrate configurations of water and natural gas molecules. Those configurations form only under special conditions within the gashydrate-stability-zone (GHSZ) that include low temperatures and high pressures that generally only occur for water depths greater than 600 m (Fig. 1.1). At shallower depths, the temperatures are too high and the pressures are too low.

During the last 40 years numerous studies have been conducted worldwide to investigate the gas hydrate distribution (e.g., reviewed in *Makogon et al.*, 1972; *Kvenvolden*, 1988; *Collett et al.*, 2009b). Gas hydrates were sampled in gravity cores and cores from deep sea ocean drilling (ODP/IODP) operations, and inferred from scientific research studies, mainly active controlled-source seismic surveys (Fig. 1.2).

Numerous surveys and studies have shown that gas hydrates are common in the thick sediments of outer continental margins (e.g. *Spence et al.*, 1995; *Paull et al.*, 1996; *Riedel et al.*, 2006a). Natural gas hydrate samples have been recovered from the seafloor or from shallow marine sediment cores from many areas around the world, e.g., at northern Cascadia (*Hyndman et al.*, 2001; *Riedel et al.*, 2006a), in the Black Sea, the Caspian Sea, and the Sea of Okhotsk (*Ginsburg and Soloviev*, 1995), and in the East Sea (Ulleung Basin) (*Park*, 2008). Marine natural gas hydrate has also been recovered from greater sub-bottom depths by ODP/IODP deep-sea drilling, e.g., at the Blake Ridge (*Paull et al.*, 1996), Cascadia margin (*Riedel et al.*, 2006b; *Trehu et al.*, 2004), India (*Collett et al.*, 2006), and South

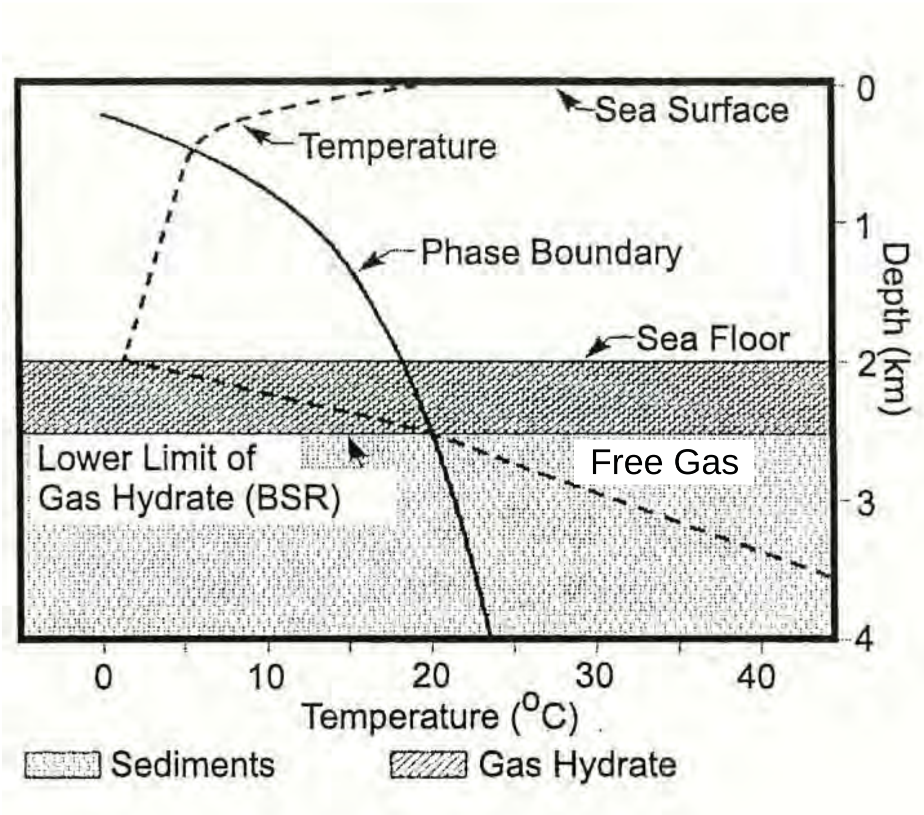

Fig. 1.1: Stability field for marine gas hydrates. Solid line indicates the phase boundary; dashed line refers to the temperature-depth profile. Increasing depth is equivalent to increasing pressure. The intersections of the temperature curve and the phase boundary mark the stability field boundaries (modified from *Dillon and Max* (2000))

Korea (*Park*, 2008; *Lee*, 2011).

Gas hydrates also have been discovered in permafrost regions of Alaska and northern Canada (e.g. *Collett*, 2004; *Dallimore and Collett*, 1998) as well as in northern Siberia (e.g. *Makogon et al.*, 1972; *Makogon*, 1981). The most detailed studies on permafrost gas hydrate samples are from sediment cores and downhole logs from gas hydrate research wells and associated seismic reflection surveys on the Mackenzie River delta (Canada) (*Dallimore and Collett*, 1998; *Dallimore et al.*, 1999). Industrial well-logs show the presence of numerous gas hydrate layers at a number of sites in the region, mainly through the high velocity and high electrical resistivity of gas hydrate. The Mallik gas hydrate production site has yielded the first detailed production test of gas hydrate accumulation with signif-

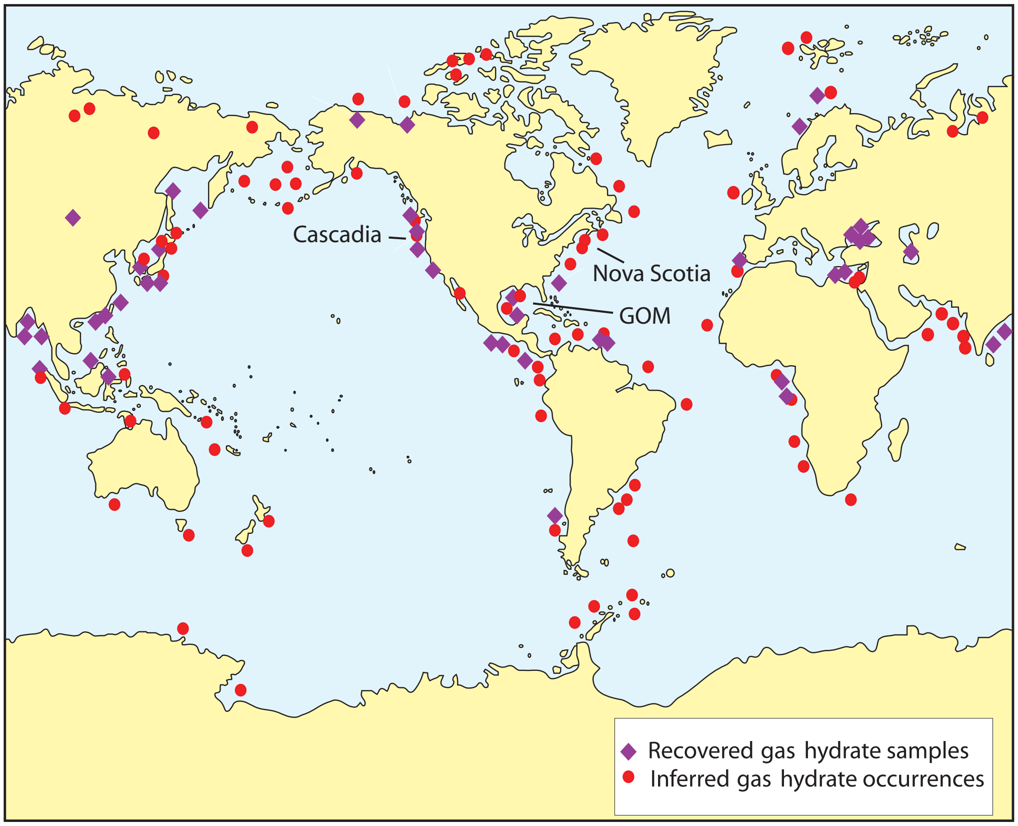

Fig. 1.2: Map of gas hydrate occurrences worldwide (recovered samples and inferred accumulations) (originally from *Kvenvolden* (1988) and recently modified in *Collett et al.* (2009b))

icant recoveries of gas (*Dallimore et al.*, 1999, 2008). Other prominent permafrost gas hydrate study locations are the Northern Slope of Alaska (e.g. *Collett*, 2004; *Boswell et al.*, 2008), where a production test was recently completed in the Prudhoe Bay (*Schoderbek and Boswell*, 2011).

1.4.2 Formation mechanism for natural gas hydrate

Several models have been suggested to explain the origin and formation of gas hydrates and free gas below the BGHSZ. However, only those relevant to the study area are reviewed in this section. Gas hydrates can form three distinct structural types that depend mainly on the size of the largest gas molecules (e.g. *Sloan*, 1998). Methane and ethane individually form structure I (sI) hydrate but can also form structure II (sII) hydrate in some combinations. Other hydrocarbons such as Propane and Butane form sII hydrate and heavier hydrocarbon molecules form structure-H (sH) hydrate (e.g. *Ripmeester*, 2000).

Structure I hydrate is mainly formed in marine environments from biogenic gases (e.g. *Collett et al.*, 2009b). This microbial-generated gas is the product of decomposition (oxidation) of organic matter by microorganisms and the reduction of carbon dioxide (methanogenesis) in low temperature environments. However, most sediments have a relatively low organic carbon content that leads to only a small production rate of biogenic gas within the GHSZ and therefore to a locally limited formation of gas hydrate (e.g. *Hyndman and Davis*, 1992; *Paull et al.*, 1994).

Some authors suggest that the formation of high concentrations of gas hydrate requires processes such as gas hydrate recycling (e.g. *Paull et al.*, 1994, 1996), that occurs at the BGHSZ. Changing sedimentation or tectonic uplift shifts the BGHSZ upward and the gas hydrate below the newly formed base of stability dissociates into natural gas and water. These gas-water mixtures rise upward above the newly formed stability base and re-form gas hydrates. Small gas residues may be left behind in the pore-space of the sediments below the newly formed base. Such recycling processes may especially apply to gas hydrates at convergent margins (accretionary wedges) with thin free gas zones below the BGHSZ (e.g. *Haacke et al.*, 2007).

The solubility-curvature mechanism described by *Haacke et al.* (2007) might explain the existence of a thick free gas zone (few hundred meters) with small gas concentrations beneath passive margins. Such occurrences also appear to have low concentrations of gas hydrate ($< 10\ \%$) within the GHSZ. *Haacke et al.* (2007) note that the upward driven methane rich pore-fluid flow is low ($\leq$ few tenth of mm per year) due to little or no tectonic activity. Therefore, the low upward flow and also low downward diffusion of methane from the existing GHSZ lead to a steady state of dissolved gas just below the BGHSZ (*Haacke* *et al.*, 2007). Because of the missing or limited tectonic uplift of the seabed gas hydrate recycling processes cannot likely account for significant gas hydrate formation at passive margins (*Haacke et al.*, 2007).

Hyndman and Davis (1992) proposed a model fluid-expulsion model that was intended to explain large gas hydrate concentrations in convergent margin areas, e.g northern Cascadia. In their model, the authors stated that the methane is removed from the upward migrating pore fluids that rise into the stability zone. The gas hydrate layer would build upward from the sharp BGHSZ to a gradational top (*Hyndman and Davis*, 1992). However, drilling and coring results from IODP Expedition 311 disproved this model for the Cascadia margin, as no regionally extensive layer of high gas hydrate saturation near the BGHSZ was found and a revised model for accretionary prisms was proposed (*Riedel et al.*, 2010). At most sites along the drilling transect of Expedition 311, gas hydrates were abundant throughout the GHSZ but closely linked to the occurrence of sand layers. The highest concentrations occurred also at much shallower depths (*Riedel et al.*, 2010) than expected from the model by *Hyndman and Davis* (1992).

The biogenic methane from in-situ organic carbon might not be sufficient enough to form the estimated quantities (*Hyndman and Davis*, 1992), but gas from deeper sources might be required to form the amounts needed for large gas hydrate deposits. Although *Malinverno* (2010) did predict that local in-situ production of methane by microbial activity explains the gas hydrate saturation levels seen during IODP Expedition 311, some advective portion of methane must contribute to the gas hydrate formation as otherwise, gas hydrate should also be present in the abyssal plain where in-situ organic carbon content is at equivalent levels to the sites cored within the accretionary prism.

Similar to the fluid-expulsion model described by *Hyndman and Davis* (1992), the gas-bubble model by *Haeckel et al.* (2004) refers to a process where rising gas bubbles from a deeper source form hydrate deposits close to the seafloor. The high demand of gas for large quantities of gas hydrate comes from the methane gas precipitation out of these gas bubbles (*Haeckel et al.*, 2004). Seafloor deposits of gas hydrate may originate from gas bubbles rising through vent conduits or small fissures in the sediment creating porous gas hydrate with bubble fabric (*Haeckel et al.*, 2004).

According to several studies such as *Malinverno* (2010), gas hydrates are not uniformly distributed in the sediments of the GHSZ. In these systems, sediment grain size is the main control on the heterogeneous distribution of gas hydrates (*Malinverno*, 2010). Those studies argue that gas hydrates are mostly found in coarse-grained sediments neighboring finer-grained sediments that contain little or no gas hydrate. Because of capillary effects and hydrophilic mineral surfaces, gas hydrate formation is inhibited in small sediment pores (e.g. *Claypool and Kaplan*, 1974). The small pore sizes may also limit the nucleation of gas hydrate (e.g., reviewed in *Malinverno*, 2010). Microbial methane is the primary source for in-situ formed gas hydrates within the GHSZ in coarse-grained sediments. *Malinverno* (2010) suggests that the fine-grained sediments host the methane that is accumulated and transported into the coarser-grained sediments where it forms the gas hydrate. *Malinverno* (2010) further argue that gas hydrate nodules and lenses are formed in fine grained sediments if no coarse-grained sediments are present.

The idea of gas venting was further developed by *Liu and Flemings* (2007). Free gas migrates through the GHSZ linking gas hydrate formation with salinity increase in the pore water. If the pore water becomes too saline the gas hydrate formation process stops. Their modeling also shows that gas hydrate formation depends largely on the grain size of the sediments. Gas hydrate forms at the BGHSZ in coarse-grained sediments. Large volumes of gas are rapidly transported into the stability zone, generate gas hydrate, and produce a significant change in salinity. However, in fine-grained sediments formation of gas hydrate results in rapid permeability reduction preventing free gas transportation into the GHSZ. The gas hydrate formation itself is concentrated at the BGHSZ.

The thermal gradient in those areas is higher than for passive margin environments, which accounts for the shift of the solubility curve toward the seabed. The steady-state curve of the dissolved gas coincides with the downward solubility curve just above BGHSZ (*Haacke et al.*, 2007). Therefore, only thin free-gas layers can exist in such environments.

1.4.3 Microbial versus thermogenic methane gas

Besides the biogenic gas production, thermo-chemical alteration of organic matter by thermal cracking of deeply buried organic carbon in greater depth form thermogenic gas. These gases from deeper sources might be required to form the sufficient amount of gas needed for large gas hydrate quantities (e.g. *Hyndman and Davis*, 1992).

Most of the past research has focused on the occurrence of biogenic gas as source for gas hydrate formation. However, recent studies in northern Alaska (*Collett et al.*, 2009b) and northern Canada (*Dallimore et al.*, 2008) have documented the importance of thermogenic gas sources to the formation of highly concentrated gas hydrate accumulations.

Biogenic and thermogenic gas can be distinguished through the geochemistry of the gases. The stable carbon-isotope signature of methane is used to determine if it was formed microbially or thermogenically. Pure biogenic formed methane contains isotopically lighter hydrocarbons and is more depleted in δ^{13}C with values in the range of -90 ‰ to -60 ‰ (*Pohlman et al.*, 2005). Thermogenic formed methane is more enriched in δ^{13}C and has values that range between -50 ‰ to -20 ‰ (*Pohlman et al.*, 2005).

1.4.4 Historical overview of gas hydrate findings and studies worldwide

The first interpretations of natural marine gas hydrate from geophysical measurements were made in the Blake Ridge area of the Atlantic ocean offshore the south-east coast of the United States of America (e.g., reviewed in *Sheridan*, 1980; *Kvenvolden*, 1988). The first identification of gas hydrate in drill-holes was made in the permafrost region of Siberia

(Russia) in the Messoyakha gas field, which has produced gas since 1969 (*Makogon et al.*, 1972; *Makogon*, 1981), although the gas hydrate origin of the gas is not certain.

Gas hydrate findings were mostly related to occurrences of bottom-simulating reflectors (BSRs) in the reflection seismic data. The BSR normally marks the BGHSZ and approximately follows the topography of the seafloor. The base of stability depends on the temperature and pressure regime of its environment and is often accompanied by a free gas layer underneath, especially in marine environments. The change in physical properties (such as velocity and density) from the gas phase to the gas hydrate phase results in an upward increase in impedance and hence a strong reflection coefficient. Gas hydrates increase the P-wave velocity in shallow unconsolidated near-seafloor sediments, where P-wave velocities normally have values of 1600 to 1800 m/s (e.g. *Helgerud et al.*, 2003). In contrast, the presence of free gas in even very low concentrations ($\leq 1\,\%$) can substantially reduce these seismic P-wave velocities (50 to 100 m/s) (*Lee*, 2004).

Over the last 40 years gas hydrates were found in numerous places worldwide (Fig. 1.2). As mentioned above, Blake Ridge was one of the earlier findings where intensive investigations and offshore drilling operations (e.g., ODP Leg164 *Holbrook et al.*, 1996; *Paull et al.*, 1996) were carried out in the mid 1990s. Even though a significant part of the Blake Ridge appears to be underlain by gas hydrates, core-samples and analyses of logging-data first showed that the concentration of hydrate appears to be low (mostly 5 - 7 $\%$) (*Paull et al.*, 1996). However, recent studies by *Hornbach et al.* (2008) show that gas hydrates occur also in higher concentrations up to 17 $\%$ sediment volume restricted to small geological structures such as lenses that are distributed over an area of approximately 20 to 30 km^2.

Other major marine drilling programs followed offshore western North America (Hydrate Ridge and North Cascadia margin), offshore India, offshore South Korea, and China, and at the Nankai Trough offshore Japan. The most recent drilling operations were conducted in the Gulf of Mexico (GOM) in a joint industry project that was formed in 2002.

The main objectives of the GOM project were to study environmental and technical hazards associated with drilling of gas-hydrate-bearing sediments, to develop and test geological and geophysical tools to predict and characterize gas hydrate, and to sample gas-hydrate-bearing sediments (*Collett et al.*, 2009a). Recent drilling results from spring 2009 show that gas hydrates are mainly found in sand layers and within fractures. *Collett et al.* (2009b) stated that hydrate-filled fractures are the most likely explanation for the localized occurrences of gas hydrates.

Studies of production performances for natural gas from marine gas hydrate reservoirs have been conducted in the Nankai Trough since the late 1990s and a first-short term production test is prepared for early 2013 (e.g. *Kurihara et al.*, 2011).

Results from the GOM and elsewhere have shown that highly saturated gas hydrate deposits do not need to be associated with BSRs in seismic data. Hence, a re-assessment of BSRs as the main indicator of gas hydrates has to follow in the near-future. Other strategies such as assessing the gas hydrate petroleum system (e.g., reviewed in *Collett et al.*, 2009b), where several individual factors (pressure-temperature stability, gas source, gas migrations, etc.) are linked, have to be considered.

1.4.5 Review of gas hydrate research at Canada's east coast

As mentioned earlier, Blake Ridge is one of the well known examples for the passive margin gas hydrate bearing reservoirs. Its geological structure is comparable to that of Canada's east coast where lateral inhomogeneous sedimentation of fine grained sands and other pelagic deposits are dominant.

The passive margin off eastern Canada was widely mapped during the last 40 years by the hydrocarbon exploration industry. From industrial data, the concentrations of natural gas hydrates were estimated from 26 offshore wells drilled in the late 1980s (*Neave*, 1990; *Shimeld et al.*, 2004).

The theoretical GHSZ of the Scotian margin was estimated by *Majorowicz and Osadetz* (2001) and is calculated with an area coverage of 400,000 km^2 ranging in water depths of between 300 and 2000 m. Heat-flow measurements provided an average temperature gradient of 30 mK/m in the upper 100 m below the the seafloor of the continental slope and the estimated volume of methane gas in subseafloor gas hydrate reservoirs was approximated with $1.9 - 8.7 \cdot 10^{13}$ m^3 at STP conditions (*Majorowicz and Osadetz*, 2001). More recent studies by *LeBlanc et al.* (2007), *Cullen et al.* (2008), and *Mosher* (2011) for areas associated with mapped BSRs in reflection seismic data estimated a total volume of $2.8 - 8.4$ $\cdot 10^{12}$ m^3 methane gas in subseafloor gas hydrates assuming the average gas hydrate layer thickness of 79 m.

An extensive database of seismic reflection data exists for the east coast of Canada. *Mosher* (2011) identified seven regions along the eastern Canadian margin where BSRs were mapped in the 2-D seismic reflection data (Mohican Channel, Haddock Channel, Barrington, Sackville Spur, Orphan Spur, Hamilton Spur, and the Makkovik Bank). In 1998/9 the Geological Survey of Canada (GSC) collected a total of 34,000 km of 2-D multichannel seismic (MCS) profiles on the Scotian Slope.

Gas hydrate distributions were estimated based on the area where a BSR was confidently identified (*Mosher*, 2011). However, estimates of gas hydrate concentration are poorly constrained - no gas hydrate has been recovered on the Canadian Atlantic margin, and limited interpretation of hydrate occurrence based on geophysical downhole logs (Thurber Consultants Ltd., *Neave*, 1990) has not been confirmed or calibrated by analysis of recovered hydrate.

The Mohican channel BSR, the focus of this study (Fig. 1.3), covers an area of 345 km^2 ranging from 300 to 450 m below seafloor (bsf) (*LeBlanc et al.*, 2007; *Cullen et al.*, 2008; *Mosher*, 2011). Studies by *Mosher et al.* (2005) and *Cullen et al.* (2008) show a second BSR occurrence underlying the first BSR in some areas (Fig. 1.4). The double BSR occurrence may have been caused by sediment movement along the Mohican Channel zone that caused changes in the position of the GHSZ (*Cullen et al.*, 2008). Dissociation of gas hydrate from a deeper (lower) GHSZ to a new location would result in a new BSR location. *Cullen et al.* (2008) mentioned that changes in sea-level and bottom-water temperatures due to glaciation are possibly related to changes in the stability field.

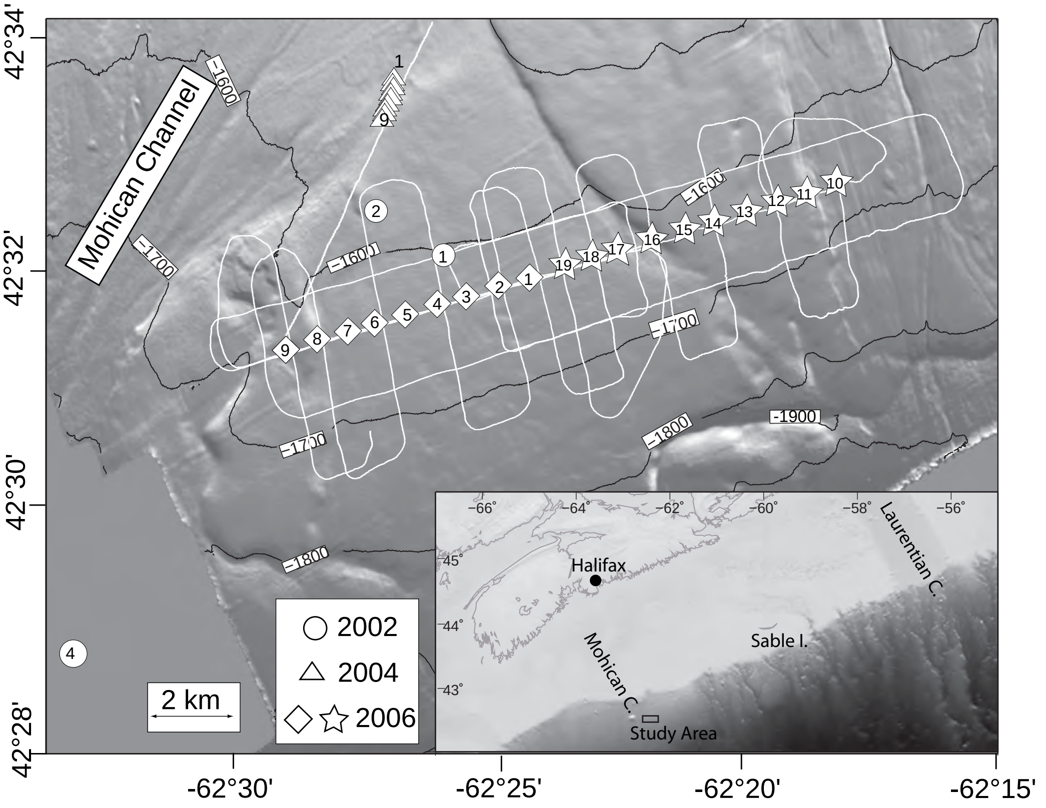

Fig. 1.3: Map showing the study areas and OBS instrument deployment locations of *LeBlanc et al.* (2007) (circles), *Cullen et al.* (2008) (triangles) and from the 2006 study (diamonds, stars). White lines are the shot profiles conducted for the 2004 and 2006 OBS and SCS data. The inset shows the location of study areas (box) in relation to the Scotian margin.

The Mohican channel BSR is intersected with a system of small-scale faults, sometimes referred to as polygonal faults (*Shimeld et al.*, 2004). These faults sole into a layer with a higher amplitude than the surrounding reflectivity, likely a gas-charged horizon (*Mosher*, 2011).

Interpretation of reflection seismic profiles by *Shimeld et al.* (2004) and velocity modeling on OBS data by *LeBlanc et al.* (2007) indicated low-velocity anomalies occurring near the BGHSZ where free gas may be present. This could be an indicator of gas hydrates without the strong BSR reflection visible in the seismic profiles (*Shimeld et al.*, 2004; *LeBlanc et al.*, 2007). Attempts to explain gas hydrate occurrences without BSR appearance are strongly related to the sediment structure. *Mosher* (2008) concludes that the sparse BSR appearance might be caused by either rare gas hydrate accumulations or due to the limit of geophysical exploration methods used so far.

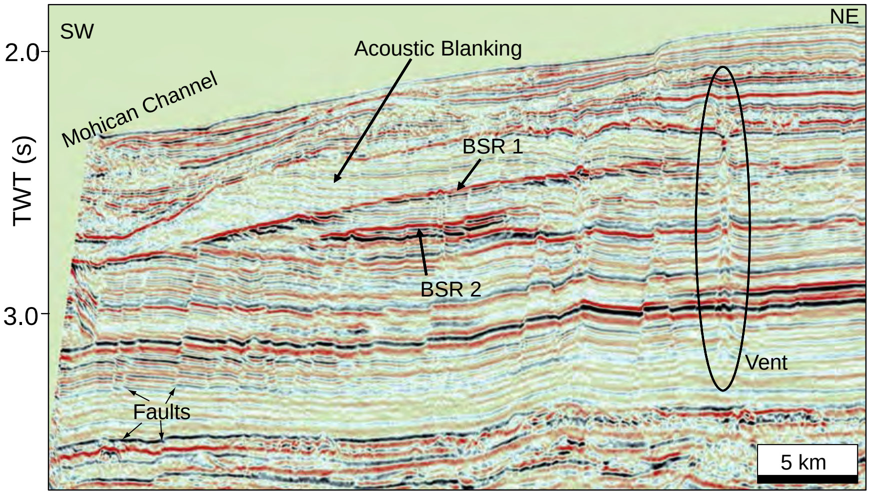

Fig. 1.4: Double BSR (BSR 1 and BSR 2) observed in 2-D seismic reflection data near the Mohican Channel (*Cullen et al.*, 2008). Near-vertical faults (arrows) that sole in-to a high amplitude layer at the bottom of this figure and other geological structures were identified (modified from *Cullen et al.*, 2008).

Studies were carried out in 2002 by *LeBlanc et al.* (2007) in the Mohican channel area with the deployment of three individual OBS stations (see figure 1.3 for deployment location). The resulting 1-D velocity profiles (Fig. 1.5) obtained through travel-time inversion show a low-velocity-zone (LVZ) near the depth range, where the BSR was identified in corresponding 2-D MCS reflection data sets. The LVZ, with a velocity decrease of 50 to 70 m/s and a maximum thickness of 260 m, is found beneath a 120 m thick high-velocity-zone (HVZ) (Fig. 1.5). *LeBlanc et al.* (2007) concluded that the absence of the BSR in some areas of the Scotian Shelf and Slope region is due to a gradual boundary between the BGHSZ and the underlying free gas, or alternatively that gas is absent. *Mosher* (2011) stated that most of the recognized BSRs are within large sedimentary drift deposits that were transported during the Miocene and Pliocene (*Campbell et al.*, 2010). Recent studies show that the Pleistocene-to-recent Mohican Channel cuts through these deposits, exhibiting various episodes of cut-and-fill during this period (*Campbell et al.*, 2010; *Mosher*, 2011).

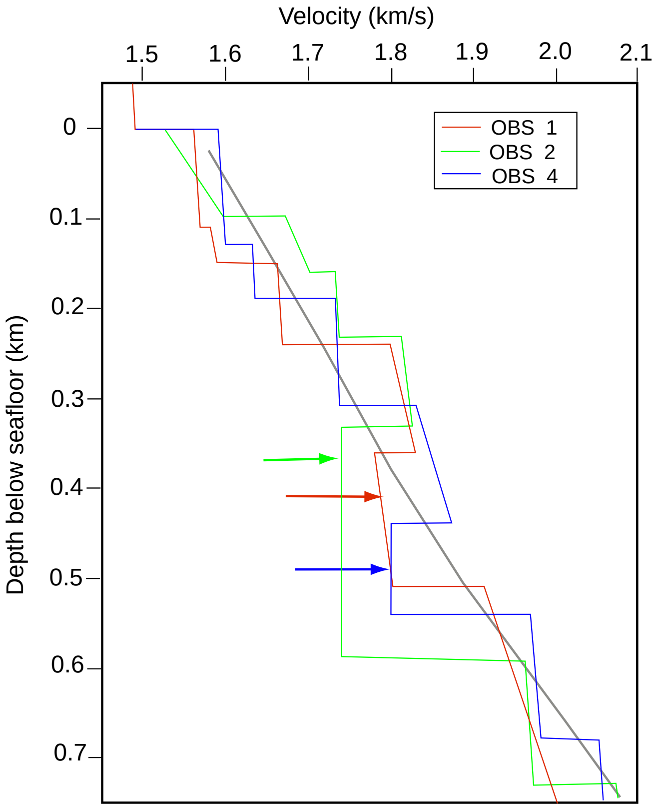

Fig. 1.5: Velocity model from 3 OBS stations modified from *LeBlanc et al.* (2007) with the regional trend calculated from a rock-physics model (grey line). Colored arrows indicate the low-velocity zones for the different OBS locations.

Travel-time inversion results on OBS data along a 2-D profile in 2004 in the vicinity of the Mohican Channel were presented by *Cullen et al.* (2008) in the form of 1-D vertical velocity profiles.

The amplitude and the distribution of the BSR were mapped in 3-D MCS reflection data acquired by Encana Ltd. in 2000 (*Cullen et al.*, 2008). The BSR is a strong reflection in the vicinity of the Mohican Channel, but fades into a weaker reflection towards the east of the Scotian slope and shelf. Within the region of the 3-D mapping by *Cullen et al.* (2008), there are zones of acoustic blanking (Fig. 1.4) below the BSR related to free gas accumulation. The modeled low-velocity zones in the 1-D profiles by *Cullen et al.* (2008) strengthen the hypothesis of free gas below the BSR. Vertical vent structures were also mapped on the 3-D MCS reflection data set (Fig. 1.6 a) as well as randomly distributed fluid-escape features that were identified at the surface of the BSR layer (Fig. 1.6 b). However, such structures were not observed close to or directly at the seafloor, which is probably related to a reduction in fluid-flow rates over time (*Cullen et al.*, 2008). The polygonal fault-system that was first discovered by *Shimeld et al.* (2004) was constrained in this study and limited to two-way-travel-times (TWT) of 0.5 to 1.5 s below seafloor (Fig. 1.6 a). *Cullen et al.* (2008) conclude that the fault pattern results from fluid release of overpressurized Cenozoic mud-rocks, commonly found in claystones with very low permeability.

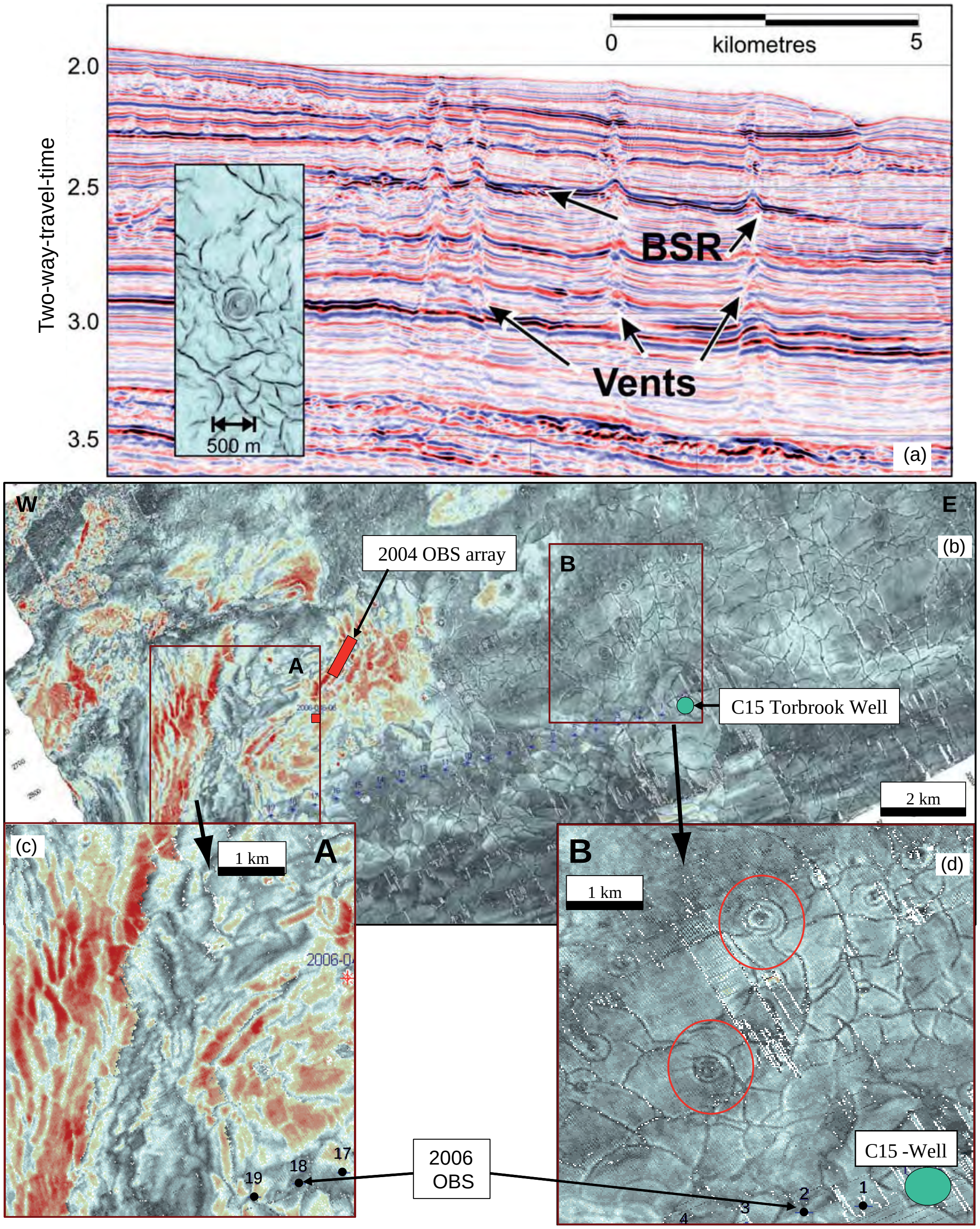

Fig. 1.6: (a) Seismic line interpreted by *Mosher et al.* (2005) shows the vent structures and polygonal faults in a time-slice (box). (b) Amplitude map of BSR depth taken from the 3-D MCS reflection data (Encana Ltd.). (b,c) The high amplitude regions (red) show that the BSR is concentrated in the western part of the study region. (d) The polygonal fault pattern as well as fluid-escape features (red circles) are restricted to the BSR surface (modified from *Cullen et al.* (2008).) The 2006 OBS arrays are used in the velocity analyses of this thesis study.

1.5 Review of geophysical methods to study gas hydrate systems

Shallow marine sediments containing neither gas nor gas hydrate generally have P-wave velocities around 1600 to 1800 m/s. The S-wave velocities of these sediments are ~300-800 m/s and their densities are ~1800 kg/m^3 (e.g. *Hamilton*, 1980; *Spence et al.*, 2010). Pure methane gas hydrate has a P-wave velocity of 3650 m/s and a S-wave velocity of 1890 m/s (e.g. *Waite et al.*, 2000). Hence, large concentrations of gas hydrate within the sediment pore space increase seismic velocities dramatically. Nevertheless, the effect of small amounts of gas hydrate on seismic velocity in marine sediments, especially for S-waves, depends strongly on the distribution of the hydrate in the pore space (e.g. *Helgerud et al.*, 2003; *Chand et al.*, 2004). For example, if hydrate fills the pore space with little grain contact then it has almost no effect on S-wave velocity, since the shear modulus is unaffected and the density of hydrate is almost like that of pore water. However, the P-wave velocity increases due to the loss of pore volume (e.g *Chand et al.*, 2004). On the other hand, if the hydrate forms cement around the grain particles, then the structure becomes more rigid and produce a higher S-wave velocity. However, this has not been observed in nature yet.

Sediments containing even a small amount of free gas ($< 1\,\%$) in the pore space show a significant decrease ($> 5\,\%$) in P-wave velocity (*Lee*, 2004). However, only a small effect on S-wave velocities can be detected, unless the gas concentrations are sufficiently large that the sediment structure is affected (e.g. *Domenico*, 1976).

Since gas hydrate and free gas change the physical properties such as velocities and densities of shallow marine sediments, seismic methods are the most common used to detect gas hydrate and free gas. In the next sections those marine seismic acquisition systems, being utilized in this thesis study, are reviewed.

1.5.1 Review of seismic systems to conduct gas hydrate research

Single- and multi-channel seismic data acquisition

Single-channel seismic (SCS) streamers usually have a short length and a small number of bundled hydrophones. The data of those hydrophones are summed or stacked together to represent a single channel with improved signal-to-noise ratios and some directivity to enhance near-vertical incidence reflected waves. However, subsurface velocities cannot be obtained from SCS data, because of the lack of velocity move-out information. Hence, multi-channel seismic (MCS) streamers, where numerous hydrophone groups are recorded separately, give the opportunity to record long offsets and velocity-dependent move-out as well as to obtain amplitude variations with the varying offset (AVO). Those AVO analyses can provide information about the sediments and their pore-space content. As already mentioned, free gas or fluids contained in the pore space have a strong effect on the compressibility and P-wave velocity of a medium and the amplitudes of the seismic signal (e.g. *Ostrander*, 1984).

Although streamer systems are commonly used for seismic data acquisition, the relocation of the hydrophone groups accurately within the water column is still difficult. The streamer moves with water movements as waves, tides, and currents and a horizontal position is not always confined. Wide-angle reflections are often only recorded on long offset streamers (several kilometers long), that are difficult and expensive to handle and bear the risk of loosing or damaging parts of the system during the survey.

Seismic source signals are typically transmitted with airgun systems that are towed behind the ship within the same depth range as the receivers. The seismic pulse is generated through released air. Besides the primary pulse, that is recorded at the receivers, the so-called bubble-pulse is caused by the oscillating air-bubble, and its appearance in the seismic data interferes with the primary seismic reflection. Hence, other airgun-systems are used to suppress the bubble during the acquisition. Generator-Injector (GI)-guns for example comprise two chambers, where the first chamber (generator) produces the primary pulse and the second chamber (injector) is triggered after a delay to suppress the bubble of the first pulse.

Airgun sources are considered to operate in a high frequency mode typically between 20 and 180 Hz. Thus longer wavelengths that provide information from deeper subsurface layers are limited. High frequency surveys provide a higher resolution of the shallow subsurface, and such surveys are often useful to study seafloor expressions of gas hydrate and free gas expulsion processes (e.g., pockmarks, vents) (e.g. *Hovland and Judd*, 1988). Combining larger guns in an array increases the volume of released compressed air, lowers the frequency range, and allows deeper penetration of energy into the subsurface.

Ocean-bottom seismic instrumentation

Besides using shallow and deep-towed streamer acquisition systems, ocean-bottom instruments (OBS/OBH) are commonly used for gas hydrate research studies (e.g. *Korenaga et al.*, 1997; *LeBlanc et al.*, 2007; *Petersen et al.*, 2007; *Cullen et al.*, 2008; *Lopez et al.*, 2010; *Dash and Spence*, 2011). Those systems usually consist of one hydrophone (OBH) and a three-component seismometer (OBS) deployed at the seafloor. The direct arrival from the source to the receiver is recorded with the hydrophone and provides information about the water depth of the instrument given the water velocity is known. The seismometer records seismic energy in two horizontal and one vertical direction. The combination of the three components provides information about the anisotropic wave propagation, such as the orientation of faults that could act as transport ways for fluids and gases as well as fault controlled gas hydrate. Depending on the survey geometry, wide-angle reflections and refractions from deeper subsurface layers can be detected with all four components.

Investigation of gas hydrate with OBS/OBH systems is dependent on the thickness of the gas hydrate and free gas layer as well as the survey geometry. Within the OBS/OBH system geometry the reflection point moves with shot offset. Hence, velocity analysis is difficult, if velocities vary rapidly laterally. This limitation can be reduced with closely spaced OBS stations (less than 100 m separation). Therefore, spacing between the OBS/OBH stations can be crucial for the velocity analysis and identification of gas hydrate layers as will be later discussed in the thesis.

1.5.2 Methods to analyse OBS seismic data for gas hydrate research

This thesis focuses on seismic velocity analysis with OBS and SCS data. The next section gives a short overview over two methods that deal with velocity analyses for OBS data. However, those methods are described more detailed in the later part of this thesis (chapters 3 and 4) and are only mentioned at this stage.

Seismic travel-time tomography

Displaying OBS data can be seen as a conventional shot-gather (one shot recorded on multiple hydrophones). Therefore, velocity analysis could be applied in the same way using normal-move-out (NMO) corrections for wide offsets. However, the instrument has only one hydrophone and therefore a common-depth-point (CDP) gather is assumed where the reflection point is at one depth location. This correction gives only a vertical 1-D estimate of the velocity field.

Hence, seismic tomographic travel-time inversion methods are commonly used in 2-D and 3-D ray tracing approaches for OBS velocity analysis. Within this thesis, tomographic inversion of multi-component OBS data sets are used to study the velocity distribution of the shallow subsurface. Simultaneously, 2-D SCS reflection data are used to constrain depths from the vertical incidence ray-paths. Inversion of data from single OBS stations or stations that are wide apart results in only reasonable 1-D velocity profiles at the receiver locations. Single station OBS results do not provide information about velocity and density distributions around the station. Refractions and wide-angle reflections from OBS data provide significant velocity information, but only if the shot-receiver offsets are large enough.

There are two approaches of travel-time inversion methods that are used in a large range of studies both developed by Colin Zelt, RayInvr (*Zelt and Smith*, 1992) and FAST (*Zelt and Barton*, 1998). Travel-time inversion using RayInvr is based on modeling interfaces associated with velocities for the layers between those interfaces. This technique, further described in chapter 3, requires travel-time picking of events in time that must be identified with these interfaces and hence requires a strong a priori knowledge of the velocity structure. The other commonly used travel-time tomography approach, FAST, relies on the use of the first-arrival travel-times alone. The calculated travel-times are computed using a finite-difference solver for the eikonal equation (Appendix 6.3.1; *Nolet*, 1987; *Vidale*, 1990). However, large shot-receiver offsets are necessary to assure the proper illumination of the deeper part of the model. Also, the exploitation of only the first-arrivals is not very efficient in the determination of low-velocity zones, which tend to be avoided by first-arrival rays (e.g. *Sirgue*, 2003).

Seismic waveform inversion

Seismic waveform inversion is an important technique used for 2-D and 3-D velocity analysis and to obtain velocity information about the sub-surface. The seismic waveform contains much more information about the medium of propagation than is typically used in travel-time inversion. The full information content of the seismic waveform can potentially be accessed by waveform inversion methods (e.g. *Tarantola*, 1984). Over the past 20 years methods were developed in either time (TD) or frequency domains (FD) (e.g. *Minshull et al.*, 1994; *Pratt*, 1999). In waveform inversion, the "best" model is recovered by iteratively minimizing the misfit between the observed waveform data, and the synthetic waveform data from forward modeling (e.g. *Pratt*, 1999).

Solving the inverse problem is critically dependent upon the accuracy of the starting model and the minimum inversion frequency, since the highly non-linear problem can cause the solution to converge to a local rather than a global minimum. For all waveform inversion techniques it is crucial to know the seismic source signature to identify the modeled seismic arrivals from multiple or false (created) reflected arrivals. Frequency is an important factor, since the higher frequencies are lost first and therefore using the longest wavelengths provides more information about the deep subsurface. As noted for travel-time inversion approaches using multiple ocean-bottom instruments, the separation of instruments can be important for waveform inversion techniques as well.

Those methods have been applied to synthetic and real wide-angle OBS data sets (e.g. *Brenders and Pratt*, 2007a; *Korenaga et al.*, 1997; *Kamei et al.*, 2012). Studies were also carried out on 2-D MCS reflection data (e.g. *Hicks and Pratt*, 2001; *Yuan et al.*, 1999; *Delescluse et al.*, 2011; *Jaiswal et al.*, 2012).

Several other inversion methods are commonly used that incorporate the seismic waveform to model the velocity structure such as a 1-D impedance inversion (*Grevemeyer et al.*, 2000). Within this inversion approach the impedance (as the product of velocity and density) is modeled versus the travel-time based on the seismic reflectivity. The 1-D impedance inversion was applied on several 2-D MCS reflection data, e.g. from the Makran wedge (*Grevemeyer et al.*, 2000) and from the Ulleung basin (*Ryu et al.*, 2009).

2. SEISMIC DATA

The seismic data acquisition and preparation for the modeling are described in this chapter. Both, the 2004 and 2006 seismic data were processed for travel-time inverse modeling and the waveform modeling. In this chapter the processing and preparation of the 2006 data, the primary data of this thesis, are described first, and then the 2004 data.

2.1 Data acquisition during the seismic surveys of 2004 and 2006

As already mentioned in section 1.4, three OBS instruments were deployed in 2002 (*LeBlanc et al.*, 2007) at different locations in the Mohican channel area (Fig. 1.3 - circles) to estimate gas hydrate and free gas concentrations from velocity analyses. Additional information from 2-D SCS and MCS reflection data showed an irregular distribution of BSRs along the Scotian shelf and slope region (*Shimeld et al.*, 2004).

In July 2004 another two OBS arrays, with an instrument spacing of 100 m, were deployed in vicinity of the Mohican Channel area (Fig. 1.3 - triangles) and further eastward on the slope. The data were used in a series of 1-D velocity analyses and travel-time inverse modeling. Both data sets were analyzed in the PhD thesis work of J. Cullen (Dalhousie University) to identify seismic velocity zones related to free gas and gas hydrate in the sediment pore-space. In agreement with Dalhousie University and J. Cullen, the Mohican channel OBS and 2-D SCS reflection data, which were also acquired in the same survey from 2004, were used in a 2-D velocity modeling with travel-time inversion as part of this thesis study.

In August 2006 another 19 OBS deployments were carried out on the Scotian Slope close to the Mohican Channel (Fig. 1.3). The same OBS instruments and seismic airguns operated during the survey of 2004 were used in the 2006 survey. The main objectives of the 2006 survey were to detect lateral changes in the sub-seafloor velocities related to possible gas hydrate and free gas occurrences. The second objective, related to the first, was to determined why the BSR appears so localized in this passive margin environment. Therefore, the OBSs were deployed with a separation of approximately 900 m in two separate arrays. These two arrays extended in a 20 km profile from an area where the BSR is visible in the reflection seismic data sets (Fig. 1.3: OBS array 2 - diamonds) to the adjacent area where no BSR is apparent (Fig. 1.3: OBS array 1 - stars). This profile addresses the important question of whether or not the gas hydrate occurrence and concentrations are related to the BSR strength. The OBS array 2 is closer to the previous OBS arrays of the 2004 and 2002 surveys. Hence, modeling was started with OBS array 2 data. However, the OBS array 1 was not further used in this thesis study because of the poor data quality and because of the OBS array 2 analysis results that showed that the key arrivals (refractions from below the LVZ) were not significantly above the background noise level.

In addition to the OBS data 2-D SCS reflection data were also acquired in the 2006 survey. Among the 50 profiles, one seismic line was acquired along the OBS array 2. Hence, the coincident 2-D SCS data and OBS data were used in a combined travel-time inverse modeling. One high-quality 2-D reflection profile selected from a 3-D MCS reflection seismic data cube (courtesy of EnCana Ltd©) was also available for seismic interpretation and identification of key reflected arrivals that could be correlated among the data sets.

2.2 Data processing of the 2006 OBS array 2 data

Each OBS hydrophone component has a record length of 8 s with a sampling rate of 1 ms. The shot-interval was 6 s, which corresponds to a shot distance of 15 m given a ship speed of 5 knots. Each OBS channel recorded a total of 8 s to include wide-angle and refracted arrivals obtained at large shot-receiver offsets (personal communication with Keith Louden).

The data of OBS array 2 (Fig. 1.3 - diamonds) were collected to a maximum shot-receiver-offset of approximately 9.5 km with an average OBS instrument spacing between the adjacent OBS stations of 900 m. The direct wave transmitted from the source to the receiver is the first seismic arrival recorded with the instrument and its travel-time arrival at vertical incidence is used to determine the water-depth of the instrument. The bathymetric depths from multibeam data acquired by D. Mosher (GSC) and the water-velocity (sound-speed profile, Fig. 2.1) obtained from CTD (conductivity-temperature-depth) measurements were used to recalculate the direct wave arrival-times. However, an offset of 50 ms between the measured and the calculated first-arrival travel-times was observed. Hence, a time-shift correction was applied to the data before further processing was conducted. These delays are possibly related to data conversion errors from the OBS recording format on-board to the standard SEGY format (pers. comm. with M. Delescluse and K. Louden).

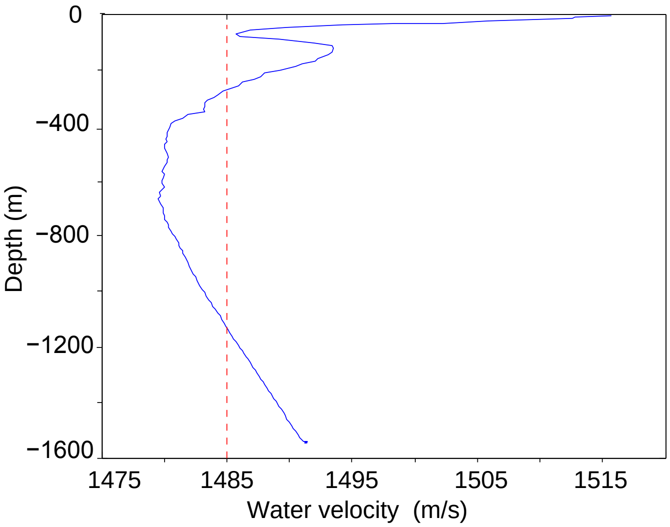

Fig. 2.1: Measured soundspeed in water column with CTD and calculated mean value (red dashed line) of 1485 m/s

In general the seismic data of all four components of the OBS array 2 instruments have a good signal-to-noise ratio (S/N=11 for the near-surface reflections). However, despite using a GI-gun to suppress the bubble pulse signal, it was still visible on some OBSs (Fig. 2.3). The amplitude spectrum recorded on the hydrophone component of OBS 1 (Fig. 2.2) shows a high amplitude peak at 8 Hz, which may be related to noise in the water column. Since this noise was also recorded on the 2-D SCS reflection data acquired at the same time as the OBSs recorded, it is most likely not an internal instrument noise. Bandpass filtering (10 to 250 Hz) of the data to remove the background noise was applied to each hydrophone component. Some components still show the low frequency bubble pulse that does not complicate the travel-time arrival identification and picking procedure.

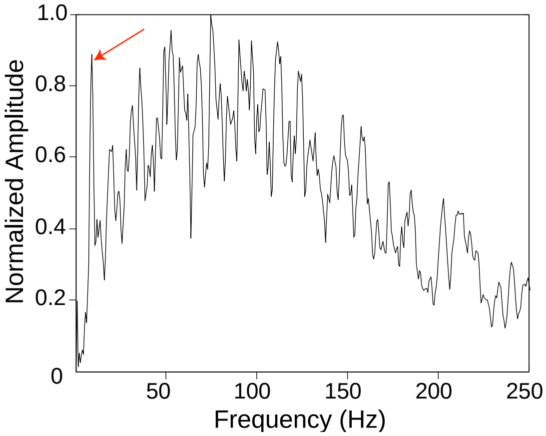

Fig. 2.2: Normalized amplitude spectrum of unfiltered OBS 1 data. Low frequency noise is visible at 8 Hz (red arrow).

The vertical geophone component and the hydrophone component were compared for identical reflections. Since the hydrophone is located within the water column and records pressure data only, the data show mainly P-wave reflections and refractions (Fig. 2.4 left). However, the three geophone components show the seafloor reflection and possible P-to-S wave converted arrivals, because the seismometer is placed directly on and coupled to the seafloor.

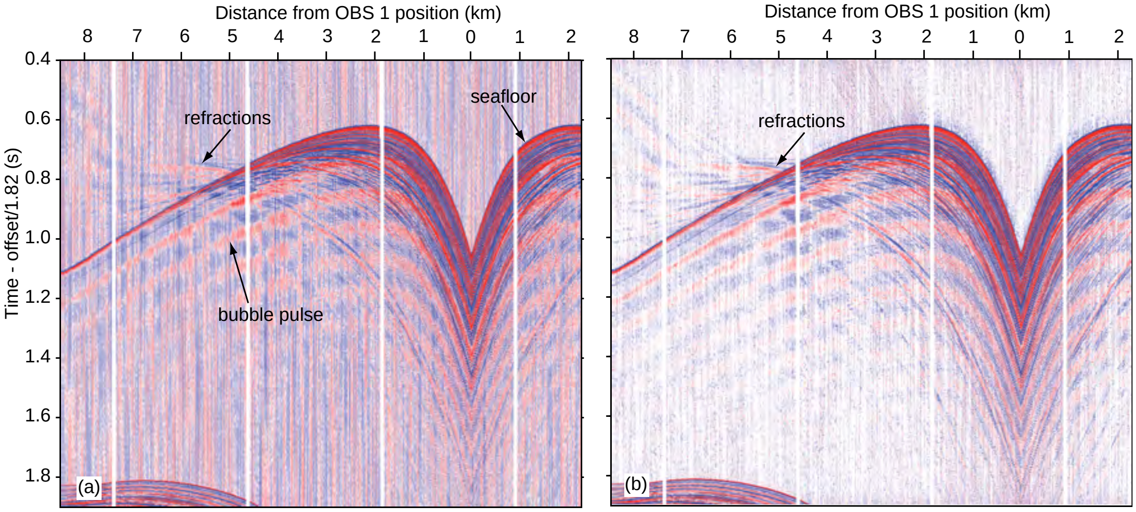

Fig. 2.3: (a) Unfiltered and (b) filtered (BP: 10-250 Hz) data from OBS 1 hydrophone component showing improvement in data quality for interpretation and identification of reflected and refracted arrivals. Seismic travel-times are plotted with a reducing velocity of 1.82 km/s to enhance the refractions. The bubble pulse is still visible in the (b) filtered data, but did not interfere with the identification and picking of the arrival-times.

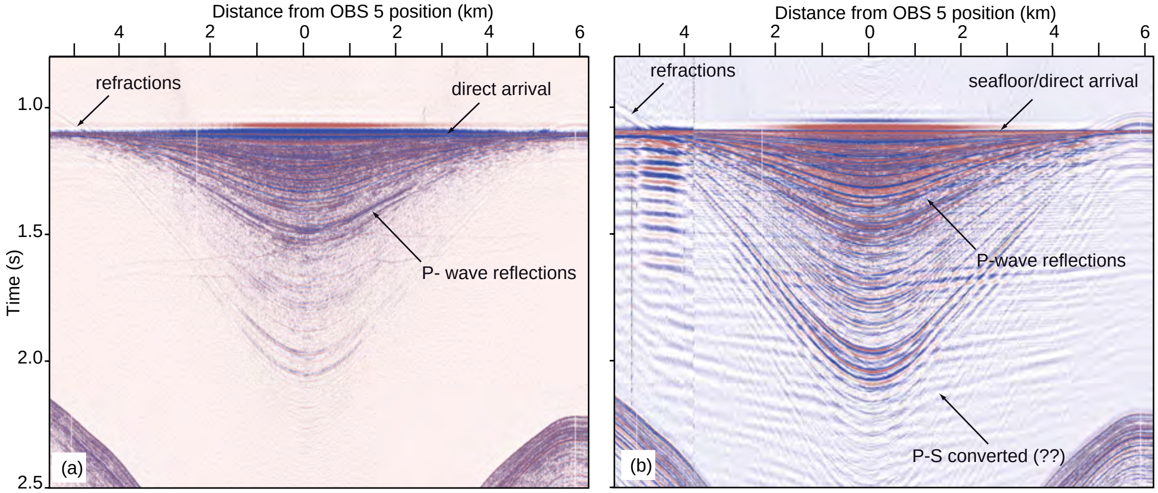

Fig. 2.4: Comparison of two channels of OBS 5: (a) Hydrophone component (BP:10-250 Hz) with an applied hyperbolic move-out (1.48 km/s) with identified P-wave reflections and refractions. (b) Vertical geophone component (BP:10-250 Hz) with an applied hyperbolic move-out (1.48 km/s). P-wave reflections and refractions as well as possible PS-converted reflections can be identified.

A hyperbolic move-out function was applied to both the hydrophone and vertical geophone data to "flatten" arrival times to facilitate horizon picking. The data were reduced to the direct arrival travel-time using standard Seismic UNIX (SU) [1] velocity move-out routines and an average reduction velocity of 1.48 km/s for the water column.

2.2.1 Relocation of the 2006 OBS and shot positions

The OBS instrument positions when dropped from the ship are accurately known to a few 10's of meters through GPS measurements. However, there may be a horizontal drift due to water currents, tidal and wave motions such that the position at the seafloor is significantly offset from the drop-site. Depending on the water current velocity, instrument drifts of up to several hundred meters have been estimated. Also the shot positions recorded can be inaccurate by up to tens of meters. Additionally, the OBS instruments often show drifts in their internal clocks, and these may vary from simple linear drift rates that are normally assumed for the period between deployment and recovery. Therefore, relocation of the OBS positions and applying clock-drift corrections, using inversion methods based on direct travel-time arrivals, are important processing steps.

The position and clock-drift inversion code used for this study was developed by *Zykov* (2006); it simultaneously inverts for the instrument positions and depths for all stations. A first linear clock-drift calibration is done on-board after retrieving the instruments. However, some clock drift still persists. The inversion method is based on a regularization that incorporates *a priori* information and uncertainty estimates of both the model parameters and the data into the solution. *A priori* information can include, e.g., the expectation of a smooth shot-profile or estimated values for model parameters (*Zykov*, 2006). The objective of the routine is to fit the observed direct travel-times to the model travel-times using the water velocity from the soundspeed profile. The setup of the 2006 geometry adds the

---

[1] supported by: Center of Wave Phenomena (CWP) at the Colorado School of Mines (CSM)

Model parameters	Initial uncertainties	Final uncertainties
Shot (x,y)	± 30 m	± 10 m
OBS (x,y)	± 50 m	± 50 m
OBS (z)	± 50 m	± 10 m
Sound speed bias	± 2 m/s	± 2 m/s

Tab. 2.1: Initial model parameter uncertainties by *Zykov* (2006) were modified for this study.

advantage of shots distributed over an angle range of 360 degree radii around each OBS station (Fig. 1.3). Hence, the positions can be relocated more accurately.

In a first inversion run, the additional clock-drift correction was not applied to the modeling routine, and uncertainty estimates for water depths were set with a high value of 50 m. The inversion converged after four iterations with a data misfit value (normalized χ^2) of 0.92. The normalized χ^2 value equal to 1 represents the optimal goodness of the fit between the observed and modeled travel-times. Another measurement of misfit is the root-mean-square (rms) residual of the travel-times. Those results are certainly higher (10 ms) than the initial picking uncertainty of 1-2 ms.

Although the misfit value was within the acceptance range ($\chi^2 \leq 1$), sometimes overestimating the data and model uncertainties can give a misleading fit value. Therefore, an additional inversion was carried out after reducing the estimated OBS depth uncertainties to 10 m, but keeping the initial uncertainties for OBS and shot positions (Table 2.1). Although the new misfit value was calculated as χ^2= 0.83, rms residuals were still larger than 10 ms for some stations.

Besides the large residual values, OBS stations 1 and 6 showed a linear drift of the residuals with time, or shot number (Fig. 2.5). The drift rates were highest for OBS 6 with a value of 6 ms/day. Hence, a linear drift correction $t_{drift} = b + kT$ was applied as part of the modeling (*T, b* - shot time and drift at the beginning of the survey; *k* - drift rate). Solutions for both coefficients, *b* and *k*, were obtained during the inversion steps.

The inversion converged after four iterations and achieved a slightly better normalized

OBS	X-deploy	Y-deploy	Z-deploy	X-reloc	Y-reloc	Z-reloc	drift-reloc
1	549197	4710691	1632	549091	4710669	1636	108
2	548369	4710455	1634	548230	4710430	1632	142
3	547566	4710280	1633	547369	4710262	1638	198
4	546771	4710045	1633	546630	4710051	1632	141
5	545968	4709842	1637	545792	4709853	1643	176
6	545156	4709629	1638	544987	4709654	1635	171
7	544344	4709407	1643	544164	4709422	1648	181
8	543533	4709212	1623	543344	4709238	1621	190
9	542737	4708998	1645	542563	4709030	1645	177

Tab. 2.2: Deployment coordinates and relocated coordinates with the Zykov code (coordinates are in UTM from central meridian 20 (meters); depths and drift distances are in meters)

χ^2 of 0.86. The rms residuals for all nine OBS stations range between 0.7 and 1.5 ms and are within the uncertainty range of the picks (Fig. 2.6). In general it can be seen that near-offset arrivals result in larger misfit values than far-offset travel-times.

Calculated drifts for deployment positions of the OBS instruments range between 100 m to 200 m in a westward direction from the deployment position (Table 2.2). The relocation algorithm also re-calculates the depths of the OBS instruments (Table 2.2). The calculated depths differ from the deployment depth values obtained from the bathymetric data (multi-beam data) by an average of 3 m. This can be neglected given an average water depth of 1640 m.

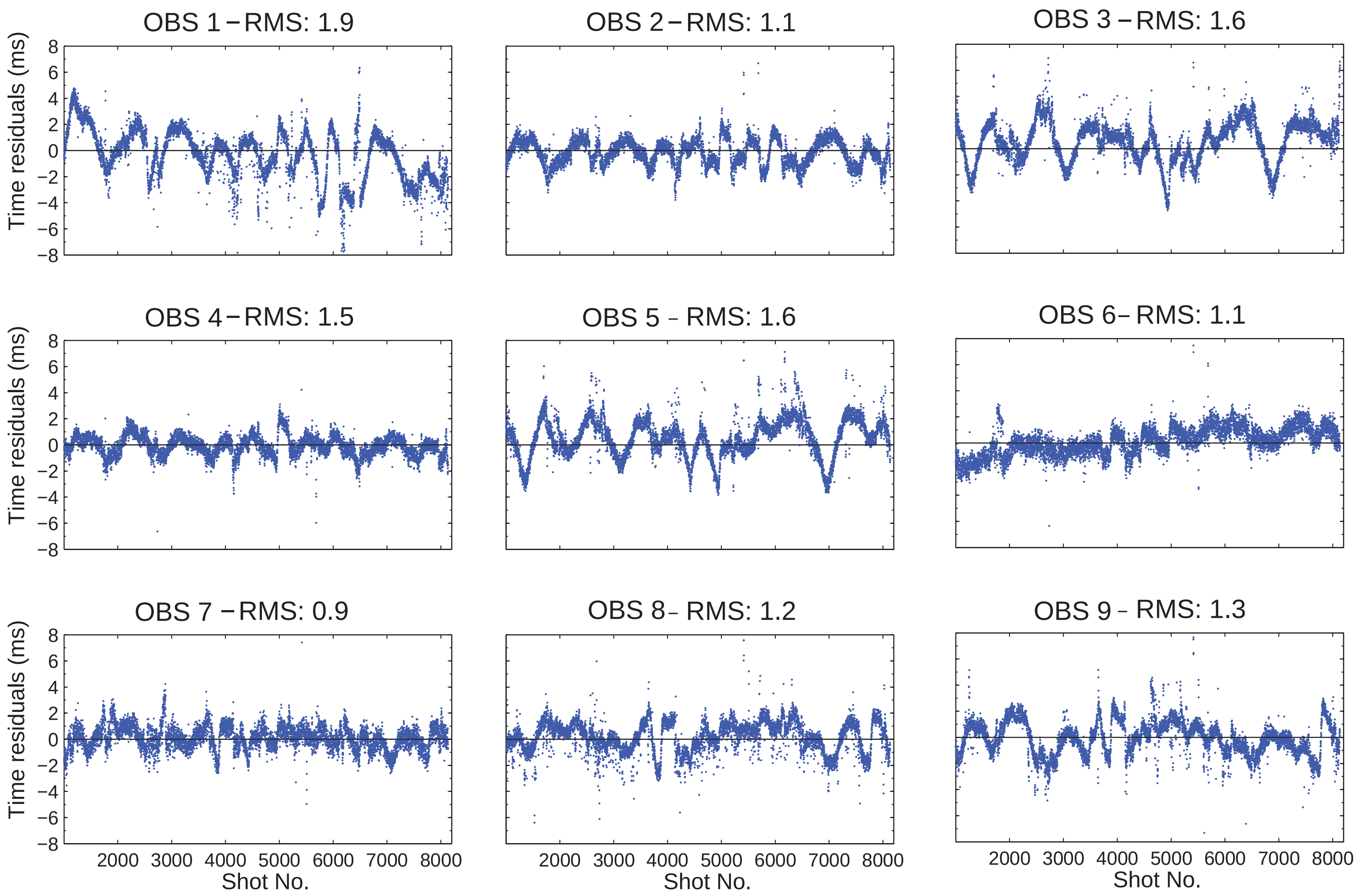

Fig. 2.5: Travel-time residuals after inversion without solving for the clock drift show significant high values for some OBS and also higher values for near-offset shots.

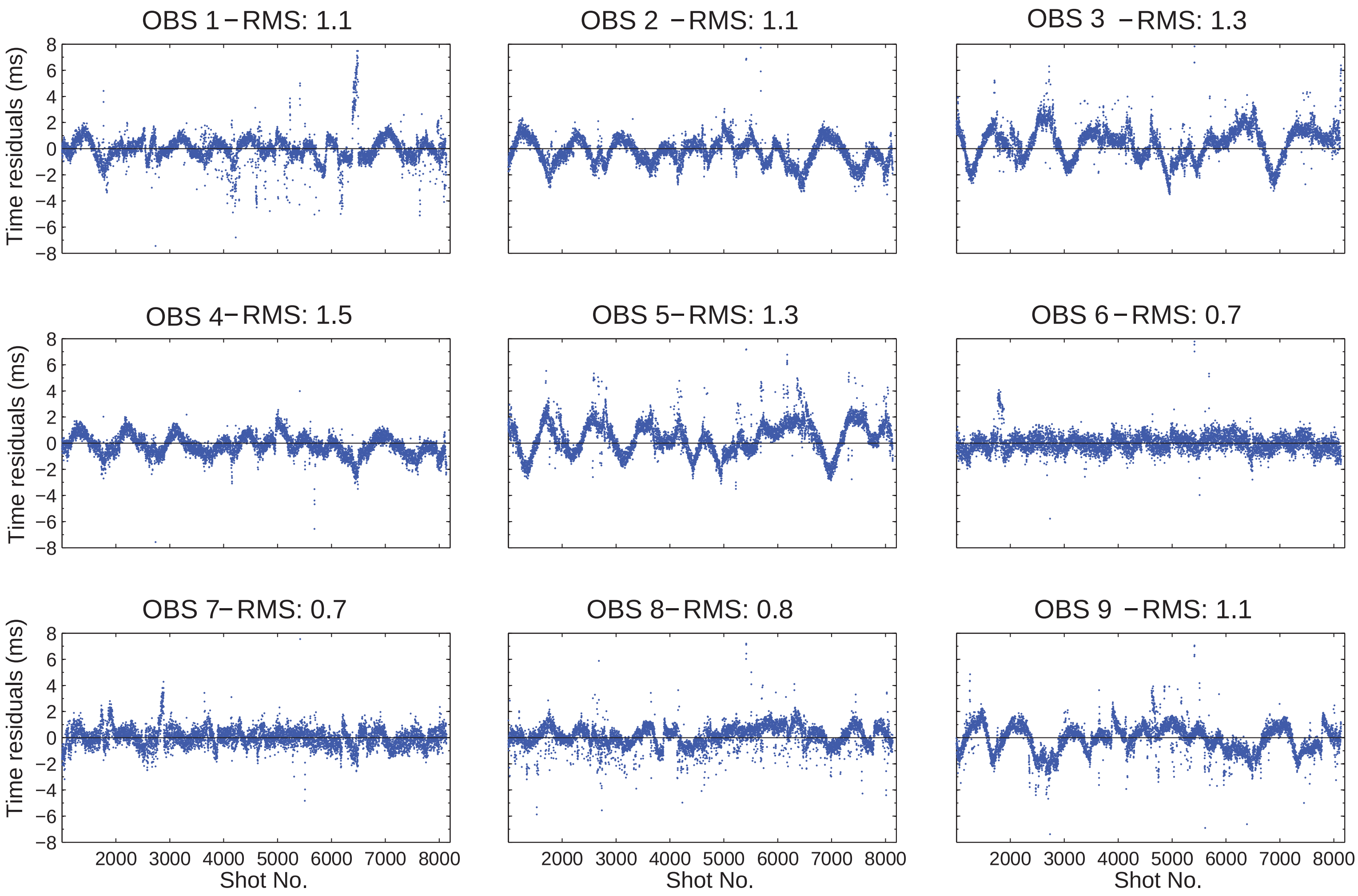

Fig. 2.6: Travel-time residuals after inversion with solving for the clock drift for OBS 1 and OBS 6.

2.3 Data processing of the 2006 2-D SCS reflection data

The 2006 2-D SCS reflection seismic data were recorded with a 61 m long streamer (Teledyne Geophysical Instruments) consisting of six hydrophone groups each with 16 instruments. Within the 50 shot profiles that were recorded during the 2006 survey, only one 2-D SCS reflection profile runs parallel with the OBS array 2 along the slope direction (Fig. 2.7). The same low-frequency (8 Hz) noise already observed on the OBS data (Fig. 2.2) was observed on the 2-D SCS reflection data possibly related to ship noise. The data were filtered with a bandpass (10-250 Hz) similar to that applied to the OBS components. The seafloor and the subparallel reflections below were picked and further used for the combined travel-time inversion modeling with the OBS data (Fig. 2.7). The prominent reflection at 2.6 s (400 ms bsf) was identified as a BSR-like reflection associated with the depth of the BGHSZ. However, the commonly found inverted phase compared to the seafloor arrival was not observed.

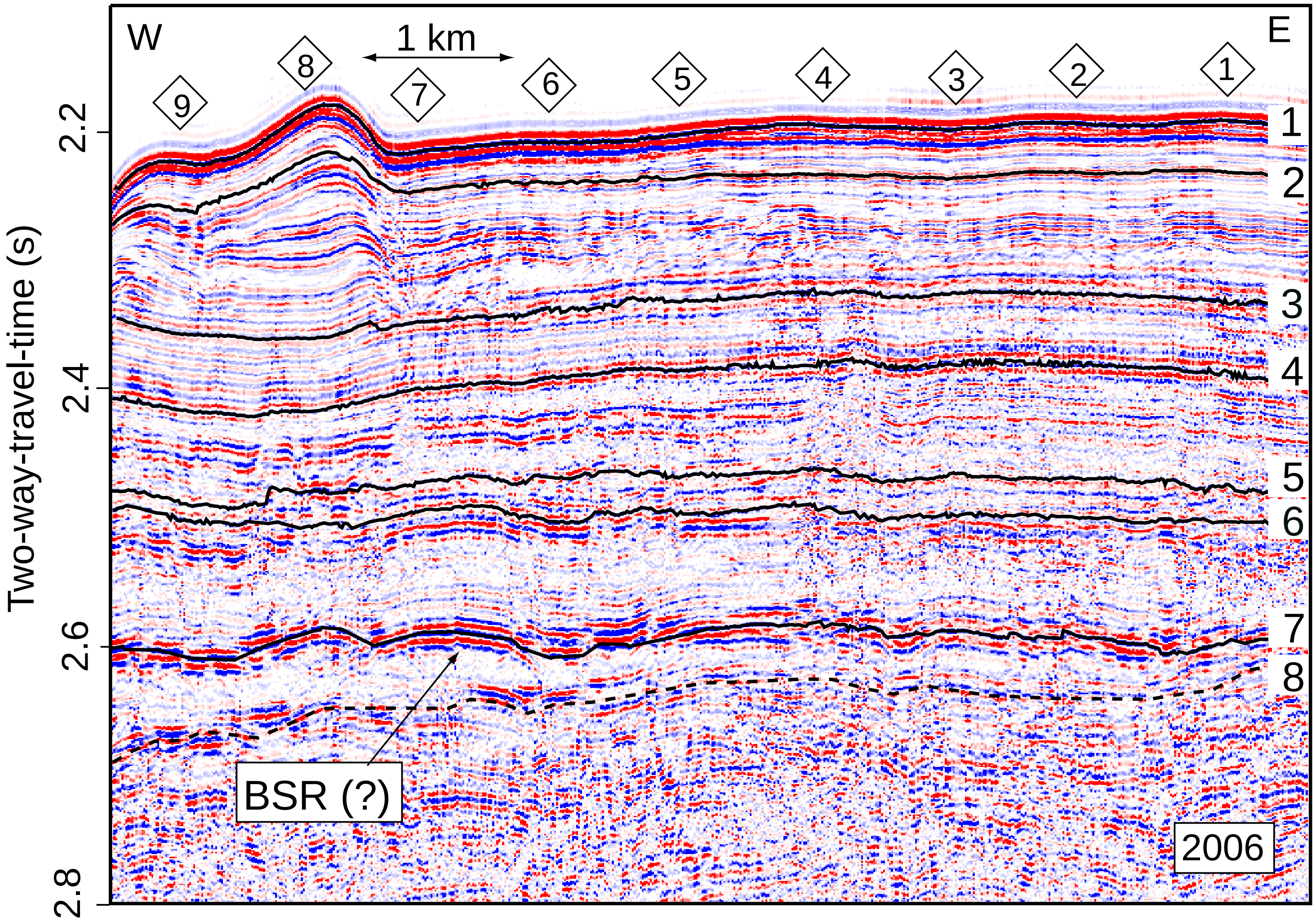

Fig. 2.7: 2-D SCS reflection profile along the nine OBS stations (diamonds) of the western array from the 2006 survey. The profile was filtered with a bandpass (10-250 Hz) and the key reflections sub-parallel to the seafloor were identified. The prominent reflection at 2.6 s (400 ms bsf) was identified as a BSR-like reflection associated with the depth of the BGHSZ; however without the inverted phase compared to the seafloor arrival.

2.4 Processing of the 2004 OBS and 2-D SCS reflection data

Although some processing and modeling on the 2004 OBS data were already applied by J. Cullen (*Cullen et al.*, 2008), re-assessing the data for data quality and recording-time corrections proved useful. The frequency spectrum of a data example (OBS 3 hydrophone) is shown in figure 2.8. The same 8 Hz amplitude peak is observed in the OBS data and in the 2-D SCS reflection data as was recorded in the 2006 data.

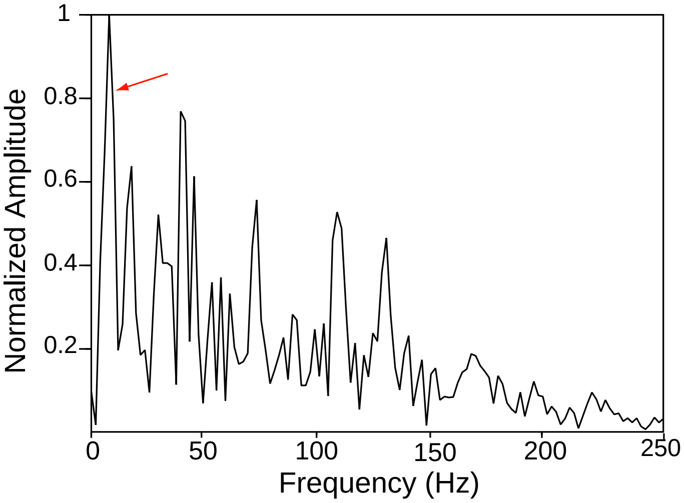

Fig. 2.8: Unfiltered normalized amplitude spectrum of the hydrophone component of OBS 3 from the 2004 survey with low-frequency noise at 8 Hz (red arrow). The main frequency content is around 45 Hz. The time window used for the calculation of the spectrum ranges from 0.8 to 1.3 s and the shot-receiver offset was 185 m.

Hence, the data were filtered with a bandpass of 10 to 250 Hz (Fig. 2.9). A hyperbolic move-out reduction using 1.48 km/s water velocity, was applied to all OBS data to “flatten” the seismic travel-time arrivals of the seafloor-arrival. The sub-parallel reflections below the seafloor can be clearly identified and a prominent reflection at 1.6 s is associated with the BGHSZ. However, the phase reversal expected for a BSR is absent. The bubble pulse is still visible in the filtered data, but does not interfere with the horizon identification.

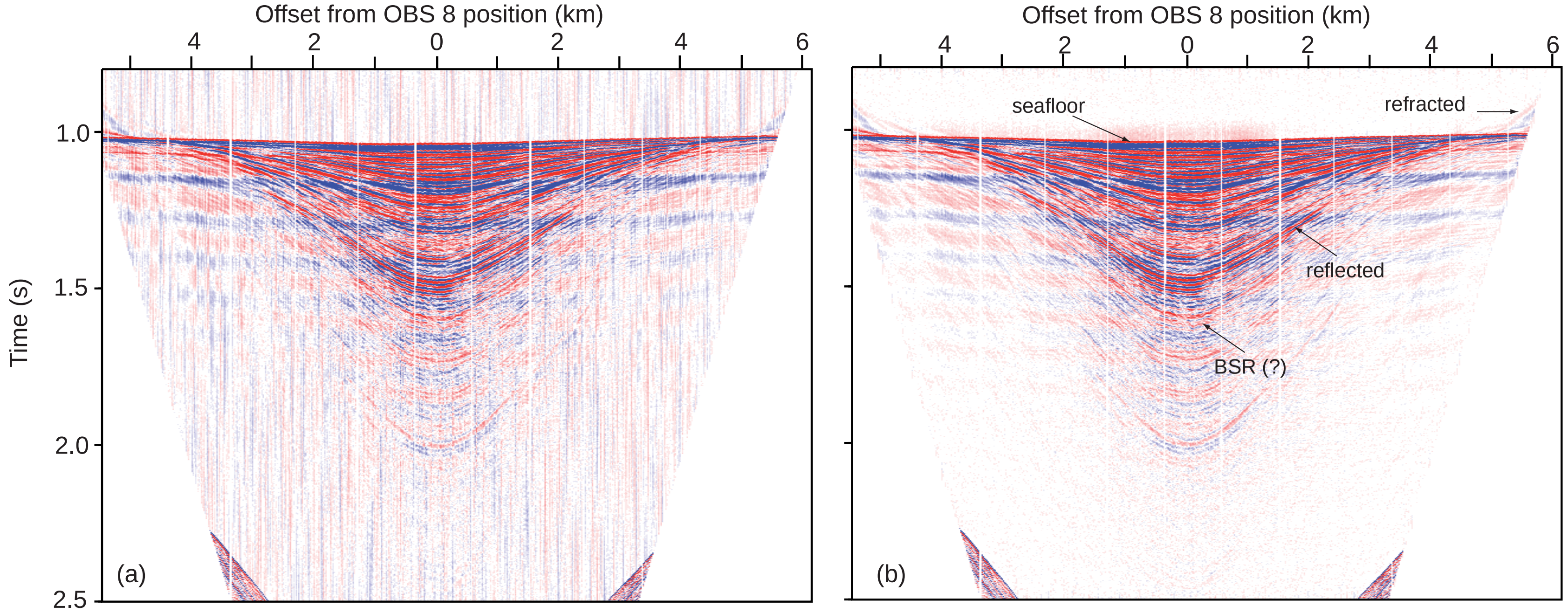

Fig. 2.9: Comparison of (a) unfiltered and (b) bandpass filtered (10-250 Hz) hydrophone OBS 8 data shown with a hyperbolic move-out reduction (1.48 km/s). The prominent reflection associated with the BGHSZ can be identified at a time of 1.6 s. But the reflection lacks the typically inverted phase associated with a BSR.

Similar to the 2006 OBS survey, 2-D SCS reflection data were recorded during the 2004 OBS acquisition. One 2-D SCS reflection profile (9.6 km long) was shot across the OBS positions. This profile was used for arrival identification and initial depth calculations as well as for simultaneous modeling with the OBS data. Similar to the OBS data the 2-D SCS reflection data were bandpass filtered (BP:10-250 Hz). A strong reflection was observed at ~400 ms below the seafloor arrival and was associated with the depth of the BGHSZ (Fig. 2.10). However, the strong inverted phase associated with a BSR is also absent in these data.

2.4.1 Relocation of the 2004 OBS and shot positions

An initial relocation of the OBS deployment positions was already obtained by *Cullen et al.* (2008) with an inversion method developed at the Dalhousie University. Since the 2004 data were compared with the 2006 data and the Dalhousie relocation program did not account for the shot position relocation, recalculating the repositioning with the Zykov code (*Zykov*, 2006) seemed desirable.

The uncertainty estimates for the OBS and shot positions as well as the instruments depths were applied to the routine as for the 2006 relocation scheme (Table 2.1). Convergence was achieved after four iterations and the normalized χ^2 has a value of 0.96. The average travel-time residuals were around 3 ms, twice the residual values obtained with the 2006 OBS data. However, the residual values are within the same range as the estimated picking uncertainties of 2 to 3 ms. The general data quality for the 2004 data is poorer (S/N=5 for refracted arrivals; S/N=15 for reflected arrivals) than for the 2006 data, hence the increased uncertainty value. However, the OBS drifts are smaller (73 to 144 m) compared to the drifts of the 2006 OBSs (100 to 200 m; Table 2.3). This is probably related to the shot-receiver configuration used within this survey. In comparison to the 2006 survey, only 2900 shots were used for the inversion compared to 7133 shots for the 2006 survey.

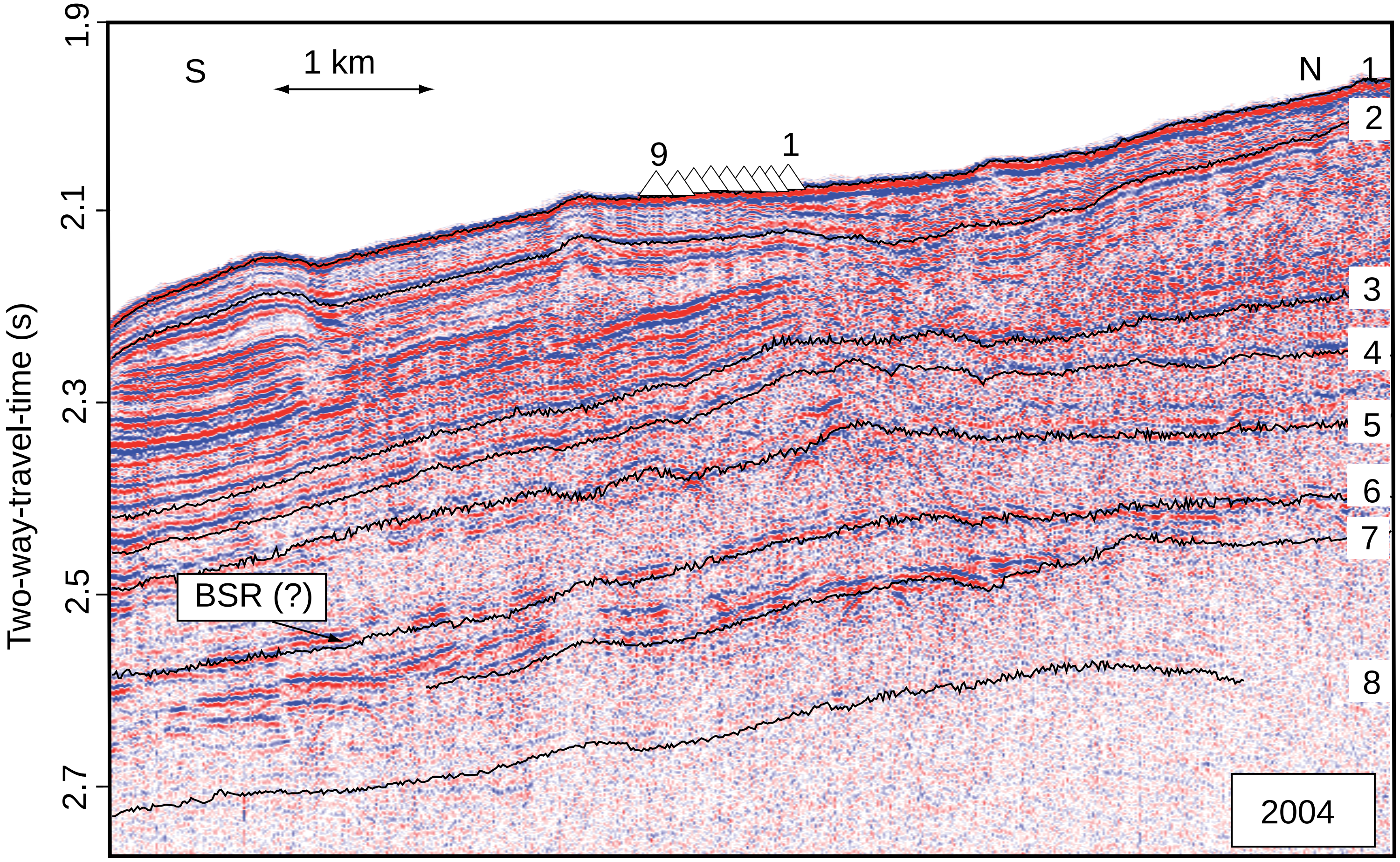

Fig. 2.10: Filtered (BP: 10-250 Hz) 2-D SCS reflection profile coincident with the 2004 OBS shot profile (triangles; numbers indicate OBS number). The reflections that were later used for the travel-time modeling are indicated with numbers, where the prominent reflector depth for the BGHSZ is identified at around 2.6 to 2.75 s TWT.

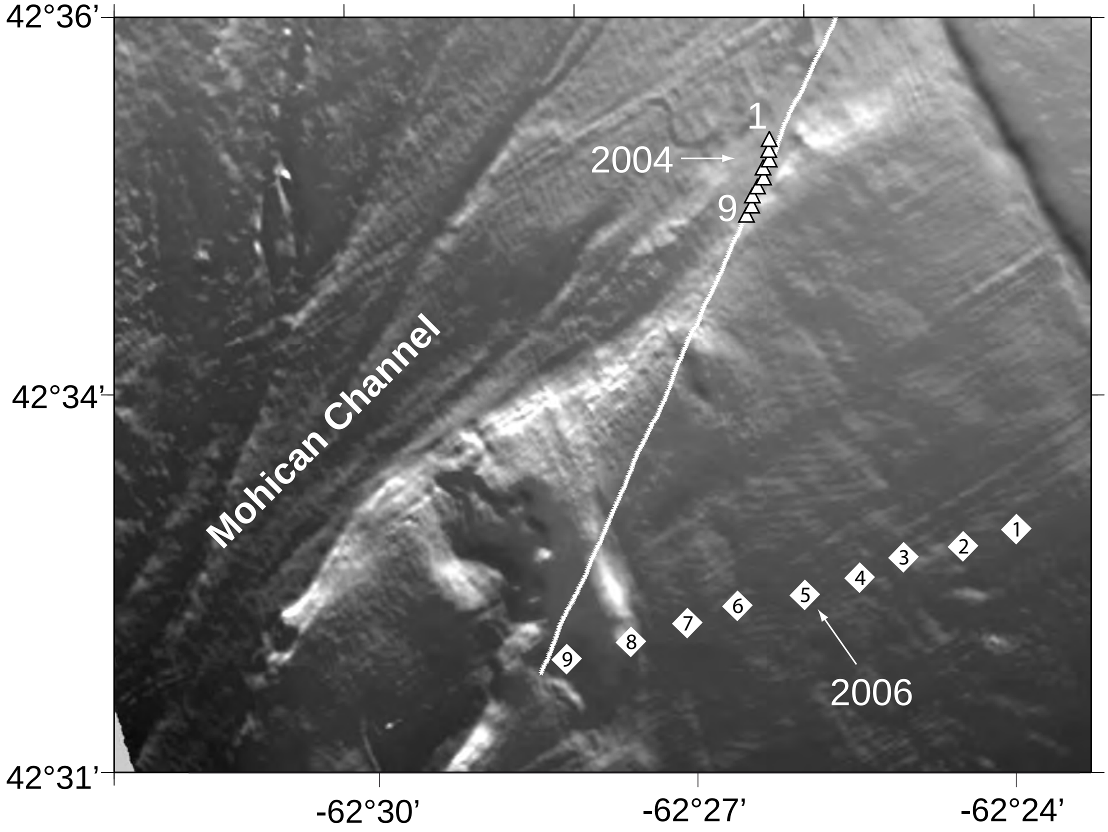

Fig. 2.11: Relocated positions of the nine instruments from the 2004 OBS array (triangles) close to the Mohican Channel and the 2006 OBS array 2 (diamonds). The white line represents the 12 km SCS reflection profile (Fig. 2.10) that was used to identify the primary reflections and for the later-stage travel-time modeling.

Since each OBS stations was not fully surrounded by a high number of shots and shot intervals are larger (20 m) than for the 2006 survey (15 m) (Fig. 2.11), repositioning errors are also larger than for the 2006 survey. Further, water depth values for the single instruments obtained from the bathymetric data (multibeam data provided by D. Mosher (GSC)) differ also from the relocated depth results with an average value of 10 m (Table 2.3). Hence, depths from the bathymetry are certainly more accurate and were used for the travel-time inversion modeling.

OBS	X-deploy	Y-deploy	Z-deploy	X-reloc	Y-reloc	Z-reloc	drift (m)
1	545378	4714546	1542	545312	4714651	1551	124
2	545216	4714212	1541	545124	4714296	1553	125
3	545215	4714323	1542	545171	4714381	1555	73
4	545540	4714880	1538	545491	4715016	1543	144
5	545297	4714434	1543	545222	4714473	1553	84
6	545297	4714434	1542	545280	4714566	1552	132
7	545621	4714992	1538	545569	4715105	1544	124
8	545459	4714658	1540	545370	4714739	1547	121
9	545459	4714769	1539	545422	4714838	1550	78

Tab. 2.3: Deployment coordinates and relocated coordinates of the 2004 OBS data with the Zykov code (coordinates are in UTM from central meridian 20 (meters); depths and drift rates are in meters). Depths for the deployment are extracted from the bathymetry data (multibeam data, D.Mosher) and differ by an average of 10 m from the relocation results for depths.

2.5 Data acquisition and processing of the 3-D MCS reflection data (Encana Ltd.)

A 24-km-long 2-D reflection seismic profile, chosen such that its geometry overlaps with the 19 OBS positions from the 2006 survey (Fig. 1.3 - diamonds, stars), was extracted from the 3-D MCS data cube (Fig. 2.12). The 3-D seismic data were acquired using six streamers each 6 km long. Each streamer consisted of 240 channels with a group interval of 25 m. Shots were fired every 50 m using an array of Bolt® guns with a total volume of 63.4 l. The BSR is visible in these data with an inverted phase compared to the seafloor arrival and following the seafloor topography. However, the BSR is only visible in the western part of the profile, close to the Mohican Channel structure, but fades out into the strong stratigraphic seismic reflectivity to the east. These data were mainly used for identification and interpretation of seismic reflections (horizons) and for comparison with the OBS and SCS reflection data.

The basic processing of the 3-D MCS data was done by ENCANA Ltd.© and included frequency bandpass filtering (3 to 180 Hz), sampling, spherical divergence compensation,

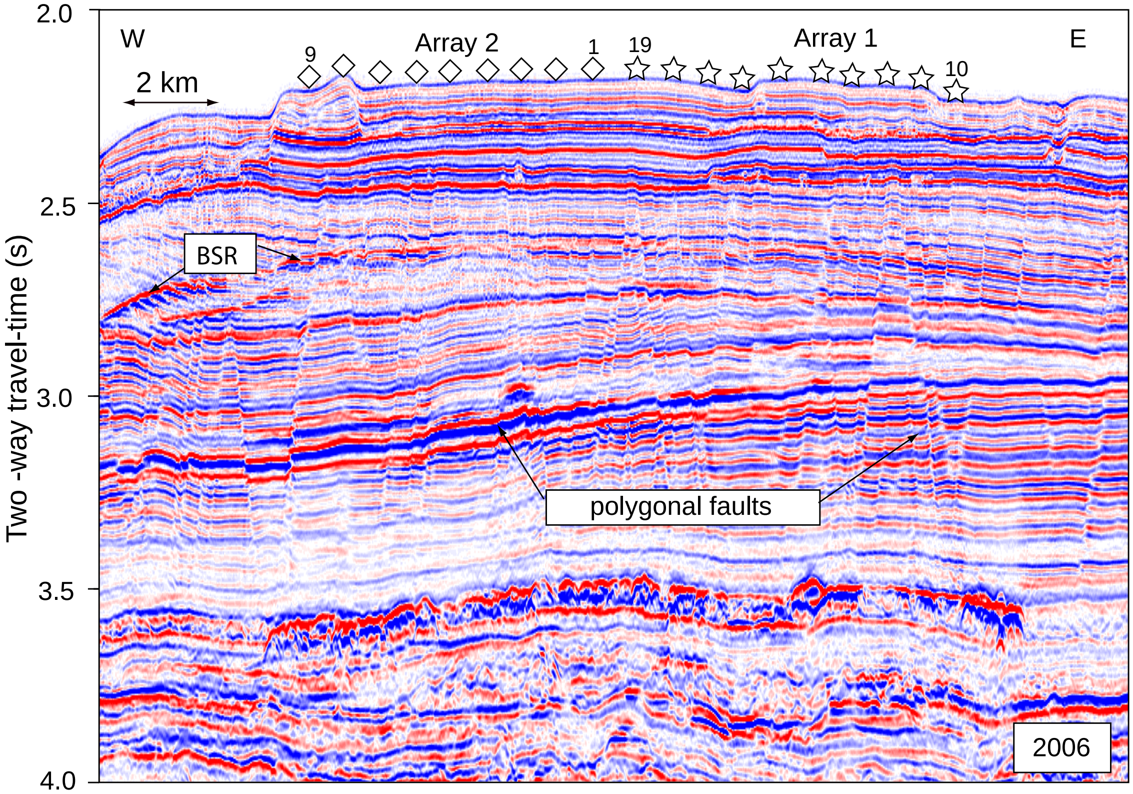

Fig. 2.12: 2-D reflection profile extracted from the 3-D MCS data set provided by EnCana Ltd. covering the 19 OBS stations of OBS array 1 (stars) and array 2 (diamonds). The BSR (indicated) appears close to the Mohican Channel. It is visible in the western part of the line and fades out into the high seismic reflectivity of the strata to the east. The BSR is clearly visible to follow underneath half of the OBS array 2 and is not visible underneath OBS array 1. Strong polygonal faulting is visible within the seismic strata in a range of 2.5 s to 3.2 s.

deconvolution, velocity analysis, multiple attenuation, and pre-stack time migration (reviewed in *Cullen et al.*, 2008).

3. SEISMIC TRAVEL-TIME INVERSION

This chapter reviews the theory and application of travel-time inversion. In the first part the general theory of travel-time modeling is described and the algorithm developed by *Zelt and Smith* (1992) is introduced. The application to data from two different seismic surveys (2004 and 2006) is presented in the second part of this chapter. The results, published in *Schlesinger et al.* (2012), show that travel-time inversion can provide an inexpensive method to obtain valuable velocity information from the subsurface. Estimates on gas hydrate and free gas concentrations are obtained from the modeled velocity values in the last part of this chapter.

3.1 Theoretical background on travel-time inversion methods

Seismic travel-time inversion methods involve the estimation of the velocity structure of the subsurface from the observation of seismic data on the surface. The inverse problem of those methods requires the seismic data information to constrain the earth model. The inversion provides estimates of parameter uncertainty, resolution, and non-uniqueness of the final result.

The algorithm developed by *Zelt and Smith* (1992), which was applied in this study, is widely used for travel-time inversion on wide-angle reflection and refraction data (e.g. *Korenaga et al.*, 1997; *LeBlanc et al.*, 2007; *Lopez et al.*, 2010; *Dash and Spence*, 2011). The method is based on a mathematical approximation of the tomographic reconstruction of the velocity field. Two-dimensional ray tracing through a starting velocity model is performed and seismic travel-times are calculated. Rays are traced through the model between the source and the receiver using zero-order asymptotic ray theory by solving the ray tracing equations (reviewed in *Zelt and Smith*, 1992, Appendix 6.3.1).

The travel-time *t* of a seismic arrival is given by the integral of slowness *s(**r**)* along the corresponding ray-path *L* shown in figure 3.1:

$$t = \int_{L(s)} s(\mathbf{r}) dl \tag{3.1}$$

.

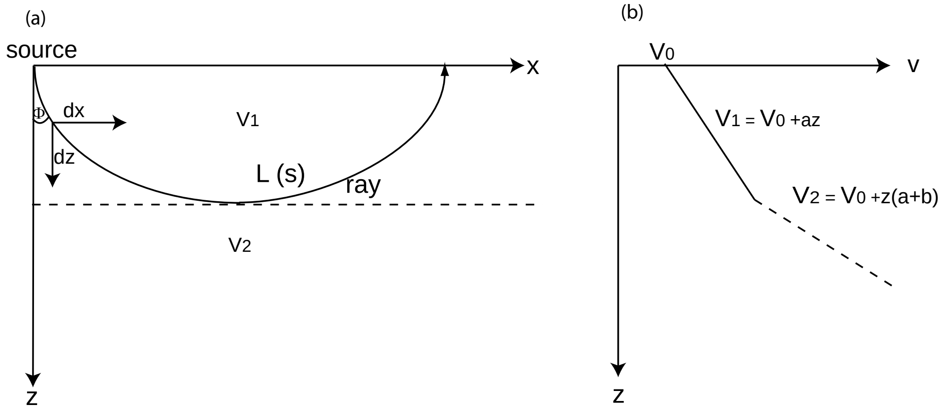

Fig. 3.1: (a) Illustration showing the velocity dependence of the ray-path. Ray (L) is bending due to velocity gradient (b) with $V_2 \geq V_1 \geq V_0$. Φ is the incident angle of the ray.

This dependency of the time on *s(**r**)* is a non-linear problem that can be solved with linearized inversion techniques. Within the inversion procedure presented in this study, the model parameter values are updated to progressively minimize the misfit between the observed and the modeled travel-times in an iterative approach.

Linearization follows Fermat's principle, where the travel-time along a ray-path does not change to the first order when the ray is perturbed. Considering small perturbations

$\delta s(\mathbf{r})$ to the reference slowness $s_0(\mathbf{r})$ the equation 3.1 can be expressed as:

$$t = \int_{L(s_0+\delta s)} s_0(\mathbf{r})dl + \int_{L(s_0+\delta s)} \delta s(\mathbf{r})dl \tag{3.2}$$

and using Fermat's principle, where $L(s_0 + \delta s)$ can be approximated with $L(s_0)$, the integral can be expressed as:

$$\begin{aligned} t &= t_0 + \int_{L(s_0)} \delta s(\mathbf{r})dl \\ \delta t &= \int_{L(s_0)} \delta s(\mathbf{r})dl \end{aligned} \tag{3.3}$$

where δt is the travel-time residual expressed by the slowness perturbation. This linear problem is now solvable.

The equations in 3.3 can be written in a more general matrix form:

$$\delta t = A \cdot \delta m \tag{3.4}$$

$$\begin{aligned} \delta t &= t - t(m_0) \\ \delta m &= m - m_0 \end{aligned} \tag{3.5}$$

where A is a {NxM}-sensitivity matrix containing the partial derivatives of the travel-times with respect to the model parameters (velocities, depths) $(\frac{\delta t_i}{\delta m_j})$ (i=1,..,N; j=1,...,M). The small perturbation of the starting model m_0 is expressed by δm. The travel-time residual vector δt represents the difference between the actual measured travel-times and the modeled travel-times. This term also shows the reorganization of the non-linear problem to a linear problem that is solvable.

The velocity model is parametrized through a series of blocks with varying velocities allowing sharp velocity contrasts between the blocks (Fig. 3.2). Each travel-time arrival is subjectively identified with a specific phase according to a reflector depth. This method allows modeling and simultaneously inverting for first and secondary reflections as well as refractions. The algorithm by *Zelt and Smith* (1992) can invert for travel-times from wide-angle reflections (OBS data) simultaneously with travel-times from vertical-incidence reflections (SCS data). Within each iteration any or all model parameters can be selected for inversion. The algorithm uses three different types of rays for the ray-tracing approach (Fig. 3.3): (1) Reflected rays from the layer boundaries, (2) turning rays that occur while velocity increases monotonically with depth, and (3) head-waves, which enter and exit a block at the critical angle and travel along the upper boundary of the block.

The information to generate the starting model for the inversion that contains velocity and depth information, can be extracted from 2-D seismic velocity analysis of MCS data, or from the analysis of sonic-logs, or from previous model results. Although the model can be rough and blocky it should be chosen carefully since the linearization assumption requires that the starting model is reasonably close the the "true" earth model. It is often useful to test several starting models in order to obtain the best-fit to the data.

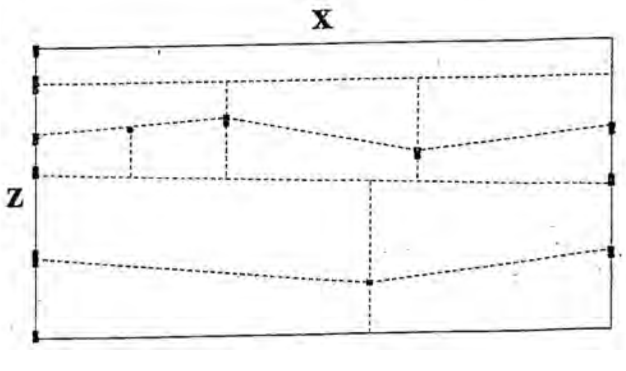

Fig. 3.2: Model parametrization examples of some random trapezoidal blocks separated by vertical boundaries are. These blocks can be arbitrarily sized and shaped. (modified from *Zelt and Smith*, 1992)

Although the linear problem is now solvable, the inverse problem is still ill-conditioned,

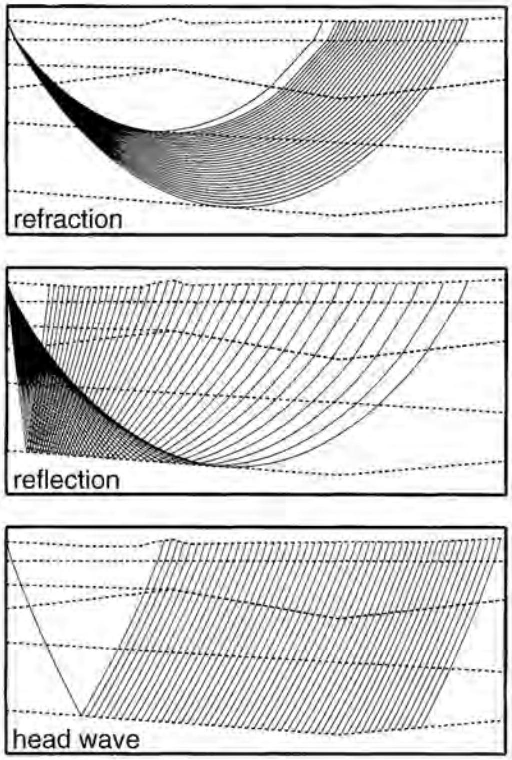

Fig. 3.3: Different types of waves that are modeled via ray-tracing (from top tom bottom): turning waves, reflected waves, and head-waves. (modified from *Zelt and Smith*, 1992)

where the solution is either non-unique or non-stable. In reality, this is due to noise in the data and errors both from the measurements and the model approximations. Regularization of the solution is an effective approach to deal with the ill-posed problem by including *a priori* information (e.g., uncertainty estimates). Additional constraints are imposed that control the under-determined part of the solution. The regularization minimizes an objective function:

$$\begin{aligned}\Phi(m) &= (A\,m - d)^T\,C_d^{-1}\,(A\,m - d) + \lambda\,(m^T H m) \\ &= (Am - \delta t - Am_o)^T\,C_d^{-1}\,(Am - \delta t - Am_0) + \lambda\,(m^T H m)\end{aligned} \qquad (3.6)$$

where the data misfit (Φ) is defined by the data residuals (δt) and the data covariance matrix

$C_d = diag\{\sigma_i^2\}$, the diagonal matrix of the standard deviation values of each data value. The trade-off parameter λ controls the weighting of data information versus to the *a priori* information expressed with the regularization matrix H.

The damped-least squares (DLS) method is a form of regularization that is implemented into the inversion routine of this algorithm (*Zelt and Smith*, 1992). The solution of the problem is sought by minimizing the data residuals. Following equation 3.5 and 3.6, the DLS solution can be written as:

$$\delta m = (A^T C_d^{-1}\, A \, + DC_m^{-1})^{-1} A^T \, C_d^{-1} \, \delta t \tag{3.7}$$

where *D* is the damping parameter, usually set equal to 1 (*Zelt and Smith*, 1992). C_m and C_d are the diagonal model and data covariance matrices under the assumption of uncorrelated errors ($C_d = diag\{\sigma_i^2\}$; $C_m = diag\{\sigma_j^2\}$). The standard deviation σ_i is the estimated uncertainty of the i^{th} travel-time measurement and σ_j is an *a priori* estimate of the j^{th} model parameter's uncertainty.

3.2 Travel-time inversion applied to the 2006 OBS and 2-D SCS reflection data

The seismic travel-time algorithm described above was applied on the 2006 OBS and 2-D SCS reflection data. In general the wide-angle and refraction data provided accurate velocity information, while the vertical incidence (SCS) data gave a high resolution control on the subsurface structure. As already mentioned in chapter 2, the original data were processed using the SU routines and travel-time arrivals of each OBS were picked using the software Kingdom Suite (©Seismic Micro-Technology Inc.).

3.2.1 Data handling

The reflected arrivals identified in the 9.6 km long SCS profile were used to constrain the identified reflected arrivals in the OBS data (Fig. 2.7, Chapter 2.3). To improve the signal-to-noise ratio of the SCS data a zero-phase bandpass filter (10-250 Hz) was applied prior to the comparison of seismic arrivals (Fig. 3.4).

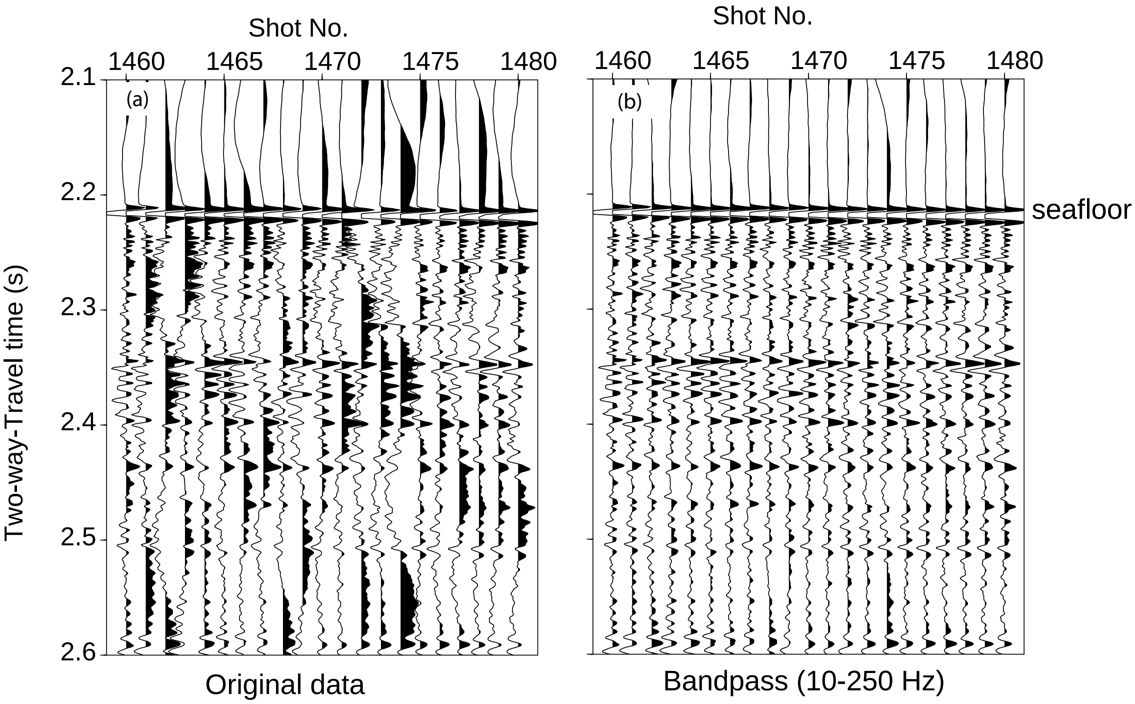

Fig. 3.4: Comparison of (a) an original unfiltered 2-D SCS reflection data section and (b) the bandpass-filtered (10-250 Hz) section. The shot-spacing is 15 m.

The OBS data were filtered to better identify the seismic arrivals, but the picked arrival times were obtained from the unfiltered data to capture the original seismic waveform. Comparison of SCS and OBS data showed an inconsistency between the direct arrival times at vertical incidence in the OBS data and the corresponding seafloor reflection travel-times in the SCS data. However, the OBS data were assumed to be accurate based on the relocation analysis for the OBS positions (Chapter 2.2.1). Therefore, the 2-D SCS reflection data were time-shifted by 80 ms to an earlier arrival time to match the OBS data.

3.2.2 Selection of reflections and refractions for the travel-time modeling

In a first approach, the reflections were selected in the 2-D SCS reflection profile and compared to reflections in the 2-D MCS reflection profile (Fig. 2.12; EnCana© 3-D MCS data). Only a few horizons that could be clearly identified in both data sets were chosen. In a next step, those reflections were compared with and identified in the OBS data. A hyperbolic move-out using the water velocity (1.48 km/s) was applied to the OBS data to "flatten" the seafloor and shallow sub-seafloor reflections. Thereafter, coincident portions of the SCS data, OBS data, and the 3-D MCS data were compared at all nine OBS locations. The OBS and 2-D SCS reflection data were filtered with a bandpass of 10-60 Hz to be comparable with the 3-D MCS data (Fig. 3.5).

Two refracted arrivals were identified in the OBS data (Fig. 3.6). The first-arrival refraction has an apparent velocity of 1.82 km/s and was identified on all OBSs except for OBS 7 for which the data was lower quality. To compare the refracted arrivals with the already identified reflections, a linear move-out with the apparent velocity of 1.82 km/s was applied to the data.

The second refracted arrival was identified on only four OBSs (2,6,8, and 9) with an average apparent velocity of 2.4 km/s (Fig. 3.6). The depth of that refraction could not be constrained by reflections, neither in the 2-D SCS reflection data nor in the OBS data. The origin of the refraction appears to be deeper than the model depth and therefore it was not included into the velocity modeling at this point.

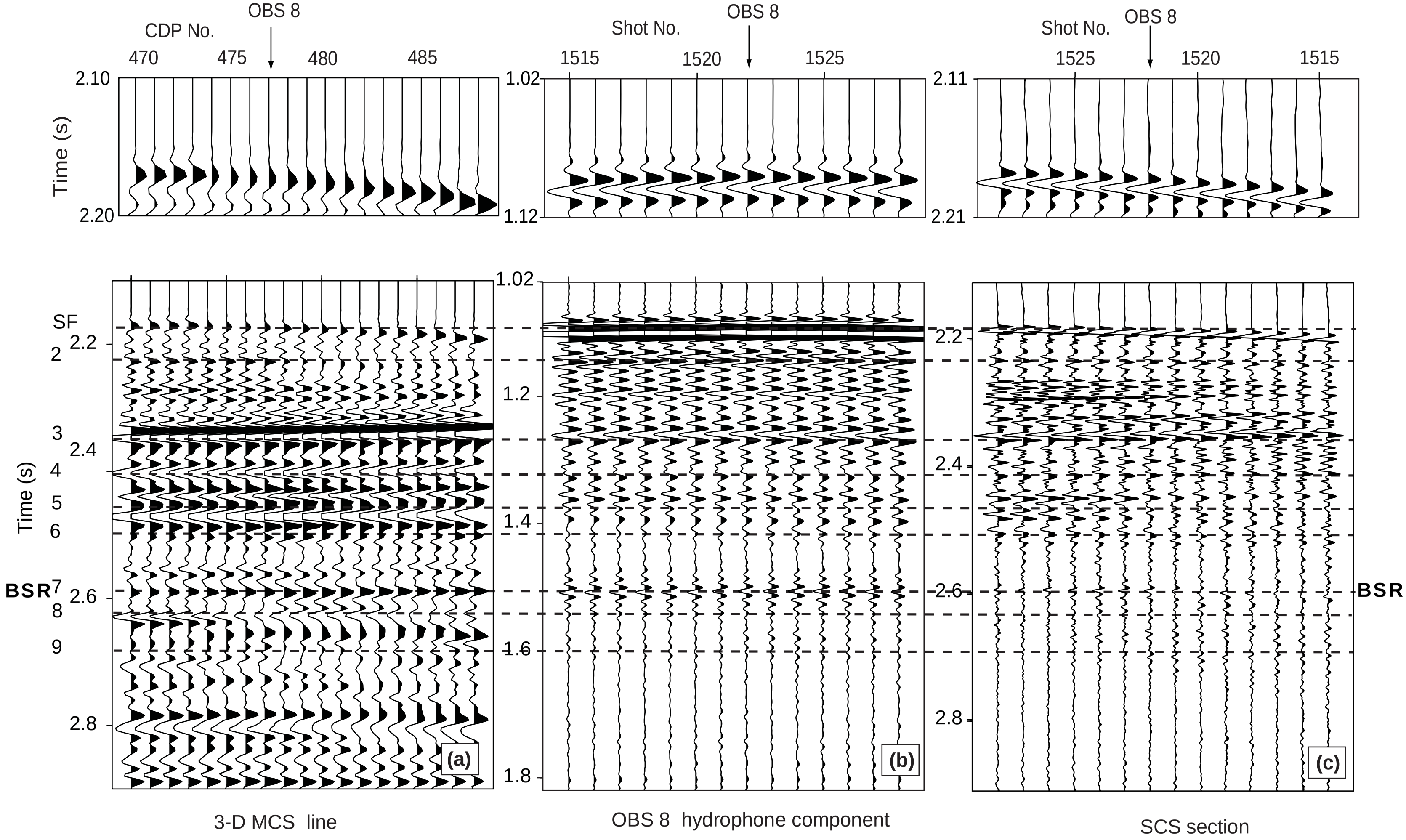

Fig. 3.5: (a) Comparison of 3-D MCS data from Encana Ltd., (b) OBS 8 hydrophone component, and (c) 2-D SCS data section at the OBS 8 location. All data sets were filtered with a bandpass of 10-60 Hz. Seismic reflections were identified in all data sets whose arrival times were applied in the travel-time inversion. The reflection marked between horizon 7 and 8 is associated with the BGHSZ. However, the inverted phase signal identified with a common BSR, is missing for this reflection. Shot spacing is 6.25 m for the 3-D MCS section and 15 m for the OBS and SCS data.

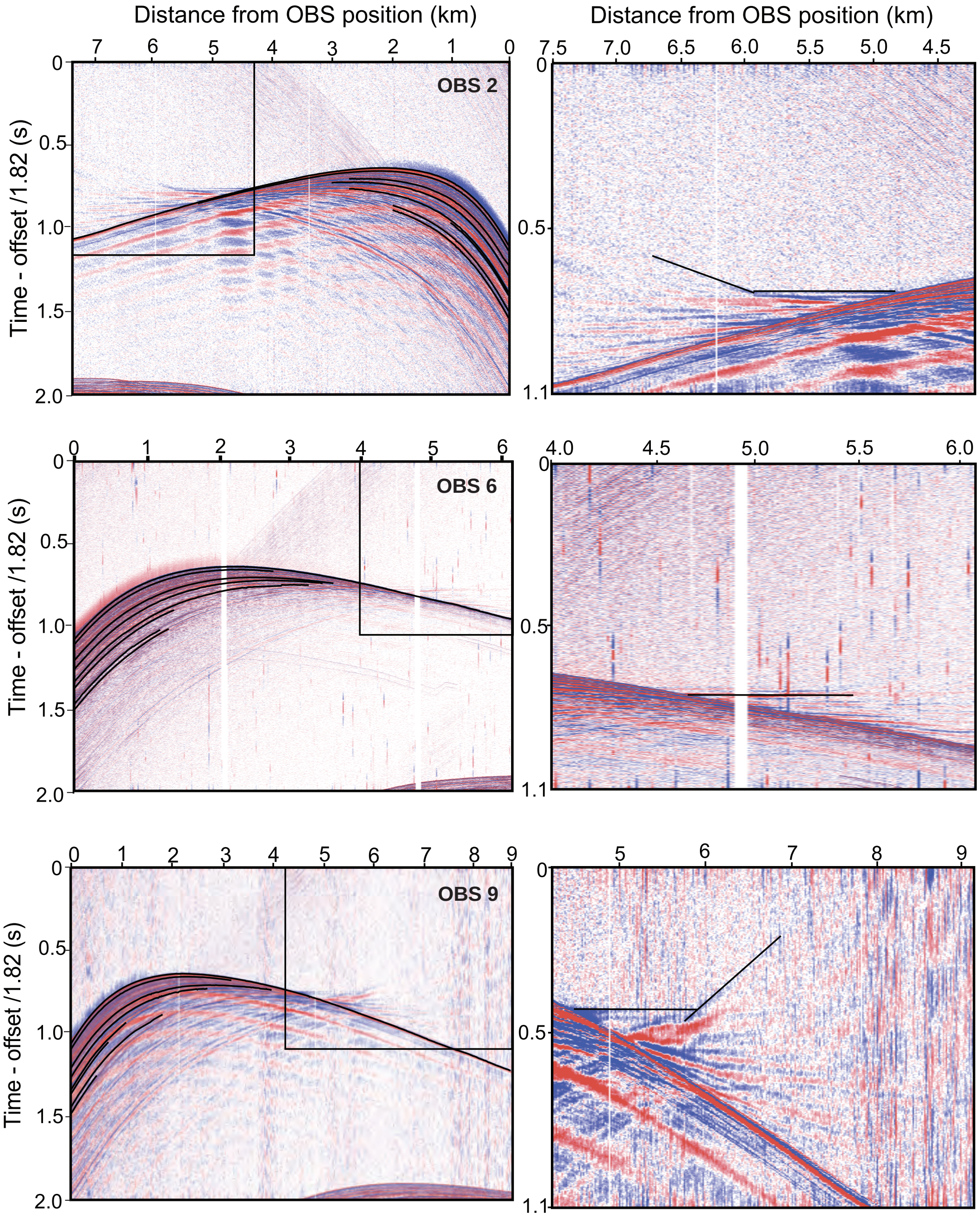

Fig. 3.6: Seismic data (BP: 10-250 Hz) of three selected OBSs (2,6,9) displayed with a reduced velocity of 1.82 km/s. The identified reflected and refracted arrivals are plotted within the OBS data. Right-hand side shows a blow-up of the identified refractions.

3.2.3 Travel-time forward and inverse modeling

Seafloor reflection and direct arrival:

Since the first four OBSs were located on the eastern side of the 10.5 km shot profile, a greater number of shots was recorded west of the instrument's positions, and so the reflected and refracted arrivals were identified to greater offsets (~6 km) to the west. With OBS 5 in the middle of the profile, reflections out to 4 km offset on each side of the OBS position were identified. The western side of the profile was modeled mainly with reflections from OBS 6 to OBS 9 out to offsets of 5 km. The reflections were identified and picked using the downward layer-stripping approach starting with the seafloor arrival and continuing to the next deeper layers (e.g. *Gray and Golden*, 1983).

Based on the S/N ratio for the reflected arrivals (e.g., S/N=11 for OBS 2), each identified arrival for the OBS and 2-D SCS reflection data was assigned an uncertainty for the picked time. The direct arrival travel-time picks were given an uncertainty of 1.5 ms for the OBS data (1 ms sampling rate) and 3 ms for the arrivals obtained from the 2-D SCS data due to a lower signal-to-noise ratio (e.g. S/N=3).

Both direct arrival travel-times of OBS data and the seafloor arrival times from the 2-D SCS reflection data were modeled. The misfit between the observed and modeled travel-times can be expressed by (1) the rms residual travel-time and (2) the normalized χ^2. For the OBS data both values were calculated with 1.2 ms rms misfit and a χ^2 of ≤ 1 (Fig. 3.7 a,b). For the SCS data, the rms misfit is 3 ms and χ^2 is 1.05 (Fig. 3.7 c,d).

Layers 2 to 4:

The pick uncertainty estimates for the next three reflections were assigned as 2 to 2.5 ms for the OBS data and 3 ms for the 2-D SCS reflection data picks. The calculated rms misfit values obtained from the simultaneous inversion of the OBS and SCS data for all three interfaces were small: 2.3 ms rms misfit for interface 2 and up to 3 ms for interface 4.

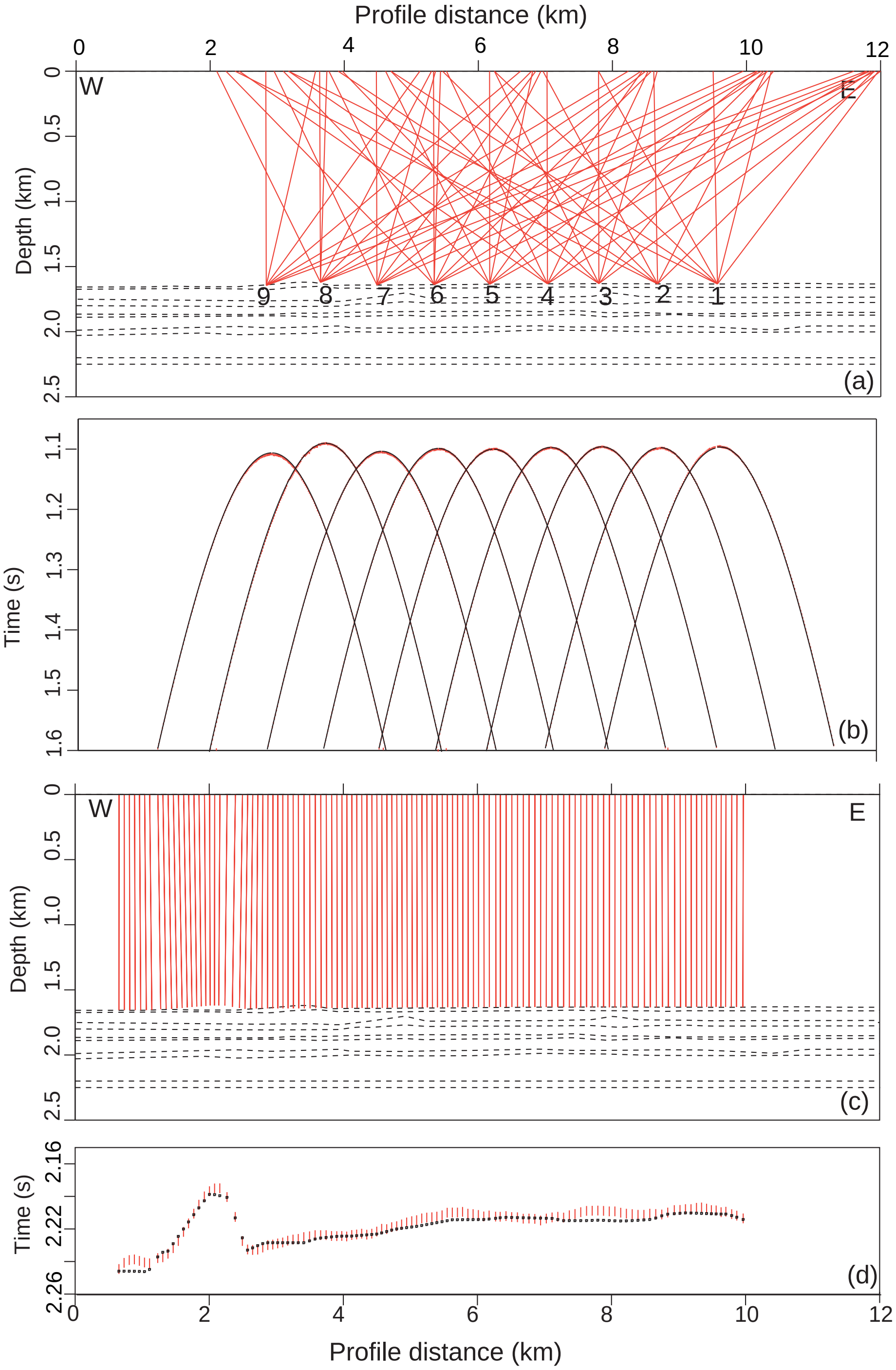

Fig. 3.7: Ray-tracing through model with first-arrivals from the nine instruments from 2006 OBS array 2 data (a) and 2006 2-D SCS reflection data (c). Modeled travel-times (black) and observed travel-times (red) are compared for the OBS data (b) and the 2-D SCS data (d). The observed arrivals are displayed with the length of the bar equal to twice the uncertainty of the picked travel-times (OBS data: ±1.5 ms; SCS data: ±3 ms). For better visibility of the rays, every fifth shot was displayed for the SCS data.

For an overall comparison of the input data (number of picks), uncertainty estimates, and calculated misfit values for all interfaces see tables 6.1 and 6.2 in the appendix. The first table shows all values obtained while inverting OBS data only. The second table shows the results from combined inversion of OBS and SCS data. However, reflections deeper than layer 7 could not be identified and modeled from the SCS data . Hence, only the first seven layers are listed in both tables.

Layer 5 reflection and refracted arrivals:

Reflected arrivals from the fifth interface were picked on the OBS data and SCS data with assigned uncertainties of 2.5 ms and 3 ms, respectively. Forward and inverse modeling of the reflected arrivals from interface 5 were matched with the travel-times of the first refraction and picked on some of the OBS data (Fig. 3.8). Picking uncertainties for the refracted travel-time arrivals were assigned as 2.5 rms.

Inversion results show that the rms misfit values were 2.5 ms for reflected and refracted arrivals from the OBS data. A combined inversion with the travel-time picks from the SCS data resulted in a rms misfit of 3.9 ms. The velocity within layer 5 ranges from 1.65 to 1.7 km/s. The refracted arrivals travel through the top of layer 6 with an apparent velocity of 1.82 km/s.

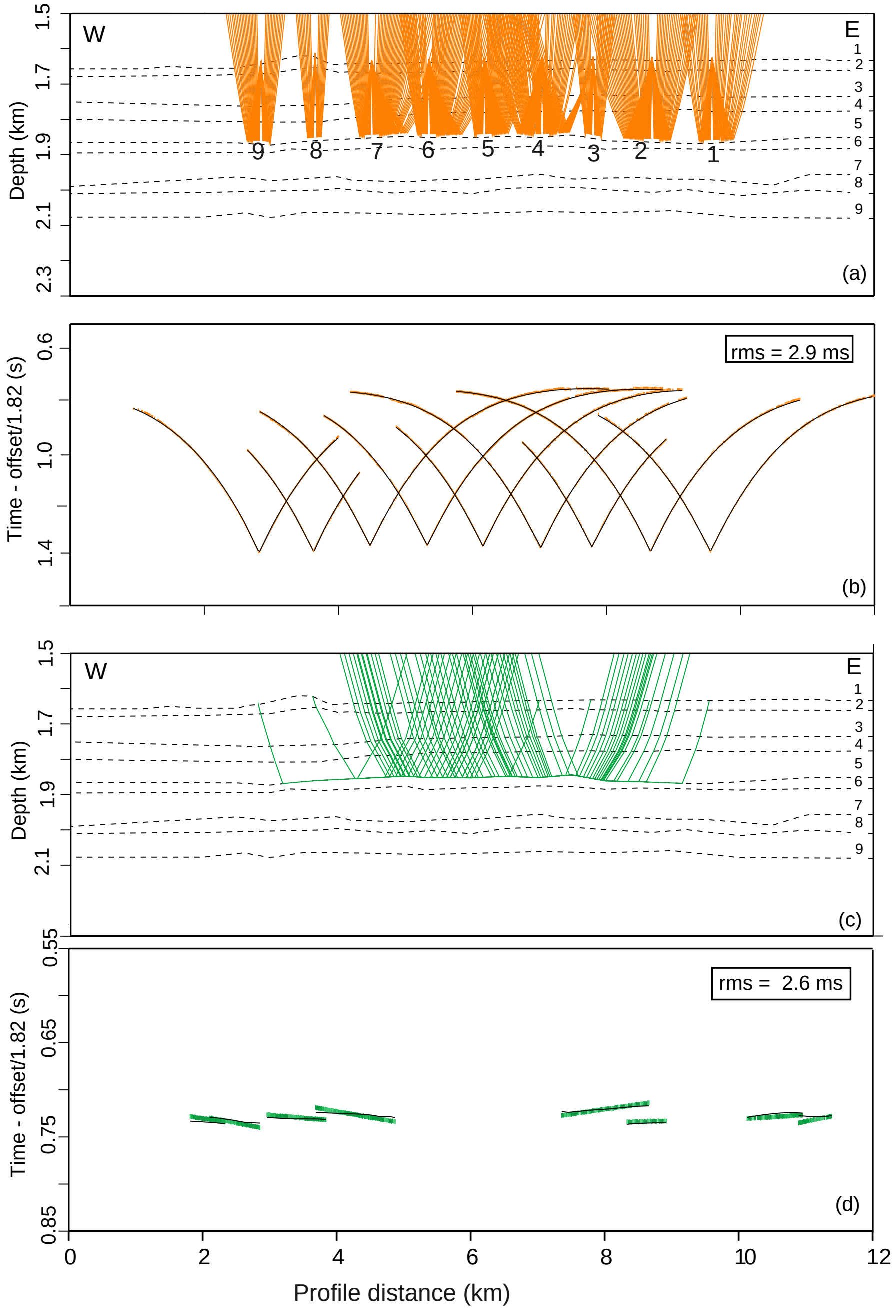

Fig. 3.8: (a) Ray-tracing for arrivals of interface 5 are displayed. (b) Modeled travel-times (black) and observed travel-times (red bars with uncertainty of 2.5 ms) of the OBS reflections from interface 5. (c) Ray-tracing of the refracted arrivals with an apparent velocity of 1.82 km/s from the top of interface 6. (d) Modeled (black) and observed travel-time arrivals for refractions from the top of interface 6 (pick uncertainties: 2.5 ms). Refracted travel-times (d) are shown with linear move-out correction (1.82 km/s).

Layers 6 to 8:

The velocities of layer 6 were modeled with 1.82 km/s in the central part of the profile with indications of higher velocities (> 1.9 km/s) at both ends of the profile. The rms misfit values of 1.5 ms for the OBS data picks and 4.2 ms for the combined inversion with the SCS data were achieved. Although the modeled layer thickness of layer 6 was only ~40 m, the next deeper layer 7 had a greater thickness (~100 m) but similar velocities (1.81 to 1.84 km/s). Thus, the transition to higher velocities over this depth range is well-established with a velocity increase of 140-190 m/s.

The high-velocity layer extends downward to interface 7 at a depth of ~330 mbsf. This depth was formerly identified as the BSR depth in the 2-D SCS seismic data and the 3-D MCS reflection seismic data sets (*Mosher*, 2004; *Cullen et al.*, 2008). However, the BSR could not be clearly assigned to either interface 7 or 8 as both reflections are only 50 ms apart from each other and neither of them shows a clear indication of the inverted phase signal typically found with BSR observations (Fig. 3.5). However, the BGHSZ is associated with these reflector depths.

Travel-time pick uncertainties were assigned as 2.5 ms for the OBS data and 3 ms for the SCS data for both reflections. The starting depths and velocities of layers 7 and 8 were chosen to match the general velocity trend following the values of the previous interfaces. Combined inversion of OBS and SCS data showed that velocities of layer 8 were slightly decreasing to 1.74 km/s within this ~30 m thin layer. However, the depth of layer 8 was not fully constrained with the 2-D SCS data, as the reflection could not be clearly identified in the SCS data. The misfit values for the combined inversion with OBS and SCS data were achieved with a rms misfit of 4.2 ms for layer 7 and 3.7 ms for layer 8.

Layer 9 and deeper reflections and refractions:

Identification of deeper reflections on the OBS data was successful on some of the OBSs, whereas the 2-D SCS data did not show deeper reflections than reflector 8. However, a deeper reflection 9 was identified on all the OBSs and modeled with a layer thickness of ~80 m that was not constrained by the 2-D SCS data. The assigned pick uncertainty was set to 2.5 ms. A small velocity increase (90 m/s) from 1.74 km/s for layer 8 to 1.85 km/s for layer 9 was modeled with the OBS data. The achieved rms misfit value for arrivals from interface 9 was 2.6 ms.

As shown in the final velocity model result (Fig. 3.10), the modeled layer 10 defines the whole range below layer 9 with a velocity assigned as 1.9 km/s. However, a secondary refracted arrival can be identified on some of the OBS data (OBSs 2, 6, 8, and 9) with an apparent velocity of ~2.4 km/s. This arrival is refracted from a layer interface deeper than the modeled range (Fig. 3.10) and was not matched to the reflections above. Hence, it was not included into the final modeling approach.

The modeled travel-times and corresponding picked arrivals from the seismic data are shown in figures 3.6 and 3.9. The final values for velocities and depths are shown in figure 3.10, where the diamonds represent the nine OBS positions at the seafloor. The model shows strong lateral velocity changes, especially for the high-velocity region (layer 6). Thus, the final velocity model was compared to the migrated section of the 2-D SCS reflection data (see Appendix: Fig. 6.2). The velocity variations correlate with enhanced reflectivity in some parts of the data.

Comparison of ray coverage

The travel-time arrivals from near-offset shots were clearly identified on the OBS data and picked for the travel-time inversion scheme. However, arrivals originating from larger shot-receiver offsets were often more difficult to identify and less visible in the seismic data. Hence, those arrivals were often not chosen for the travel-time inversion and a more conservative picking approach was followed.

The ray coverage of arrivals from neighboring stations increases with depth as shot-

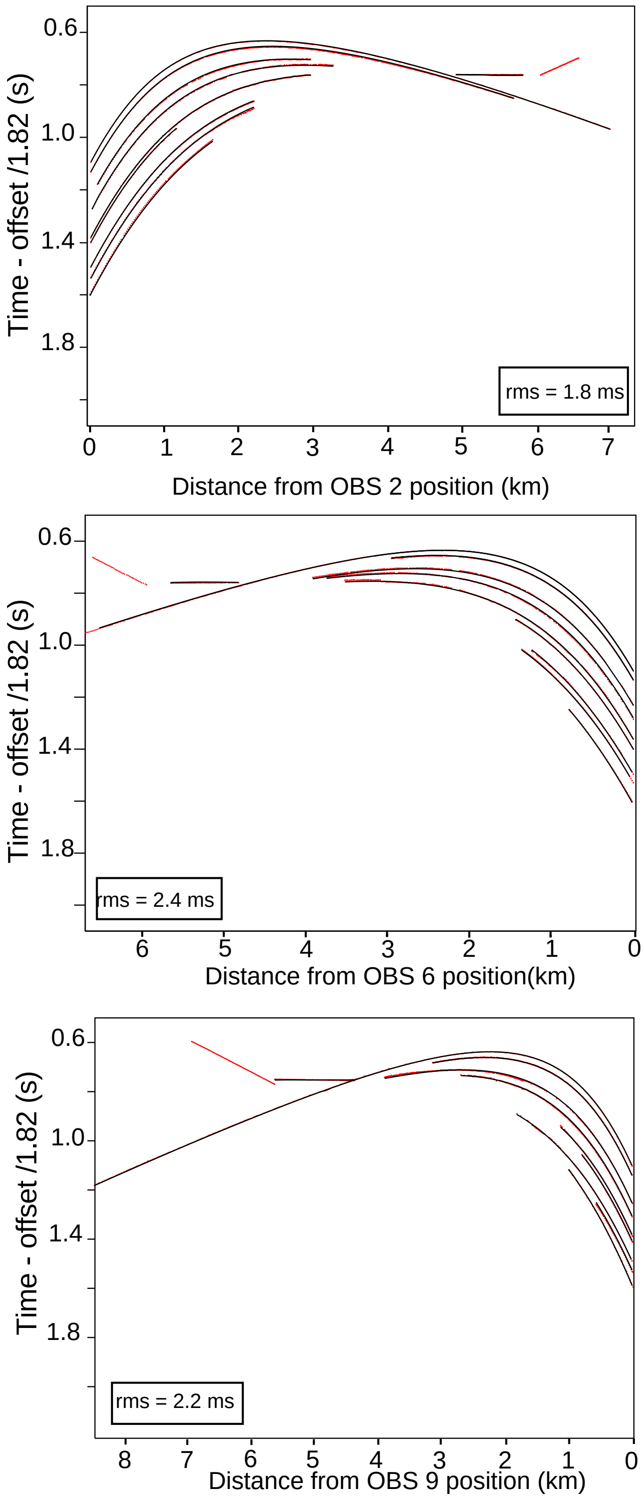

Fig. 3.9: The modeled (red) and observed seismic travel-times (black) of three OBSs (2, 6, 9) are shown with a reducing velocity (1.82 km/s). The identified horizons correspond to those picked in the OBS data (Fig. 3.6)

receiver offsets become greater. The 2006 OBS instruments were spaced at ~900 m. Normally, the portion of a horizon illuminated by rays is larger for deeper horizons than for shallower horizons. However, a deeper horizon may have good quality picks over a more limited offset range than a shallower horizon, and so it is possible that a deeper horizon is imaged over a more limited extent. For example ray-tracing for arrivals from interface 4 show a more continuous ray-coverage than arrivals traced for interface 6 (Fig. 3.11 a, 3.11 b). But because we followed a more conservative approach by not picking highly uncertain large-offset arrivals, the rms misfit value for layer 6 is smaller than for layer 4 (Table 6.1).

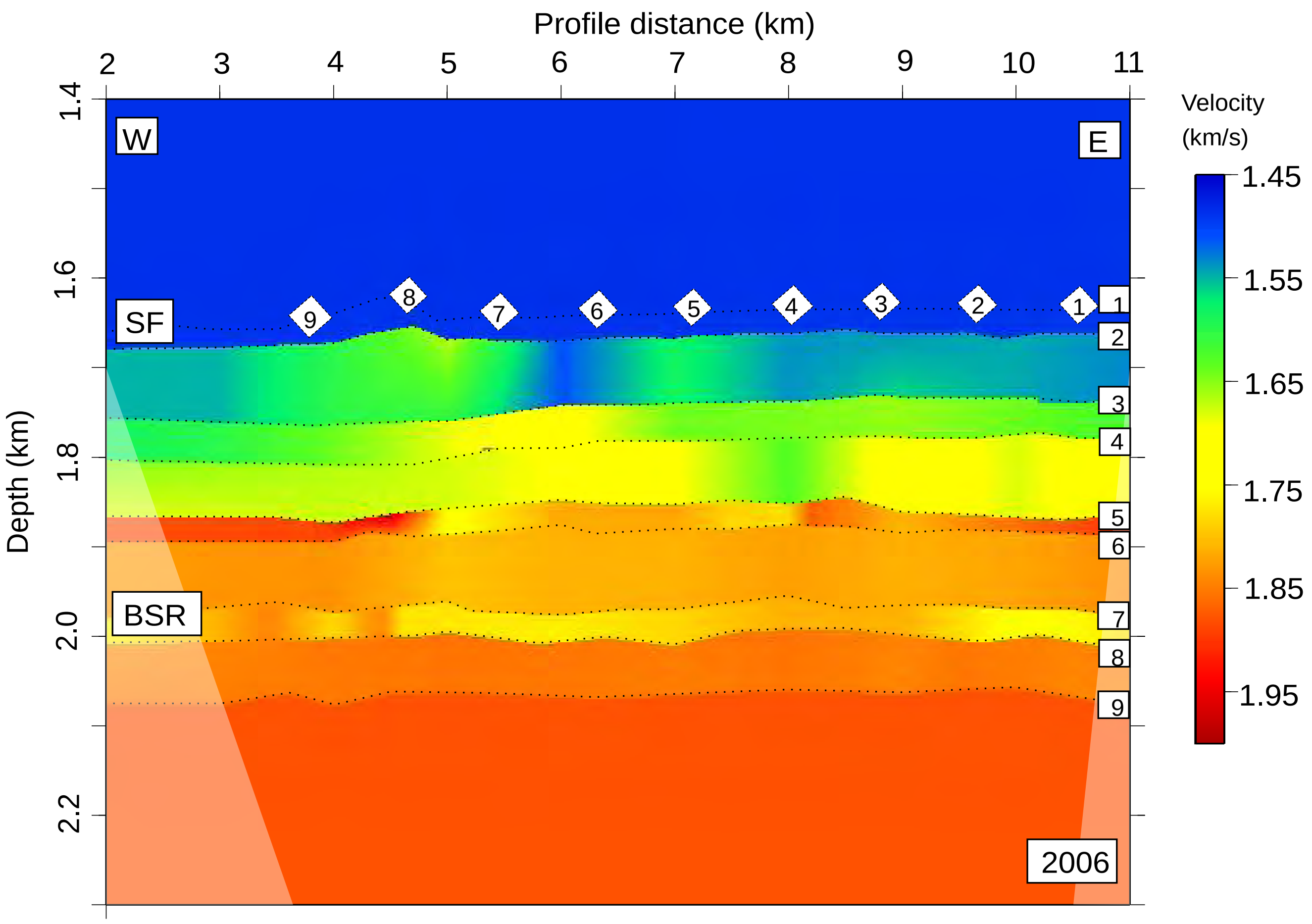

Fig. 3.10: Final 2-D velocity model obtained from travel-time inversion using reflections and refractions from nine OBSs and the 2-D SCS reflection data. West to east oriented profile, where the Mohican Channel is in the western part (seafloor topography probably corresponding to levees of channel). Diamonds represent the OBS positions on the seafloor.

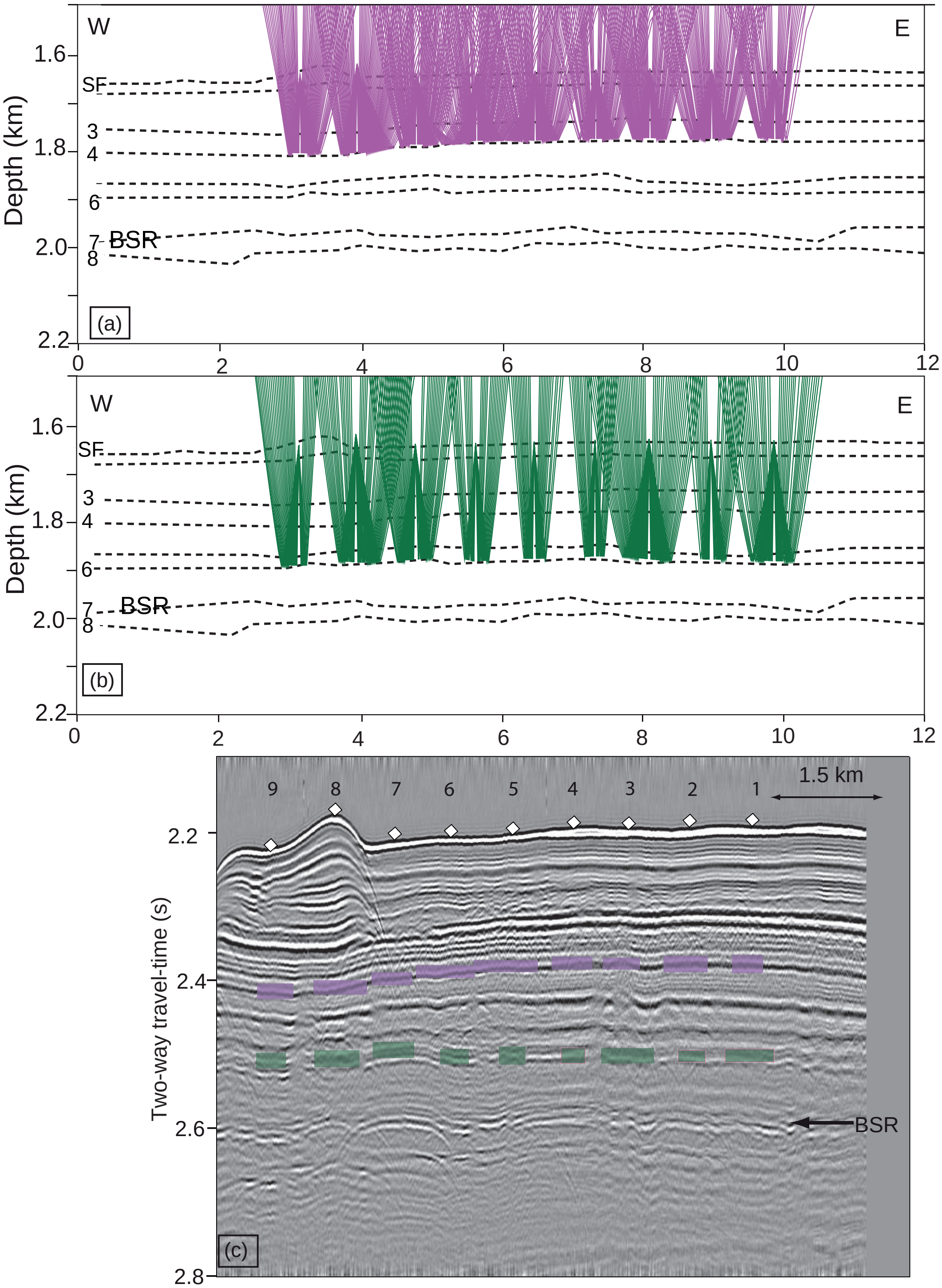

Fig. 3.11: Comparison of ray coverage of interfaces 4 (a) and 6 (b). The 2-D SCS reflection profile is shown with ray coverage (colored boxes) for each OBS for interfaces 4 and 6 (c).

3.2.4 Sensitivity analysis

The uncertainty of the modeled velocity values depends on the number of picked travel-time arrivals and the uncertainty assigned to those picks. The sensitivity method described in *Katzman et al.* (1994) was used to determine the stability of the modeled velocity parameters. Velocities are perturbed for a single layer of the final model and then they are held fixed while inverting for the corresponding depth values. The perturbations are made larger until the travel-time residual values increase significantly above the value of the starting model.

In a first modeling the velocities of the high velocity region above the BSR-like reflection in the 2-D SCS and 2-D MCS reflection data were modeled. Velocities of layer 5 and the top-velocity of layer 6 were perturbed with ± 3 % from starting values of 1.69 km/s and 1.82 km/s, respectively. The refracted and reflected arrivals of layer 5 were applied in the ray-tracing modeling. The misfit value for those perturbations ranged between 2.3 to 3 ms for the reflected arrivals and 4.5 ms for the refractions (Fig. 3.12 a).

The depth of interface 7 at ~330 mbsf was identified with the BGHSZ (BSR depth) in the 2-D SCS and 2-D MCS reflection data. The velocities of layer 7 were modeled with OBS and 2-D SCS reflection data picks and the allowed perturbations were ±3 % (60 m/s) relative to the optimal velocity of 1.82 km/s. The rms misfit value obtained with reflected arrivals from OBS and 2-D SCS data remained constant with 5.5 ms for the perturbation range (Fig. 3.12 b).

The sensitivity of the low-velocity region was tested with the velocities of layer 8 below the identified BSR-like reflection. Modeling was obtained with OBS data only (Fig. 3.13 a) and simultaneously with the 2-D SCS reflection data (Fig. 3.13 b). Results show that the inversion tends to favor lower velocities with increasing perturbation. The rms misfit value increases slightly from 2.1 ms to 2.3 ms over a perturbation range of up to -20 % of the optimal start velocity (1.74 km/s). Although the SCS could not strongly constrain the depth values of interface 8, the sensitivity analysis shows that by increasing the velocity with even less than 3 % increases the rms residual misfit values significantly. Thus higher velocities within that depth range can be excluded.

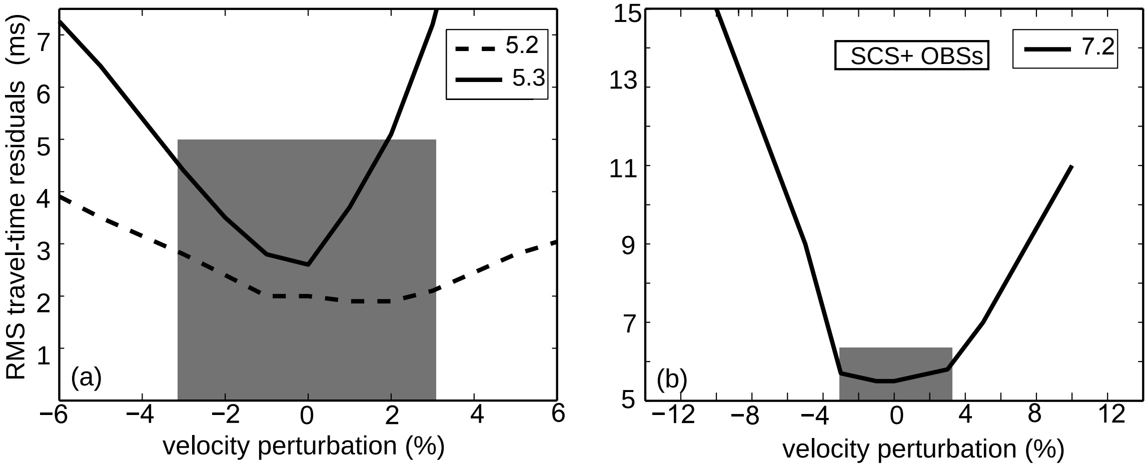

Fig. 3.12: (a) Sensitivity analysis (*Katzman et al.*, 1994) applied to reflections from interface 5 (5.2 - dashed line) and refractions from the top of layer 6 (5.3 - solid line) for all nine OBS stations. (b) Sensitivity analysis carried out on velocities of the high velocity layer 7 with OBS and 2-D SCS reflection data. An approximate estimate of the confidence range is a velocity perturbation of ± 3 % for both sensitivity analyses (shaded box).

3.2.5 Summary of 2006 data modeling

Travel-time inversion models were obtained using the algorithm of *Zelt and Smith* (1992) applied to data from nine OBS stations and a 2-D SCS reflection profile collected in 2006. Modeling refracted arrivals for a depth of 220 m below seafloor (bsf) is related to an increase in velocity of 140-190 m/s. This high velocity region was modeled above a reflection associated with the BGHSZ at 330 mbsf in 2-D SCS and 2-D MCS reflection data (*Cullen et al.*, 2008). However, the corresponding velocity contrast associated with BSRs could scarcely be modeled. The velocity drop below the BGHSZ was modeled with a decrease of only 50-80 m/s. The thicknesses of the two layers were modeled with 100 m for the high

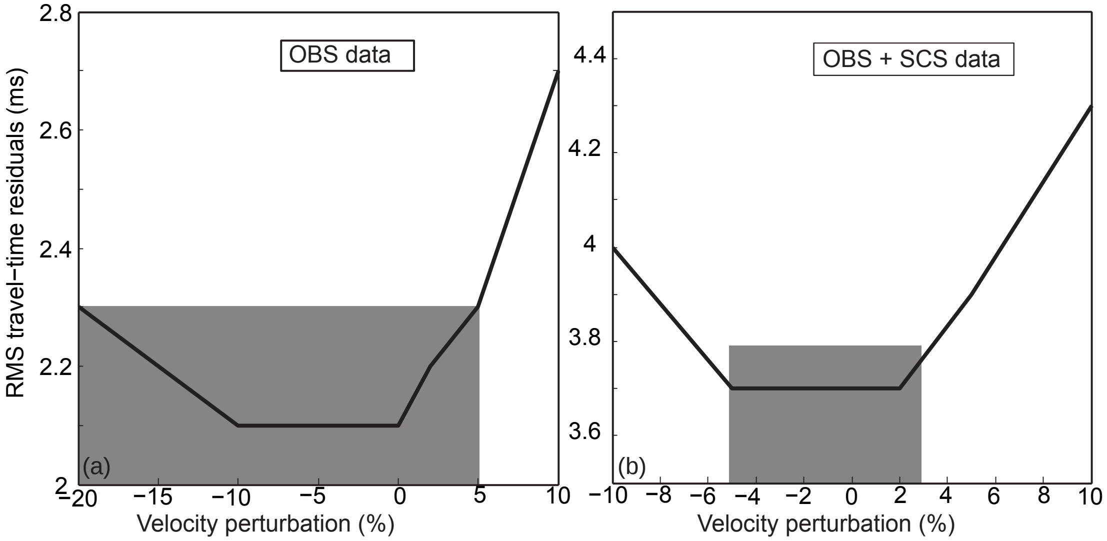

Fig. 3.13: Comparison of sensitivity analysis for layer 8 achieved for (a) OBS data and (b) combined with the SCS reflection arrivals. The rms misfit value increases slightly with decreasing velocity over a range of -20 % perturbation (shaded box). (b) Combined inversion of OBS and SCS data shows no significant change in rms misfit values for up to +3 % (~50 m/s). It allows lower values with up to 5 % (~80 m/s) velocity change from the starting value of 1.74 km/s (shaded box).

velocity region and 30 m for the low-velocity region. The BSR was not clearly identified in the OBS and 2-D SCS reflection data, because it lacks the inverted phase signal. The 2-D SCS reflection data (Fig. 2.7) show a strong amplitude reflection in the time-range of the BGHSZ. However, the reflection also does not follow the seafloor topography as is commonly observed with BSRs.

Modeling the sensitivity of the higher velocity zone above the BGHSZ shows that velocities can vary by ± 3 % (60 m/s). These results indicate even higher velocities than modeled (1.82 km/s) with the travel-time approach. However, sensitivity modeling of the lower velocity region below the BGHSZ shows that velocities may vary by up to ± 3 % (50 m/s) for the 2006 data. Sensitivity results indicate that velocities can be even lower than 100 m/s (5 %) than the modeled velocity of 1.74 km/s.

3.3 Travel-time inversion applied to the 2004 OBS and 2-D SCS reflection data

Travel-time inversion of the 2004 OBS data has previously been carried out by *Cullen et al.* (2008). They determined 1-D vertical velocity models for each OBS station independently. The 1-D velocity models for the nine OBSs of the 2004 survey provide meaningful information on the vertical velocity structure underneath each station.

Within this thesis study the 1-D vertical profiles were re-modeled and refined (Fig. 3.14). Wide-angle reflection and refraction travel-times from all nine OBS stations of the 2004 data, plus travel-times from the 2-D SCS reflection data, were modeled simultaneously to create a 2-D velocity model.

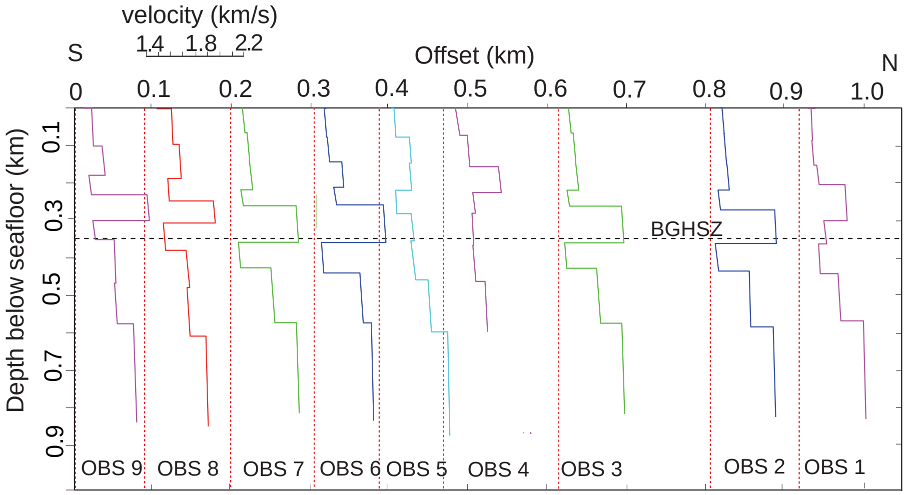

Fig. 3.14: The 1-D velocity-depth models for the nine OBSs (2004) obtained from *Cullen et al.* (2008) were re-modeled in this study. The red dashed line is the reference velocity mark (1.4 km/s) to calculate the velocity differences using the scale on top. Each profile is separated from its neighboring profiles with the spatial distance from the geographical locations. The black dashed line indicates the depth of the BGHSZ from the 2-D reflection data (Fig. 2.10). The velocity increase of 210 to 450 m/s at ~200 - 250 mbsf was modeled on all stations except OBSs 4 and 5, where a smaller velocity contrast occurs.

3.3.1 Data handling and selection of reflections and refractions for the travel-time modeling

While the spatial OBS separation for the 2006 survey averaged 900 m, the 2004 OBS instrument spacing was smaller with 100 m. Shots were also fired by distance with an average spacing of 20 m. Similar to the 2006 data the shot profile was 12 km in length and therefore both 2-D velocity models (2004 and 2006) are comparable. However, the velocity models may differ in resolution and accuracy.

Data preparation for travel-time inversion applied to the 2004 data was comparable to steps carried out on the 2006 data sets. The 2-D SCS reflection data were bandpass filtered (10-250 Hz) for a better identification of the seismic horizons (Fig. 2.10). However, the unfiltered OBS ensures no phase shifts due to filtering and was used to identify the reflected and refracted waveforms.

The hydrophone component data from the OBS instruments of both data sets (2004 and 2006) were compared with each other. Reflections were identified in the 2004 data set consistent with the horizons picked in the 2006 data (Fig. 3.15) and the equivalent reflections in the corresponding 2-D SCS reflection profile were also picked for travel-time modeling (Fig. 3.16). However, calculation of seafloor depths and comparing them with bathymetry values show that the seafloor and subsurface reflections on the 2-D SCS reflection data have a delay of 360 ms. Thus the SCS reflection profile was adjusted in time so that the reflections were comparable with those of the OBS data.

For the final travel-time modeling eight reflections were identified in the OBS and 2-D SCS data and modeled. Additionally, one refracted arrival was also identified on some of the OBSs (OBSs 6, 7, 8, and 9) with an apparent velocity of ~1.66 km/s.

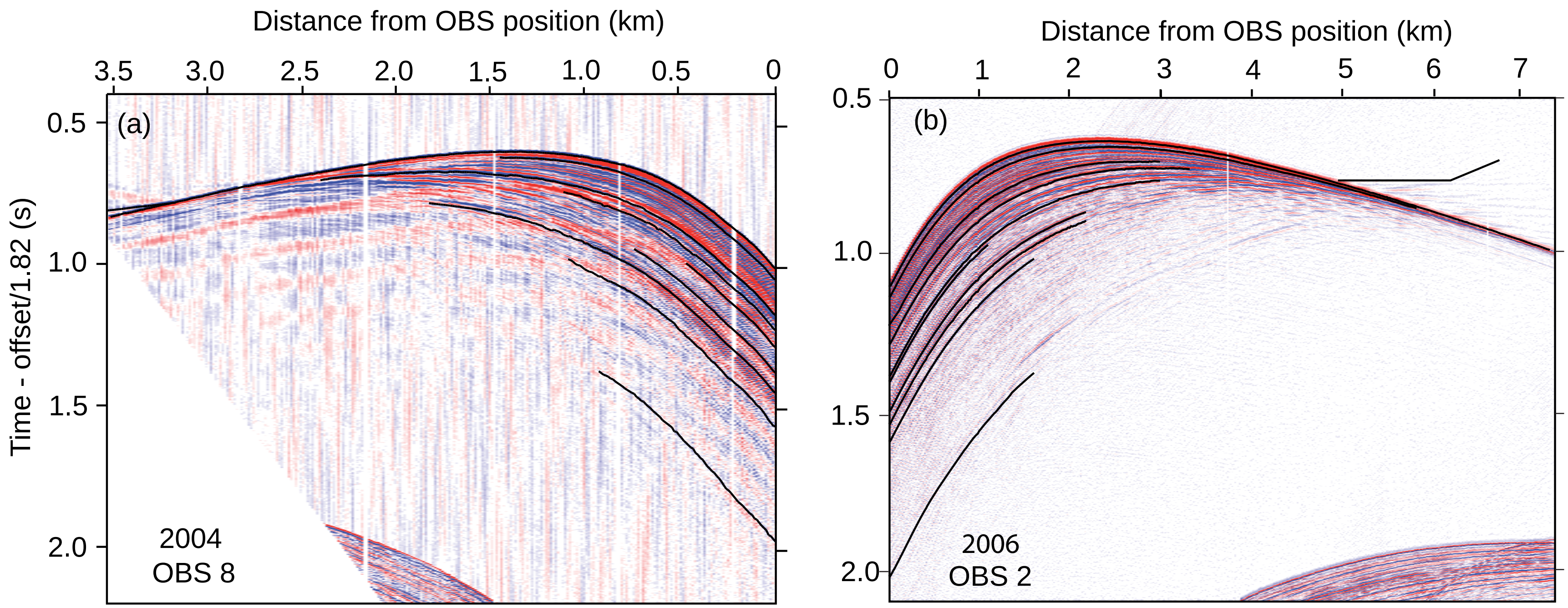

Fig. 3.15: Comparison of hydrophone components of (a) OBS 8 (2004; BP: 10-250 Hz) and (b) OBS 2 (2006; BP: 10-250 Hz) showing the identified reflections and refractions used for travel-time inversion. Both data sets show only one side of the instrument with a reduced velocity of 1.82 km/s.

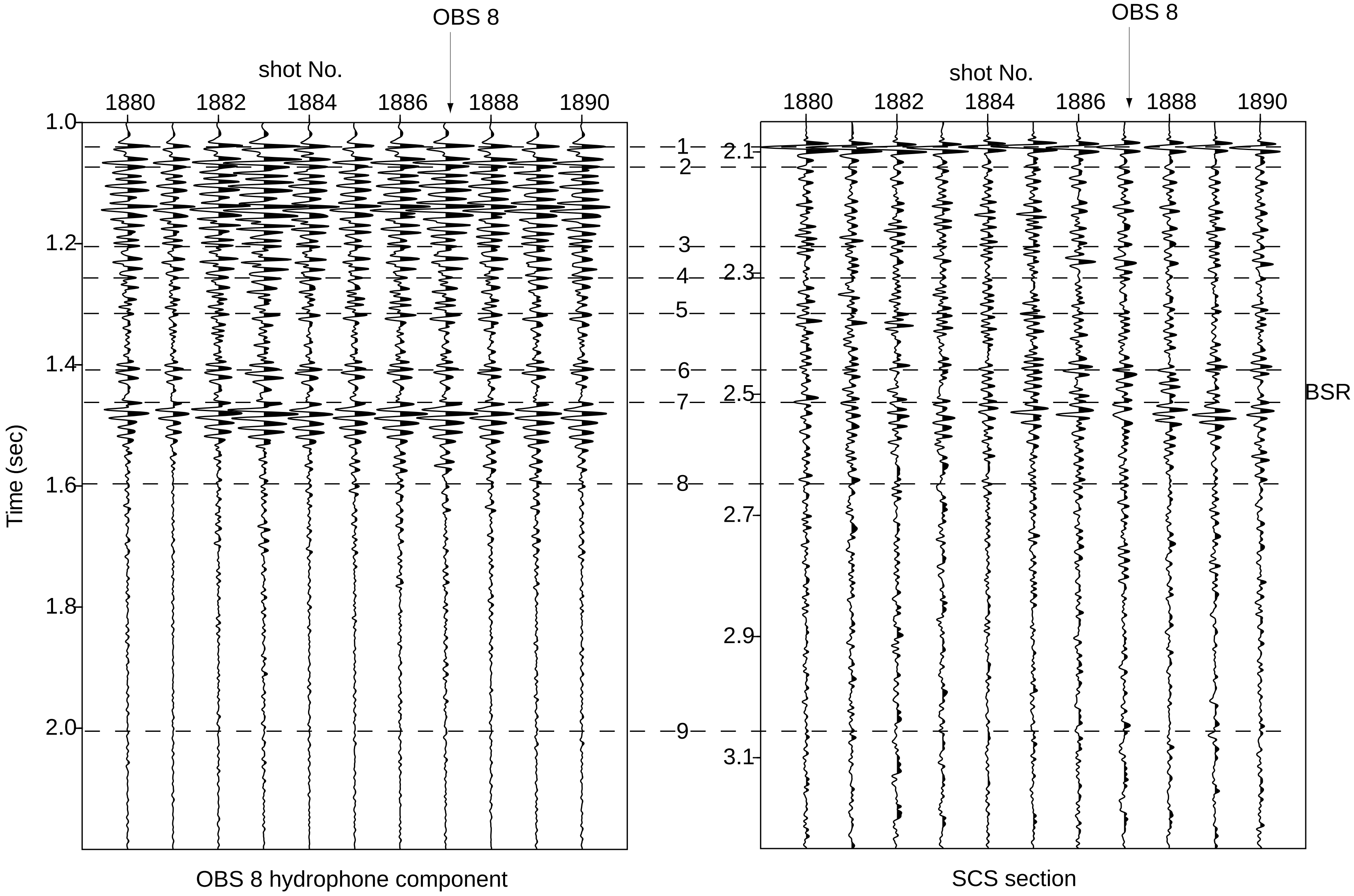

Fig. 3.16: Comparison of (a) the 2004 OBS 8 hydrophone data (BP: 10-250 Hz) and (b) the 2004 2-D SCS reflection data (BP: 10-250 Hz) near the OBS 8 location. The BSR-like reflection was not clearly assigned to reflection 6 or 7, because the inverted phase signal is not observed for neither of them.

3.3.2 Travel-time inversion results from the 2004 OBS and 2-D SCS reflection data

Seafloor reflection and direct arrival:

In a first step the vertical incidence seafloor reflections were modeled with the OBS direct arrivals. The rms misfit value of 2.96 ms is comparable to the misfit achieved while relocating the OBS and shot positions (3.2 ms) (Chapter 2.4). However, the depths obtained in the relocation approach differ by an average of 10 m from the depth-values extracted from the bathymetry (multibeam) data provided by David Mosher. Using the bathymetric depths for the travel-time modeling of the seafloor reflection reduced the rms misfit values to 1.9 ms and the χ^2 to a value less than 1. Hence, the bathymetric depth values for the OBS positions were used for the inverse modeling

Uncertainty values for arrival picks identified in the OBS data and 2-D SCS reflection data are averaged and listed in table 6.3 (Appendix). A comparison of misfit values obtained while modeling the OBS data alone and combined with the 2-D SCS reflection data is shown in the same table.

Layers 2 and 3:

The reflections of OBS and 2-D SCS data were compared (Fig. 3.16) and simultaneously modeled with the travel-time inversion approach. Travel-time pick uncertainties for reflections from interfaces 2 and 3 were assigned as 2 ms for the OBS data and 3 ms for the SCS data. The modeled velocities for layer 2 and 3 were averaging at 1.6 km/s and rms misfit values of 3.5 ms and 4.4 ms, respectively, were achieved. The modeled layer thicknesses were 30 m for layer 2 and 100 m for layer 3.

Reflected and refracted arrivals of layer 4:

The reflection 4 was identified on both OBS and 2-D SCS reflection data with pick uncertainty values of 3 ms and 4 ms, respectively. However, the final rms misfit value

(6.9 ms) for the combined inversion of OBS and 2-D SCS data travel-times from interface 4 was higher than the estimated pick uncertainties.

The OBS refracted arrivals with an apparent velocity of 1.66 km/s match the depth value modeled for interface 4. Those refracted arrivals could only be identified on the most western OBS instruments (6, 7, 8, and 9). The rms misfit value for the refracted arrivals is 3.8 ms; hence slightly higher than the estimated pick uncertainty (Fig. 3.17). The velocity increases from 1.62 km/s at interface 4 to 1.7 km/s at interface 5 with a thickness of ~50 m for layer 4.

Layers 5 to 8:

Simultaneous modeling of reflections from interface 5 for the OBS data and the 2-D SCS reflection data resulted in a layer thickness of 50 m. The inversion resulted in a model velocity of 1.68 km/s for layer 5 and the modeled rms misfit value was 5.7 ms.

The comparison of results from layer 5 with those of layer 6 shows a rms misfit decrease to 4.3 ms for a simultaneous modeling of OBS and SCS data. The smaller misfit value is the result of an improved visibility of the reflection 6 compared to the reflection 5 in both data sets; e.g. the number of picks doubled for layer 6. The velocities increase rapidly from 1.68 km/s at interface 5 to an average of 1.89 km/s at interface 6 within a modeled thickness of 100 m for layer 6. The base of this high velocity layer, at ~320 mbsf, corresponds to the depth of the BGHSZ and the BSR identified in the 2-D MCS reflection data from earlier studies (Chapter 1.4.5 - *Shimeld et al.* (2004); *Mosher* (2004))

The velocity decreases to 1.76 km/s below interface 6 and the layer thickness is about 90 m. The simultaneous inversion of SCS data and OBSs for velocities and depth values of layer 7 resulted in an rms misfit value of 5.3 ms. Ray tracing of reflections from the base of layers 6 and 7 is shown in figure 3.18.

Identifying reflections for interface 8 within the 2-D SCS reflection data was challenging due to low signal-to-noise ratios for the data, so the depth of layer 8 was difficult to

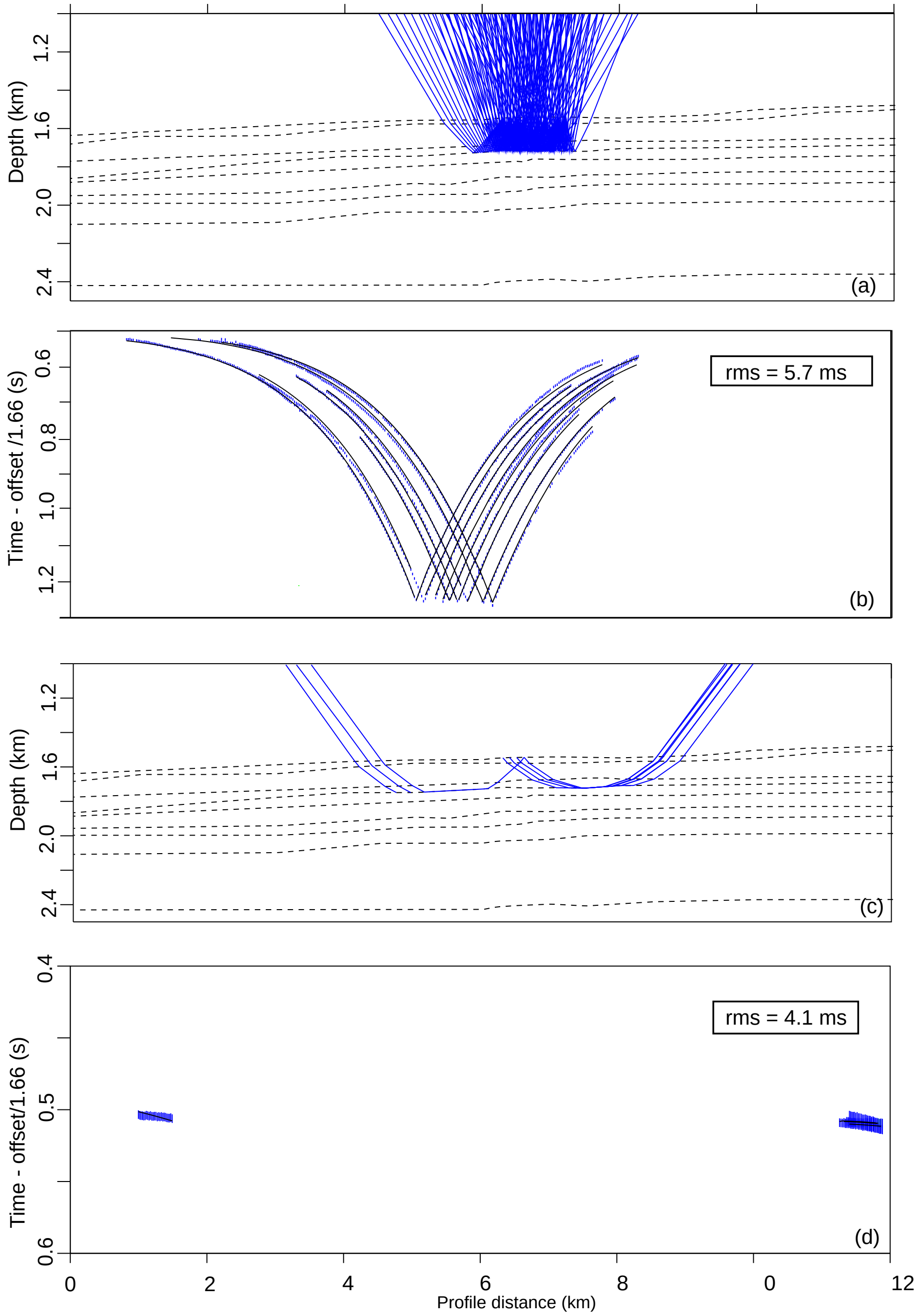

Fig. 3.17: Reflected rays (a) from the base of layer 4 for OBS data and corresponding observed travel-times (green bars) and modeled travel-times (black) (b). Rays corresponding to the refracted arrivals of OBSs 6,7,8, and 9 (c) and corresponding observed (green bars) and modeled travel-times (black) (d) in a linear-reduced time display with an apparent velocity of 1.66 km/s. Observed travel-times were assigned with an uncertainty value of 5 ms for a better visualization.

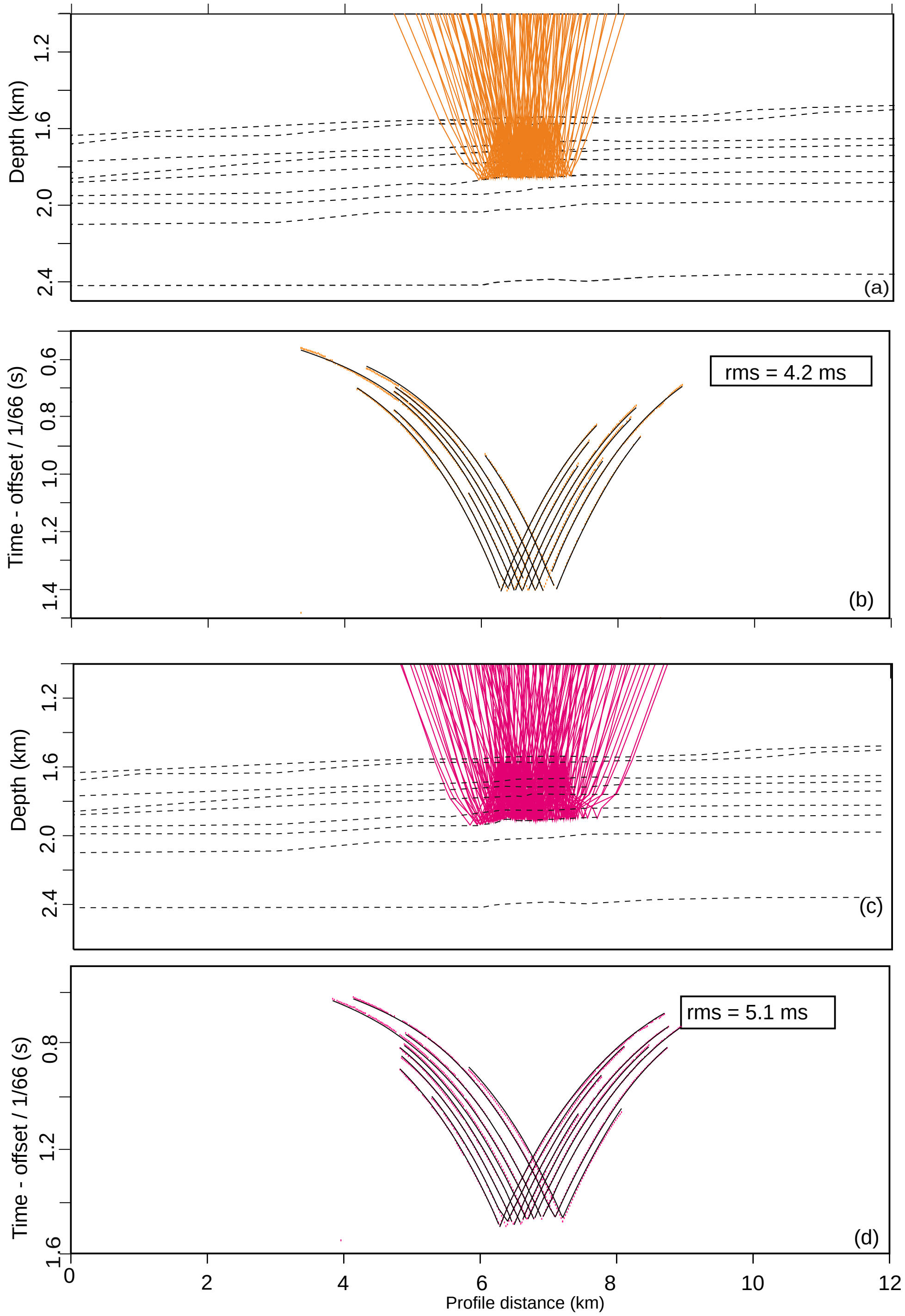

Fig. 3.18: Ray tracing for reflections from interface 6 for the OBS stations only (a) and corresponding modeled (black dots) and observed (orange bars) travel-times with an assigned uncertainty of 5 ms (for better visualization) (b). Rays (c) and corresponding travel-times (d) for interface 7 (modeled - black dots, observed - pink bars with 5 ms uncertainties)

constrain. Modeled rms misfit values are comparable to those of the shallower interfaces (4.7 ms). The modeled average layer thickness is approximately 100 m and the velocity increases to an average of 1.8 km/s. The velocities of layer 9 were modeled with 1.9 km/s, but the corresponding reflection could only be identified on some of the OBSs. The 2-D SCS reflection profile provided no information to constrain the depth of this layer.

The final velocity model is shown in Figure 3.19. Since the ray-coverage for modeling OBS data was achieved only between 4 and 8 km profile distance, despite a full profile length of 12 km, only this part of the model is enhanced in Figure 3.19.

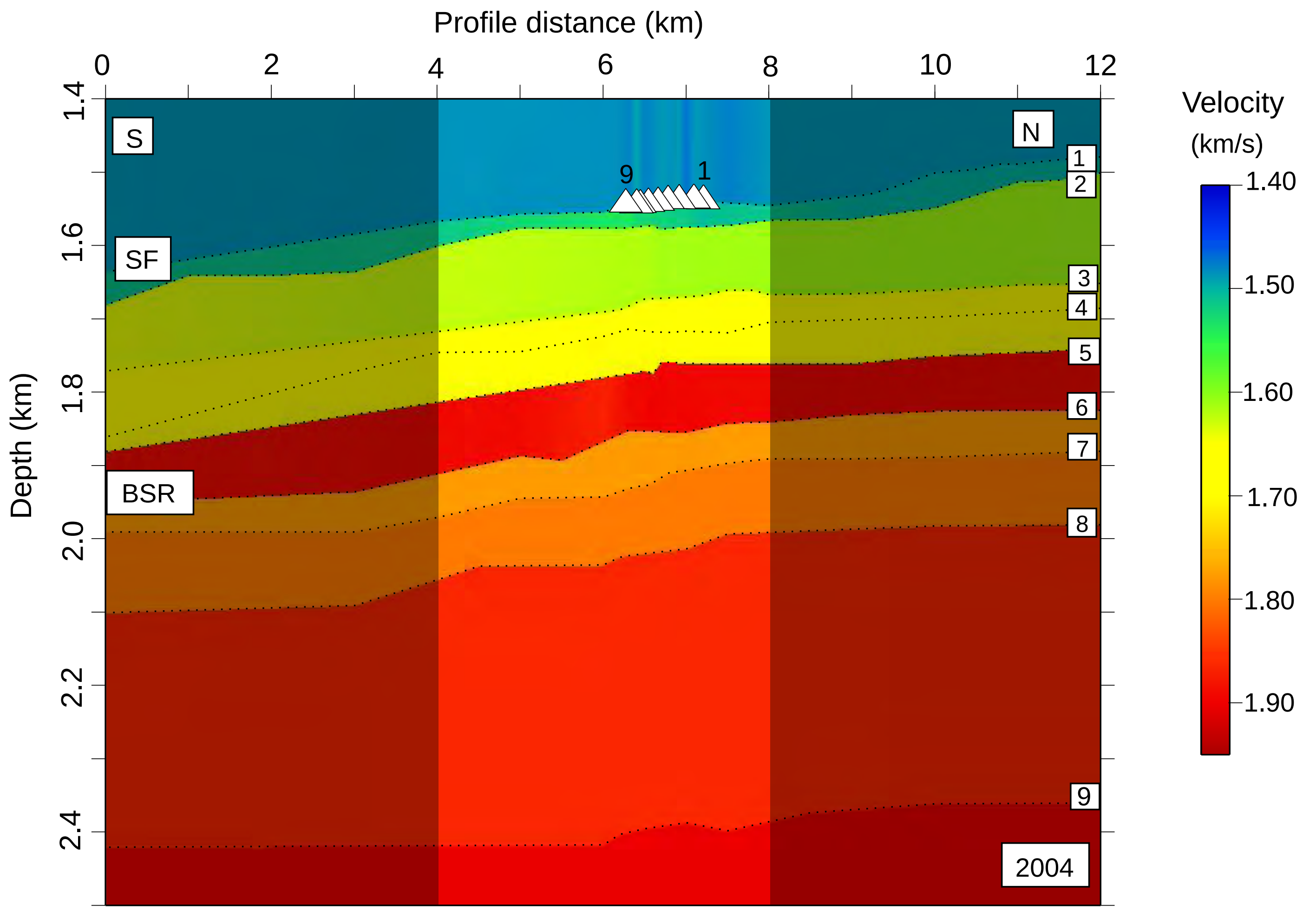

Fig. 3.19: Final 2-D velocity model for the 2004 OBS and 2-D SCS reflection data for all identified interfaces. The model is enhanced between 4 and 8 km profile length as the region of sufficient ray-coverage. OBS positions are indicated with a triangle at the seafloor depth and the labeled numbers indicate the interfaces of the model.

3.3.3 Sensitivity analysis

Similar to the 2006 OBS and SCS analyses, a sensitivity analysis was carried out on the velocities of the layers above and below the identified BSR-like reflection associated with the BGHSZ (layers 6 and 7) for the 2004 data (Fig. 3.20). The analysis was accomplished by perturbing the layer velocity and then inverting for the depth of the interface at the base of the layer.

For the higher velocity zone (layer 6) above the BSR-like reflection (Fig. 3.19), sensitivity results show that velocities can vary by ± 3-5 % (60 - 100 m/s) from the optimal velocity of 1.89 km/s. For the low-velocity layer below the BSR-like reflection (layer 7), the sensitivity results show that velocities can vary by ± 3 % (± 50 m/s) from the starting value of 1.76 km/s without significantly affecting the misfit value.

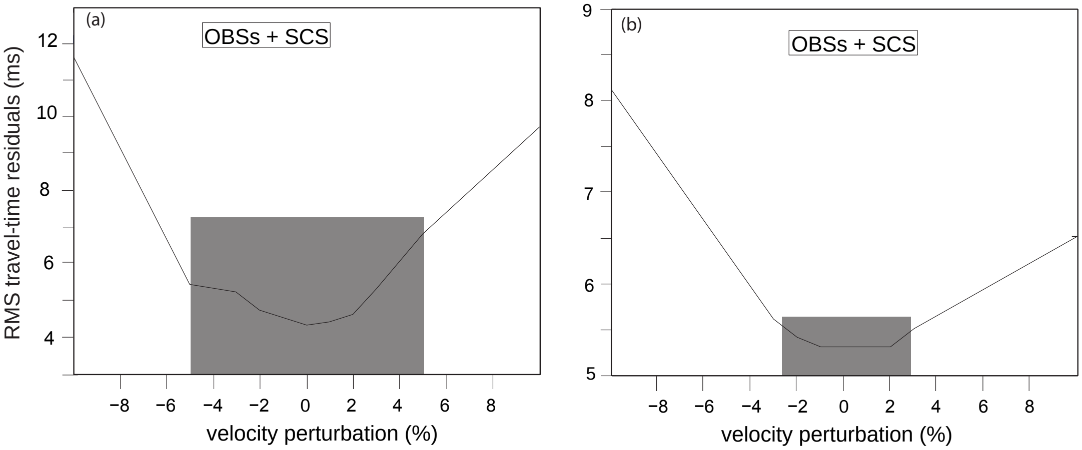

Fig. 3.20: Velocity perturbations were applied for layer (a) 6 and (b) 7, while inverting for the depth of the layer base. Shaded boxes indicate the limits within which the velocity could change without significantly changing the misfit value.

3.3.4 Summary of 2004 data modeling

The most prominent feature in the final 2-D velocity model of the 2004 data is a high-velocity layer with a thickness of ~110 m and an average velocity of 1.9 km/s. The base of this high-velocity layer, at 310 to 330 mbsf, corresponds to the reflection associated with the BGHSZ identified on the 2-D SCS reflections sections and the 2-D MSC reflection data (*Shimeld et al.*, 2004; *Mosher*, 2004). The velocity suddenly decreases by 130 m/s below the BSR-like reflection and the layer thickness of this low-velocity region was modeled with ~100 m.

The final 2-D velocity model of the 2004 data has a horizontal profile coverage of 4 km, because the OBS spacing of this survey with nine OBSs was 100 m. This is much smaller than the 9 km profile modeled with the wider spaced (~900 m) 2006 OBS array.

Comparing the final results of both data sets shows that the same significant reflections identified on both data can be modeled with similar velocity and depth values. However, similar to the 2006 OBS and 2-D SCS reflection data, the BSR was not observed with a clear reversed phase signal nor as a reflector following the seafloor topography. The depth of interface 6 is associated with the depth of the BGHSZ. Hence, the reflection is referred to as a BSR-like reflection.

3.4 Estimates of gas hydrate and free gas concentrations

A prominent feature in the final 2-D models for the 2004 and 2006 surveys is a high-velocity layer in which the velocity increases by 140 to 300 m/s. With a thickness of approximately 90 to 100 m, the top of the layer occurs at 220 mbsf, and the base at 310 - 330 mbsf. Beneath this layer, the velocity decreases by 130 m/s in the 2004 model, but only by 50-80 m/s in the 2006 model. The velocity decrease occurs at the interface identified with the depth of the BGHSZ from from 2-D reflection seismic data from previous studies. Thus, we interpret the high-velocity layer as a region of increased gas hydrate concentration. The low-velocity layer beneath the inferred hydrate zone is interpreted to correspond to a zone in which free gas is present.

3.4.1 Compare velocity model results with previous studies

To compare the final 2-D model results from the 2004 and 2006 data (Figs. 3.10 and 3.19) with the results from *LeBlanc et al.* (2007) and *Delescluse et al.* (2011), velocities for each interface were averaged with a constant spatial sampling of 100 m across the 2-D velocity profiles. Error estimates on the velocities obtained from the sensitivity analysis are shown with error bars for each layer (Figs. 3.21 and 3.22). The grey shaded area represents the confidence intervals for the velocities determined by the sensitivity analysis. The averaged 1-D velocity profiles (2004 and 2006) are comparable to results from two OBS stations (OBSs 1 and 2) from the 2002 data of *LeBlanc et al.* (2007), although there are some distinct differences.

The velocity model of OBS 2 (2002) (Fig. 3.21 - purple dashed line), which is closest (2 km to the south) to the 2004 OBS array, shows an increase in P-wave velocity of 70 m/s at 230 mbsf. This velocity increase is significantly lower than the one modeled with the 2004 data (300 m/s) (Fig. 3.21 - green line) for the high-velocity zone above the BSR. However, the 100 m thickness of this high-velocity zone is comparable to the thickness modeled with the 2004 data.

Below the BGHSZ, a velocity decrease was modeled with both data sets (2002 and 2004). However, the thickness and velocity values for this layer are significantly different in the two models. The P-wave velocity decreases to 1.73 km/s in the 2002 model and the thickness of this layer is about 260 m (*LeBlanc et al.*, 2007). The layer thickness modeled with the 2004 data is only approximately 100 m, and the velocity drop is larger (130 m/s) than for the 2002 data (75 m/s).

The velocities modeled for OBS 1 (2002) (Fig. 3.22, purple dashed line), which is closest to the 2006 OBS array (1 km north of OBSs 3 and 4), show similar results to OBS 2 (2002). The velocity increases by an average of 150 m/s at a depth of 230 mbsf, but drops only by 50 m/s at approximately 360 mbsf. This is comparable to the final model of the

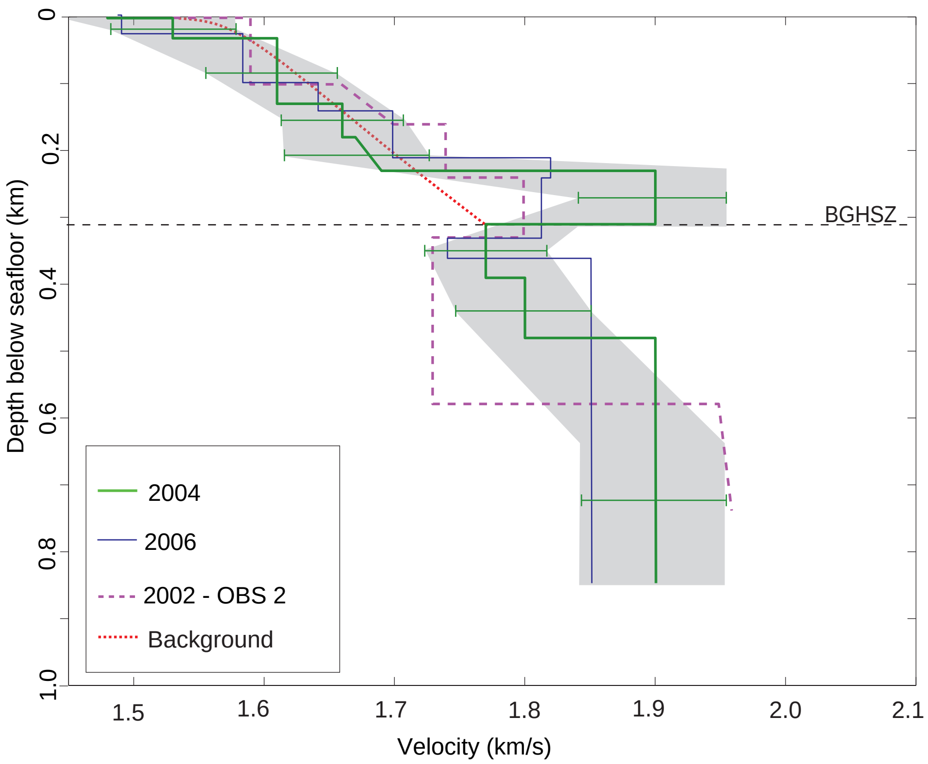

Fig. 3.21: Average 1-D velocity-depth profile (green line) of the 2004 2-D velocity model from the area of the main ray-coverage (4 to 8 km profile length) is compared to the 1-D vertical velocity-depth profile of OBS 2 (purple dashed line - 2002) and the final 1-D averaged velocity profile of the 2006 OBSs (blue line). The background velocity (red dashed line) was calculated using physical sediment parameters provided by *LeBlanc et al.* (2007) and the rock physics modeling of *Helgerud et al.* (1999). The grey shaded area represents the velocity perturbation range obtained with the sensitivity analysis.

.

2006 OBSs, where the velocity increases by 140 m/s and decreases by 50-80 m/s below the high-velocity layer (Fig. 3.22 - blue line). Hence, the thickness of the high velocity zone is approximately 120 m for the 2002 data and 2006 data. However, the thickness of the low-velocity zone is much greater for the 2002 OBS 1 (150 m) than for the 2006 data (30 m). The vertical velocity profile GXT-5300-B (Fig. 3.22 - orange line), which is located approximately in the middle of the 2006 OBS array, was obtained from *Delescluse et al.* (2011) and is generally consistent with the velocity profile of the 2006 OBS survey. The velocity increases by an average of 130 m/s at 230 mbsf, and drops by only 70 m/s at

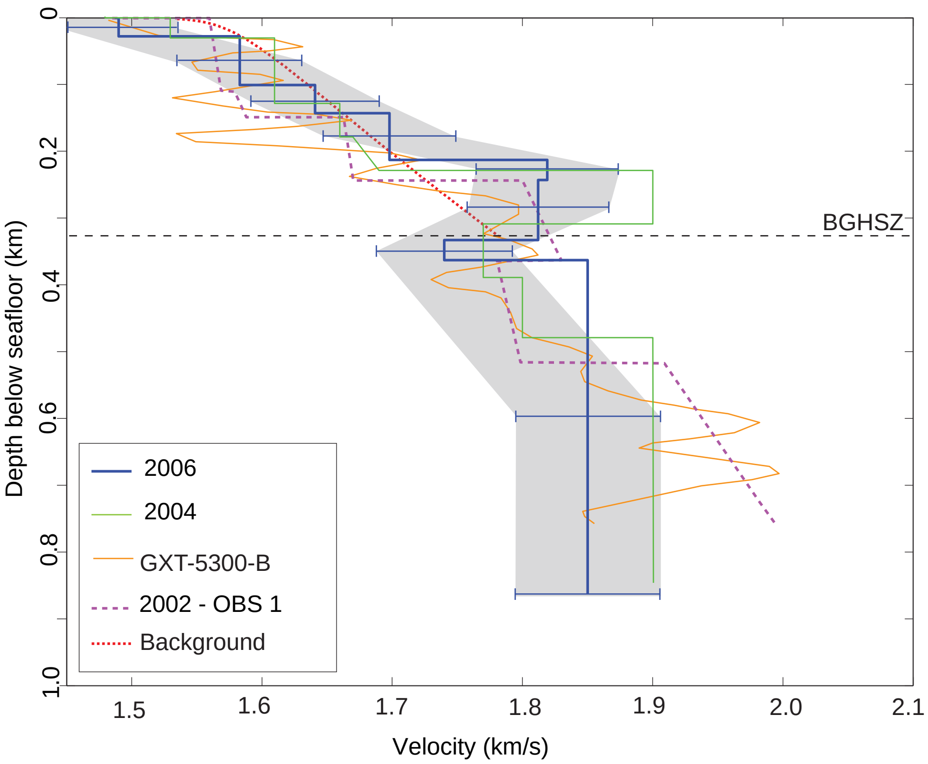

Fig. 3.22: Average 1-D velocity-depth model (blue line)from the 2006 data is compared to the 1-D vertical velocity-depth profile of OBS 1 (purple dashed line - 2002) and the final 1-D averaged velocity profile of the 2004 OBSs (green line). One vertical velocity-depth profile of *Delescluse et al.* (2011) obtained from a 2-D velocity model at a location that is closest to the middle section of the 2006 OBS array is shown as well (orange line). The grey shaded area represents the velocity perturbation range obtained with the sensitivity analysis.

a depth of 350 mbsf. Overall, the velocity contrasts for the 2002 models, for the inferred gas hydrate (high-velocity zone) and free gas layers (low-velocity zone), are closer to the results achieved with the 2006 data and smaller than the velocity contrasts from the 2004 data.

3.4.2 Estimated gas hydrate and free gas concentrations

Seismic velocities can provide estimates for gas hydrate and free gas concentrations. A number of methods based on porosity-depth relations have been used to convert velocities

Porosity at seafloor (%)	61
Compaction factor lambda (m)	1100
Composition of Quartz (%),Clay (%)	15,85

Tab. 3.1: Sediment properties modified from the values given in *LeBlanc et al.* (2007) to calculate physical properties such as velocities and densities.

to gas hydrate concentrations (e.g. *Lee et al.*, 1993; *Hyndman et al.*, 1993; *Jarrard et al.*, 1995). For the velocity models presented in this study, we used the effective medium theory (EMT) of *Helgerud et al.* (1999) to calculate the P-wave velocity predicted for a given gas hydrate concentration. The EMT is based on rock physics models (e.g. *Dvorkin et al.*, 1999).

The exponential decrease of the sediment porosity ϕ with depth is calculated incorporating the seafloor porosity ϕ_0 and the compaction factor λ (Eq. 3.8).

$$\phi(z) = \phi_0 * e^{(-z/\lambda)} \tag{3.8}$$

The compaction factor accounts for the non-elastic loss of pore space due to overburden pressure and subsequent volume change (e.g. *Sheriff*, 2002). The parameters shown in table 3.1 are taken from *LeBlanc et al.* (2007) and modified to fit the average velocity increase with depth for sediments containing no free gas or gas hydrate.

Several models exist with different distributions of gas hydrate in the sediment pore space. Gas hydrate can be either within the pore fluid or as part of the solid dry sediment frame. The latter assumption leads to a reduction in the sediment porosity and alteration of the sediment rigidity and hence its shear-wave velocity (*Helgerud et al.*, 1999). The gas is distributed either homogeneously throughout the fluid or within patches in the sediment pore space.

Gas Hydrate

Using the EMT for modeling gas hydrate concentrations, a reference velocity profile was calculated by assuming that no gas hydrate or free gas was present in the pore space (Fig. 3.23 and Fig. 3.24 - red dashed line). With the parameters given in table 3.1 three other profiles were calculated using the same sediment parameters but with 10 %, 15 %, and 20 % of gas hydrate concentrations in the pore space.

The calculated gas hydrate concentrations for the 2006 modeled velocities are 2 to 11 % of the pore space. These values are slightly larger than the 2 to 6 % concentrations of bulk gas hydrate estimated from the nearby OBS 1 in the study of *LeBlanc et al.* (2007). However, the modeled velocities for the 2004 data are higher, corresponding to a greater gas hydrate concentration of 8 to 18 % in the pore space of the sediment. This is the best estimate of the concentration range for the 2004 data, corresponding to a velocity uncertainty of ± 75 m/s; however, a larger range cannot be excluded since our sensitivity analysis provides only a rough velocity uncertainty of $\pm 50 - 100$ m/s.

Free Gas

As discussed by *LeBlanc et al.* (2007) concentrations of free gas in the pore space as small as 1 % can reduce the P-wave velocity by more than 5 %, or approximately 90 m/s. This is already known from earlier studies on laboratory data examples (e.g. *Lee*, 2004). Those free gas concentrations were calculated based on rock physics models presented by *Helgerud et al.* (1999) and *Dvorkin et al.* (1999). Similar velocity decreases of 50-80 m/s as modeled with the 2006 data set and 130 m/s modeled with 2004 data set correspond to concentrations of less than 1 % gas in the sediments at a depth of 310-330 mbsf. The modeled thickness for this low velocity layer beneath the BGHSZ is approximately 30 to 150 m. The modeled velocity for the region below the BGHSZ in the 2004 model, relative to the background velocity, is approximately the same as the uncertainty value obtained with the sensitivity analysis (see section 3.3.3). Hence, the layer below the BGHSZ can be modeled without free gas. However, the modeled velocity for the region below the BGHSZ in the 2006 model indicates lower velocities (≤ 100 m/s) than the background

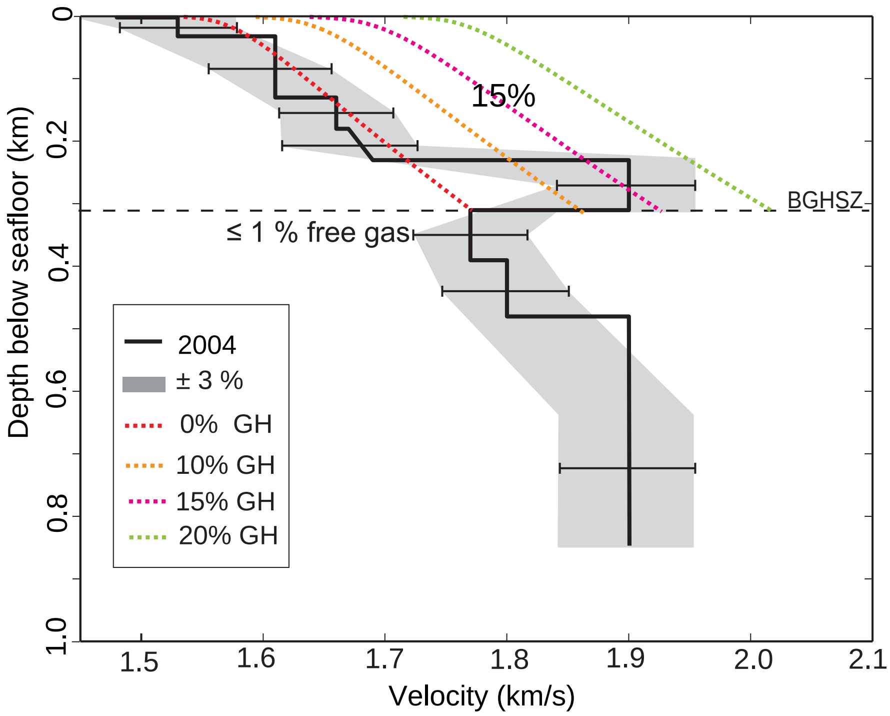

Fig. 3.23: Comparison of the 1-D velocity profiles (2004- black line) with the background velocity profile (red dashed line) calculated for no gas hydrate and free gas fillings using rock physics models (*Helgerud et al.*, 1999) and physical properties given by *LeBlanc et al.* (2007). Three other velocity profiles (10 % gas hydrate - orange dashed line; 15 % gas hydrate: purple dashed line; 20 % gas hydrate: green dashed line) were also calculated.

velocity. Thus, we conclude that a small quantity of free gas is present in the region below the BGHSZ.

3.5 Discussion

Our results suggest a systematic variation of gas hydrate concentrations in the study area. The OBS sites of this study are located near the eastern sidewall of the Mohican Channel (Fig. 1.3). The 2004 OBS array, oriented north to south, is parallel and very close to the channel wall, whereas the 2006 OBS array is oriented west to east, perpendicular to the channel wall and extending away from it. In the final 2-D velocity models, velocity values and calculated gas hydrate concentrations for the layer above the BGHSZ are signif-

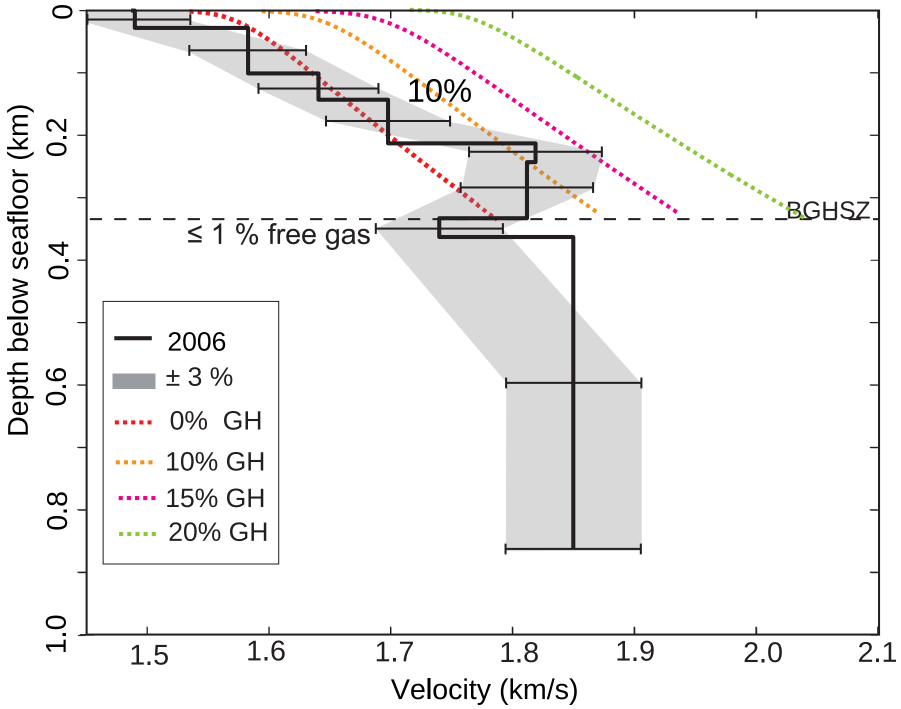

Fig. 3.24: Comparison of the 1-D velocity profiles (2006-black line) with the background velocity profile (red dashed line) calculated for no gas hydrate and free gas fillings using rock physics models (*Helgerud et al.*, 1999) and physical properties given by *LeBlanc et al.* (2007). Three other velocity profiles (10 % gas hydrate - orange dashed line; 15 % gas hydrate: purple dashed line; 20 % gas hydrate - green dashed line) were also calculated.

icantly higher for the 2004 data than for the 2006 data. That is, gas hydrate concentrations generally appear to decrease with distance from the Mohican Channel. This pattern is consistent with the 2 to 6 % gas hydrate concentrations derived for the 2002 data for OBS 1, located east of the channel (*LeBlanc et al.*, 2007). This is most likely related to the sediment composition that changes with distance to the channel. Recent studies (reviewed in e.g *Boswell and Collett*, 2006) have shown that gas hydrates are more often found in sands. Due to the sedimentation and glaciation history of the Scotian margin (see chapter 1.3) the sediments are fine-grained, glacially-derived, marine sediments with a high percentage of clay (*Mosher*, 2008). The coarser grained deposits (e.g. sands) were probably transported within the submarine channels (e.g. Mohican Channel) and deposited over the sidewalls (flanks) and at the foot of the channel. Thus the concentration of sand decreases away from the thalweg (center) of the channel. As other seismic studies have shown small-scale faults and vent structures can be observed within the depth range of the gas hydrate bearing sediments (*Cullen et al.*, 2008; *Mosher*, 2011). However, it is not yet verified that those are acting as migration routes for fluids and gases into the stability field.

A key feature of the gas hydrate distribution on the passive Scotian margin, based on the seismic velocity analyses, is that the hydrate is distributed in the 100 m thick region just above the BGHSZ, with no indications of gas hydrates occurring between the seafloor and the top of that layer (~220 mbsf). *Malinverno et al.* (2008) presented modeling results from the Cascadia margin to show that this could be produced, either by low sedimentation rates or by low rates of upward fluid flow. On the passive Scotian margin, the low fluid flux rates are likely the dominant factor in restricting gas hydrate to the layer above the BGHSZ. However, no fluid-flux measurements were undertaken to this date that can constrain this hypothesis.

Similar to the gas hydrate distribution is the occurrence of the observed BSR in the 2-D reflection seismic data sets. BSRs occur in patches distributed over the Scotian margin and are mainly located where channel structures appear (*Cullen et al.*, 2008; *Mosher*, 2011). Recent studies by (*Campbell et al.*, 2010; *Campbell*, 2011) and *Mosher* (2011) state that the recognized BSR at the Mohican channel site is within the large Shubenacadie sedimentary drift deposit that was transported during the late Miocene and Pliocene. The BSR appears in a depth range that can be correlated with the onset of the Quaternary (1.6 Ma ago). Recent studies (e.g. *Mosher*, 2011) show that the Pleistocene-to-recent Mohican Channel cuts through these deposits, exhibiting various episodes of cut-and-fill during this period.

The BSR is only recognizable in the 2-D seismic profile chosen arbitrarily from the 3-D seismic data cube (Fig. 2.12 in section 2). However, it quickly fades into the reflectivity of the seismic stratigraphy. Neither the 2-D SCS reflection data nor the OBS data show the BSR as a reflection with a reversed phase to the seafloor signal and a strong amplitude.

Studies by *Chapman et al.* (2002) and *Lee* (2007) show that BSRs can disappear with respect to the source frequency that is used. The BSR amplitude decreases with increasing frequency. *Lee* (2007) conclude that the amplitude reduction of the BSR at the Blake Ridge with increasing frequency content is due to seismic attenuation. However, P- wave velocity dispersion of partially gas saturated sediments alone can decrease the amplitude of the BSR approximately by a factor of three (*Lee*, 2007).

The velocity contrast modeled within this study is small as are the calculated free gas concentrations. The layer below the BGHSZ can be modeled as a gas-free zone or a region containing a small amount of free gas. If significant amounts of free gas were present in the sediments, the low velocity would be less than the water velocity. Our velocity results indicate values that are similar to the background velocity values (1.7 - 1.8 km/s).

However, the thickness of the free gas zone (up to 150 m) modeled within this study is consistent with *Xu and Ruppel* (1999) and *Haacke et al.* (2008), who argue that a thick free gas zone is associated with passive margins with low rates of methane flux ($\leq$ few tenths mm/yr, (*Haacke et al.*, 2007)) and slower seafloor uplift. Hence, low concentrations of free gas in the sediments below the BGHSZ are expected. The modeled velocity for the region below the BGHSZ in the 2006 model can be 100 m/s less than the background velocity. Thus, we can infer small concentrations ($\leq 1\%$) of free gas in the sediments pore space. However, the data of this study and the applied methods limit the resolution of those small velocity contrast associated with the free gas concentrations.

The 1-D vertical velocity profiles obtained by *Delescluse et al.* (2011) show smaller contrasts between the two velocity zones at the depth of the BGHSZ with increasing distance from the Mohican Channel. In comparison to the velocity profile GXT-5300-B (Fig. 3.22) another vertical velocity profile was modeled by *Delescluse et al.* (2011) that is located several kilometers to the west of the 2006 OBS array, at the edge of the Mohican Channel. The results of this model show a velocity decrease of 200 m/s below the BSR depth. The lower velocity is most likely a result of a higher gas concentrations within the sediments that are closer to the Mohican Channel.

4. WAVEFORM TOMOGRAPHY

This thesis chapter introduces waveform inversion methods, particularly the frequency-domain waveform inversion developed by *Pratt* (1999). The application of this inversion approach to synthetic OBS data is shown in the first part of this chapter. In the second part of this chapter the waveform inversion technique is applied to the 2006 OBS data that was used in this thesis.

Travel-time inverse methods are commonly used for both MCS and OBS data. The benefit of those techniques compared to standard migration methods and waveform inversion approaches is their time efficiency and low computational cost. Two methods that are commonly applied were developed by Colin Zelt (RayInvr, FAST; *Zelt and Smith*, 1992; *Zelt and Barton*, 1998). The RayInvr inversion algorithm was applied to the 2004 and 2006 OBS data in chapter 3.

Travel-time inverse methods are based on the asymptotic ray theory assumption (Appendix 6.3.1, e.g. *Cerveny*, 2001; *Nolet*, 1987). This assumption is necessary to derive the ray equations from the waveform equation and implies very large frequencies. Lower frequencies that are crucial for the background velocity structure are omitted. Hence, this restrains the ability of travel-time inverse methods to recover low-velocity regions associated with free gas in natural marine gas hydrate environments. In the high-frequency ray-tracing approach, no turning rays can curve within the low-velocity zone, and rays can only turn upward again after velocities become larger than at the top of the low velocity zone. Thus, the thickness of the low-velocity zone is often difficult to model with ray-tracing methods. Waveform inversion approaches use the whole frequency spectrum of the source and access more information contained in the seismic waveform.

Several studies based on synthetic modeling comparing both travel-time tomography and waveform tomography (*Pratt et al.*, 1996; *Sirgue and Pratt*, 2004; *Brenders and Pratt*, 2007a), respectively, show that the velocity structure obtained by waveform inverse modeling has a higher vertical resolution than the velocity models achieved with travel-time tomography only. However, travel-time inverse methods are often applied to generate the starting model for the waveform inversion approach.

The lateral resolution attained in waveform inversion is generally in the order of the wavelength of the propagated wavefield (*Sirgue*, 2003; *Takam-Takougang*, 2011). In contrast the lateral resolution for travel-time inversion is limited to the first Fresnel-zone (e.g. *Williamson*, 1991; *Williamson and Worthington*, 1993).

Several waveform inversion algorithms have been developed over the last 20 years, both, in time domain (TD, e.g. *Tarantola*, 1984; *Mora*, 1987; *Shipp and Singh*, 2002) and in the frequency domain (FD, e.g. *Shin*, 1988; *Pratt and Worthington*, 1990; *Bunks et al.*, 1995). Both methods are analytically equivalent if all frequencies are inverted simultaneously (*Pratt*, 1999; *Sirgue and Pratt*, 2004). However, frequency-domain waveform inversion is more computationally efficient compared to the cost-intensive time-domain methods, because of the ability to use a limited number of frequencies that provide the same unaliased image as the time-domain approach that uses all frequencies of the source spectrum (*Pratt and Worthington*, 1988; *Sirgue and Pratt*, 2004). However, the computational cost of frequency-domain inversion is proportional to the number of frequencies that are used (*Sirgue and Pratt*, 2004).

Highly heterogeneous media can be modeled more efficiently with frequency-domain approaches and attenuation and dispersion effects can also be readily included into the modeling.

Time-domain waveform inversion has the advantage of using a wide range of frequency components, and thus the signal-to-noise ratios increase with the addition of more frequencies. The advantage of time-windowing the data to isolate late arrivals and P-S converted arrivals is only feasible in the TD approach (e.g., *Virieux and Operto*, 2009). However, the frequency selection of only a few frequencies is only feasible in the FD approach (*Pratt*, 1999; *Sirgue and Pratt*, 2004). Frequency-domain inversion approaches typically proceed sequentially from the lowest available frequencies in the data to higher frequencies using a single or a group of a few frequencies at each step (*Sirgue and Pratt*, 2004).

The waveform inversion approach applied in this thesis is implemented in the frequency domain and based on the algorithm developed by *Pratt* (1999). Thus the next section focuses on FD waveform approaches only. Several studies have been carried out using synthetic and real data sets to investigate deep crustal structures onshore using 2-D MCS reflection data sets (e.g. *Brenders and Pratt*, 2007a; *Bleibinhaus et al.*, 2007, 2009; *Ravaut et al.*, 2004) and offshore using wide-angle reflection and refraction data (e.g. *Operto et al.*, 2006; *Takam-Takougang and Calvert*, 2011; *Kamei et al.*, 2012). However, only two studies (*Delescluse et al.*, 2011; *Jaiswal et al.*, 2012) applied to 2-D MCS reflection data to investigate the shallow (<500 m) subseafloor structure in a marine natural gas hydrate environment have been conducted up to this date. Both studies are restricted due to the fact that the lowest available frequency from the source spectrum was 8 Hz. However, the study by *Jaiswal et al.* (2012) shows that in this waveform approach the model updates with these "high" starting frequencies improve the shallow subseafloor velocity structures significantly. Additionally to the "high" starting frequency of 8 Hz, the study by *Delescluse et al.* (2011) has limited refractions that were only observed at large offsets over a small offset range (~ 1 km) that restrain the inversion.

This thesis chapter shows the first application of synthetic and real OBS data to investigate shallow marine gas hydrate and free gas occurrences. In comparison to previous OBS studies using waveform inverse methods (e.g. *Operto et al.*, 2006; *Kamei et al.*, 2012), where large receiver spacing were used (1-10 km), this study shows for the first time an application of waveform inversion to examine small-scale features only a few hundred meters beneath the seafloor using high-resolution OBS arrays with receiver spacings of 100 m to 1 km.

Only a few previous studies (*Bleibinhaus et al.*, 2009; *Takam-Takougang*, 2011; *Kamei et al.*, 2012; *Jaiswal et al.*, 2012) have dealt with resolution and sensitivity tests applied to the FD waveform approach. The study by *Kamei et al.* (2012) shows an application of OBS data to deep crustal and mantle structures in the Nankai subduction zone. The checkerboard velocity perturbation tests resolve structures as small as 350 m, but the focus is in the deeper section of the crust (5 to 10 km depth). Shallow subseafloor structures (< 1 km) are resolved with 200 and 400 m checkerboard patterns in the study by *Takam-Takougang* (2011), but applied to MCS reflection data. The study by *Jaiswal et al.* (2012) deals with shallow subseafloor gas hydrates and resolution limits of ~30 m within the uppermost 400 m below the seafloor. However, this study is also applying the FD waveform approach to surface-towed MCS reflection data.

This thesis shows a resolution test of shallow (< 500 m) subseafloor structures applied to OBS data for the first time. The low-velocity region is recovered in corrugation patterns of 5 % velocity change in a variety of cell-sizes (100 m to 1 km) applied to a 1-km-spaced OBS array. The results of the resolution tests obtained in this study are guidelines for future studies that are not available from the current field data.

The results from chapter 3 have shown that the low-velocity region below the base of the GHSZ was difficult to constrain with travel-time inversion on both data sets (2004 and 2006). Seismic arrivals from deeper regions cannot be observed and modeled with certainty. Within this thesis chapter the region below the base of the GHSZ is explored with the waveform inversion algorithm of *Pratt* (1999) applied to synthetic OBS data. The modeling shows that an appropriate shot-receiver geometry provides the large offsets required for waves traveling through the deeper part of the model to recover the low-velocity region. The modeling of synthetic OBS data in this thesis chapter investigates limits on lateral resolution that have not been addressed in any previous study. These results are significant for future marine OBS surveys that examine small scale geological structures. This chapter contributes to the further understanding and investigation of gas hydrate and free gas occurrences in continental margin environments. In the last part of this chapter, the inversion is applied to real OBS data collected in 2006, with a starting model based on travel-time inversion. These results show the limitations of waveform inverse modeling using data with a "high" starting frequency (8 Hz) and a suboptimal signal strength.

4.1 Theoretical background for waveform tomography

In this section the fundamentals of waveform inverse theory are reviewed. This theory is based mainly on the (full-) waveform forward and inverse modeling approach developed by *Pratt* (1999).

4.1.1 The forward problem

The acoustic wave equation describes the recorded pressure field $u(\mathbf{x}, \omega)$ at a spatial location **x** arising from a disturbance at the source location (Eq. 4.1):

$$\nabla^2 u(\mathbf{x}, \omega) + \frac{\omega^2}{c^2(\mathbf{x})} u(\mathbf{x}, \omega) = -f(\mathbf{x}, \omega), \tag{4.1}$$

The term $f(\mathbf{x}, \omega)$ describes the distribution of the source energy in the model with an angular frequency (ω).

The acoustic wave equation is strictly valid only in fluids and gaseous media, but it is frequently applied in seismic waveform inversion. The acoustic isotropic wave approximation is applied in the FD waveform inversion shown in this study, which considers only the P-wave velocity as a model parameter (*Pratt*, 1999; *Bleibinhaus et al.*, 2007; *Brenders and Pratt*, 2007b). Hence, amplitude errors introduced by the acoustic modeling can be corrected for by applying careful preconditioning of the seismic data (reviewed in *Virieux and Operto*, 2009). The numerical solution is computationally inexpensive compared to the numerical solution of the elastic wave equation, because the dominant parameter is the P-wave velocity (e.g. *Pratt et al.*, 1996; *Brenders and Pratt*, 2007a; *Bleibinhaus*, 2011). A number of studies applied the acoustic waveform inversion successfully to elastic data (*Brenders and Pratt*, 2007b; *Delescluse et al.*, 2011; *Jaiswal et al.*, 2012; *Kamei et al.*, 2012).

Attenuation and dispersion can be easily added into the modeling by using the complex valued velocity (*Pratt*, 1999),

$$c = c_{Re} + i\, c_{Im} \tag{4.2}$$

$$c_{Im} = -c_{Re}/2Q, \tag{4.3}$$

where c_{Re} is the real velocity part and c_{Im}, the imaginary part of the velocity, contains the Quality factor (Q).

In a discrete form on a 2-D grid the numerical format of equation (4.1) can be stated as

$$\mathbf{S}(\mathbf{m},\omega)\,\mathbf{u}(\mathbf{m},\omega) \;=\; \mathbf{f}(\omega), \tag{4.4}$$

where **S** is the complex-valued impedance matrix, which depends explicitly on the 2-D acoustic model parameter **m** containing discretized velocity and density information of the subsurface materials (*Pratt*, 1999; *Brenders and Pratt*, 2007a). The pressure wavefield **u** and the source term **f** are defined in two dimensions (Nx, Nz) on the rectangular grid for each frequency. The pressure field **u**(**m**,ω) can be solved by seeking the solution for these linear equations.

4.1.2 The inverse problem

The non-linearity of the waveform tomography problem is due to the modeling parameter $\mathbf{m}(\mathbf{x}) = 1/c^2(\mathbf{x})$ in equation (4.4), where c(**x**) is the locally varying velocity field.

Synthetic seismic data **u** (**m**, ω) can be generated through forward modeling for a given source-receiver configuration, and for a given set of model parameters (*Brenders and Pratt*, 2007a). These modeled data are compared to the "real" (observed) seismic data. The main requirement for a good starting model for the inversion is that the first-arrival waveforms match within half a cycle of the dominant frequency (*Pratt*, 1999).

The data residuals δd, the errors between the modeled (**u**) and the observed data (**d**) for a single frequency component ω of a given source-receiver (**x, s**) pair, are defined as

$$\delta d = \mathbf{u}(\mathbf{m}) - \mathbf{d}(\mathbf{m}). \tag{4.5}$$

The objective of the waveform inversion is to find the model parameter **m** such that the data residuals δd are minima. This is achieved with minimizing the misfit defined by the squared sum of the data residuals:

$$\begin{aligned} E\left(\mathbf{m}\right) &= \frac{1}{2}\delta d^T \delta d && (4.6) \\ &= \frac{1}{2}\sum_{i=1}^{n} \delta d_i * \delta d_i && (4.7) \end{aligned}$$

where E (**m**) is the L_2-norm misfit-function and δd^T is the conjugate transpose of the residual.

For the frequency-domain waveform inversion approach used in this study the misfit is minimized by applying the negative gradient $G_m = -\nabla_m E$ with respect to the model parameters **m** (e.g. *Sirgue*, 2003).

$$\nabla_m E = \begin{pmatrix} \delta E/\delta m_1 \\ \delta E/\delta m_2 \\ \vdots \\ \delta E/\delta m_m \end{pmatrix} = \begin{pmatrix} \frac{\delta u_1}{\delta m_1} & \frac{\delta u_1}{\delta m_2} & \dots & \frac{\delta u_1}{\delta m_m} \\ \frac{\delta u_2}{\delta m_1} & \frac{\delta u_2}{\delta m_2} & \dots & \frac{\delta u_2}{\delta m_m} \\ \vdots & \vdots & \vdots & \vdots \\ \frac{\delta u_n}{\delta m_1} & \frac{\delta u_n}{\delta m_2} & \dots & \frac{\delta u_n}{\delta m_m} \end{pmatrix}^T \begin{pmatrix} \delta d_1 \\ \delta d_2 \\ \vdots \\ \delta d_n \end{pmatrix} = J^T \delta d. \qquad (4.8)$$

Each column of the sensitivity matrix $\mathbf{J}$ is a partial derivative wavefield (*Pratt*, 2008), representing the change in the wavefield **u** due to infinitesimal perturbation of a single parameter. Each *jth* element of the gradient vector contains the partial derivative wavefield $\delta\mathbf{u}/\delta m_j$ sampled at each receiver point and conjugated, multiplied by the data residuals, and summed over all receivers (*Pratt*, 2008).

The partial derivative wavefields are not calculated by perturbation and new modeling; they are rather calculated by the method known as *virtual source* (*Pratt*, 2008).

The *virtual source* is generated while differentiating equation (4.4) with respect to the *ith* model parameter, m_i:

$$\mathbf{S}\frac{\delta \mathbf{u}}{\delta m_i} + \frac{\delta \mathbf{S}}{\delta m_i}\mathbf{u} = 0. \qquad (4.9)$$

This results in a new forward model with

$$\mathbf{f}^{(i)} = -\frac{\delta \mathbf{S}}{\delta m_i}\mathbf{u}, \qquad (4.10)$$

as the *ith* virtual source. The virtual source results from the interaction of the original wavefield **u** with the changes due to the perturbation in the model parameter m_i (*Pratt*, 1999).

For every iteration *n*, the gradient is computed in two steps (*Pratt*, 2008):

1. The calculation of the backpropagated wavefield as solution to a forward modeling run where the source term is replaced by the data residuals (*Pratt*, 2008). Hence, the data residuals propagate backwards as a wave originating at the scattering locations.
2. The backpropagated wavefield is multiplied by the *virtual sources* at each grid point.

The gradient operation consists of forward propagation, backpropagation of the residuals, and a multiplication of the two fields. The model is updated in the next iteration *n+1* with a scalar step-length α that defines the direction of the model update vector. This steplength must be repeatedly calculated (*Brenders and Pratt*, 2007a):

$$m^{(k+1)} = m^{(k)} + \alpha^{(k)} G_m^k, \tag{4.11}$$

where $k = 1, ..., n$ are the model perturbations (updates).

However, the calculation of the step length α requires at least one forward modeling step. Hence, a minimum of at least three forward problems need to be solved for each iteration of the non-linear waveform inversion (*Brenders and Pratt*, 2007a).

4.1.3 Survey geometries

The 2-D grid spacing is chosen so to have a minimum of four grid points per smallest wavelength λ_{min} for a given minimum velocity c_{min} and maximum frequency f_{max} to achieve 95 $\%$ accuracy (*Jo et al.*, 1996; *Brenders and Pratt*, 2007a):

$$\Delta = \frac{\lambda_{min}}{4} \tag{4.12}$$

$$\lambda_{min} = c_{min}/f_{max} \tag{4.13}$$

For data with a specific temporal frequency f, the spatial wavenumber of the data for a fully unaliased surface sampling is given by

$$k = \frac{f \; sin\,\Theta}{c_{min}}, \tag{4.14}$$

where c_{min} is the minimum velocity of the medium in which the receivers are located and Θ is the emergence angle of the propagating wave (*Brenders and Pratt*, 2007a). For vertical emergence (90°) the maximum horizontal data wavenumber (k_{max}) is:

$$k_{max} = \frac{f}{c_{min}} = \frac{1}{\lambda}. \tag{4.15}$$

According to the sampling theory, the full recovery of the wavenumber bandwidth of the wavefield is achieved when the data is sampled in the source and receiver gathers with a spatial sampling less than

$$\Delta_{samp} \leq \frac{\lambda}{2}. \tag{4.16}$$

According to *Brenders and Pratt* (2007a) those limitations correspond to a completely unaliased sampling, and thus represent a conservative limitation. The best results could be obtained when using a receiver spacing $\Delta r = \Delta_{samp}$ and a shot spacing of $\Delta s \approx 2\Delta_{samp}$ (*Takam-Takougang and Calvert*, 2011).

4.1.4 The starting model for the inversion

Choosing an accurate starting model is probably the most challenging part of the waveform modeling approach. Commonly starting models are derived from travel-time tomography methods. For the acoustic active-source waveform inversion, ray theory based approaches (*Zelt and Smith*, 1992; *Zelt and Barton*, 1998) are the preferred choice to derive an initial model (*Bleibinhaus*, 2011). Using the first-arrival travel-times only (*Zelt and Barton*, 1998) will produce the low-wavenumber solution while modeling velocity contrasts as gradients rather than boundaries (e.g. *Zelt and Barton*, 1998; *Brenders and Pratt*, 2007a). However, when using *Zelt and Smith* (1992)'s approach for travel-time inversion, secondary arrivals (reflections, refractions) are incorporated into the modeling and the the final velocity model has sharp velocity boundaries. In order to use these velocity model results for the waveform approach the model itself has to be smoothed.

According to *Pratt* (1999) the non-linearity of the inverse problem might be overcome and the misfit function will more likely lead to the global minimum when using a low-wavenumber starting model.

To test the eligibility of the starting model for the inversion procedure itself, the synthetic data generated in the forward modeling step using the starting model has to match the first arrivals of the observed data within 1/2 cycle of the wavelength. Otherwise the wrong cycles of the waveforms are matched which would result in a local rather than global minimum misfit solution.

4.1.5 Aliasing

Since both forward and inverse modeling are carried out in the frequency-domain, the forward modeled data have to be transformed into the time-domain using Fourier transformation (FT). Due to the periodicity of the FT, time-aliasing will likely be introduced into the time-domain data if the frequency sampling interval is not sufficiently small (*Brenders and Pratt*, 2007a). Hence, the frequency sample rate (Δf) is defined by the maximum time-window (T_{max}) of the seismic trace such as

$$\Delta f = \frac{1}{T_{max}}. \tag{4.17}$$

For a function $f(t)$, the discrete frequency-domain data will be transformed into an aliased time-function $f(t + nT_{max})$ (for $n > 1$) (*Brenders and Pratt*, 2007a). The aliasing can be suppressed by using a large T_{max}. This can become computationally expensive, as it requires a small value of Δf and hence a large number of frequencies.

To obtain the time-domain data $u(t)$, for each receiver location, a discrete series of $u(\omega)$ is computed with a range of frequencies using equation (4.4). Hence, the periodic time-domain signal is

$$\sum_{n=-\infty}^{\infty} u(t \, + \, nT_{max}), \tag{4.18}$$

By introducing a complex-valued angular frequency ($\omega' = \omega + \frac{i}{\tau}$) instead of ω, the problem of non-zero $u(t)$ values can be overcome. The Fourier transform of $u(t)e^{-t/\tau}$ is $u(\omega')$. Hence, an approximation of the original time-domain data can be expressed with

$$\sum_{n=-\infty}^{\infty} u(t \, + \, nT_{max})e^{-nT_{max}/\tau}. \tag{4.19}$$

For the unaliased component (n=0), the original time-domain data is recovered and for all positive values of n, the signal is attenuated by a minimum of $e^{-T_{max}/\tau}$. Further details of these assumptions can be found in *Brenders and Pratt* (2007a), where the time-damping factor τ is approximately calculated with $\tau \; \approx \; 0.4 * T_{max}$.

4.1.6 Frequency selection for the inverse modeling

As mentioned above, frequencies are chosen following the Nyquist sampling approach (Eq. 4.17). However, the number of frequencies can become very large due to a small sampling rate Δf if the seismic record is long. *Sirgue and Pratt* (2004) state that using a selection of frequencies can be sufficient for the inversion result. However, the "efficient" waveform tomography is strongly dependent on the shot-receiver offset.

The vertical wavenumber coverage k_z of a 1D thin layer for a given frequency is limited to the range $[k_{zmin}, k_{zmax}]$, with

$$k_{zmin} = 2k_0\alpha_{min}, \tag{4.20}$$

$$k_{zmax} = 2k_0, \tag{4.21}$$

$$\alpha_{min} = \frac{1}{\sqrt{1+R_{max}^2}}, \quad R_{max} = h_{max}/z, \tag{4.22}$$

where R_{max}, is the ratio of the maximum half-offset h_{max} and the depth of the target layer z. Hence, the minimum and maximum wavenumber k_z are produced by the furthest and nearest offsets, respectively (*Sirgue and Pratt*, 2004). The wavenumber k_0 can be written as $k_0 = \omega/c_0$, with $\omega = 2\pi f$. The wavenumber coverage of a multi-offset acquisition is

$$\Delta k_z = |k_{zmax} - k_{zmin}| \tag{4.23}$$

$$= 4\pi(1 - \alpha_{min})f/c_0, \tag{4.24}$$

and the wavenumber bandwidth is

$$\frac{k_{zmax}}{k_{zmin}} = \frac{1}{\alpha_{min}} = \sqrt{1+R^2} \tag{4.25}$$

The wavenumber coverage increases linearly with the frequency, while the wavenumber bandwidth is a function of offset-to-depth ratios (*Sirgue and Pratt*, 2004). Each frequency has a limited, finite-band to the image spectrum. To recover the target region accurately over a broad range of wavenumber, the continuous coverage of the target in the wavenumber domain must be preserved as the imaging frequencies are selected (*Sirgue and Pratt*, 2004):

$$k_{zmin}(f_{n+1}) = k_{zmax}(f_n) \tag{4.26}$$

where f_{n+1} is the next frequency to be chosen following the frequency f_n. Using this condition and equation (4.22) give the following selection scheme:

$$f(n+1) = \frac{f(n)}{\alpha_{min}}. \tag{4.27}$$

The frequency increment Δf_{n+1} is given by

$$\begin{aligned} \Delta f_{n+1} &= f_{n+1} - f_n \\ &= (\frac{1-\alpha_{min}}{\alpha_{min}})f_n \\ &= (1-\alpha_{min})f_{n+1}. \end{aligned} \tag{4.28}$$

The frequency increment is not constant, but increases linearly with the frequency (*Sirgue and Pratt*, 2004). For further details refer to *Sirgue and Pratt* (2004).

4.2 The application of waveform inverse modeling to OBS data

Within this section the waveform inversion is carried out on synthetic OBS data generated with simplified velocity models that are based on modeling results from travel-time inversion of the 2006 OBS data and inversion results from *Delescluse et al.* (2011) from the study area. In the subsequent section, the waveform inverse method is applied to the 2006 OBS data with a starting model based on the results from travel-time inversion in chapter 3. Within this study phase-only inversion was applied to the synthetic and real OBS data, because the phase of the seismic waveform in strongly influenced by velocity changes (*Kamei*, 2012). Phase-only inversion provides more stable P-wave velocities than phase+amplitude inversion (*Kamei*, 2012). However, phase+amplitude inversion results can provide more information on geological structures as studies by e.g. *Delescluse et al.*

(2011) and *Takam-Takougang* (2011) have shown. Attenuation strongly influences the amplitudes of the seismic data. Hence, phase+amplitude inversion incorporates those effects into the modeling. However, the P-wave velocity contrasts applied to the model of this study show small velocity contrasts. Therefore, we infer small S-wave velocity contrasts for the model and small attenuation effects on the seismic data.

As already mentioned travel-time inversion methods use only the high-frequency content of the data (*Brenders and Pratt*, 2007a), while waveform inverse method generally starts with the lowest available frequency in the data to obtain the general background information of the velocity structure. The seismic waveform itself provides more information about the medium the wave propagated through than the travel-time arrivals alone (*Brenders and Pratt*, 2007a).

The travel-time inversion models (Figs. 3.10 and 3.19 - chapter 3) give little information about the velocities below the BGHSZ. Although refracted arrivals that originated from greater depths with apparent velocities around 2.4 km/s were recorded on few OBSs, they could not be modeled sufficiently within the travel-time inversion.

The travel-time inverse modeling also showed that the selected survey geometry is important for the final ray-coverage and therefore for the modeled 2-D velocity structure. The modeling examples presented in the next sections using synthetic OBS data and the waveform inversion approach provide an overview of suitable survey geometries that can be used to get the best velocity information for the subsurface structure of the study area.

Modeling with synthetic seismic OBS data

To generate synthetic OBS data, the final velocity model results obtained through travel-time inversion (Chapter 3) and results based on studies by *Delescluse et al.* (2011) were combined (Fig. 4.1). In a first step, the width of the model was extended from 12 km to 30 km. This was necessary to obtain refracted arrivals that originate at depths below the

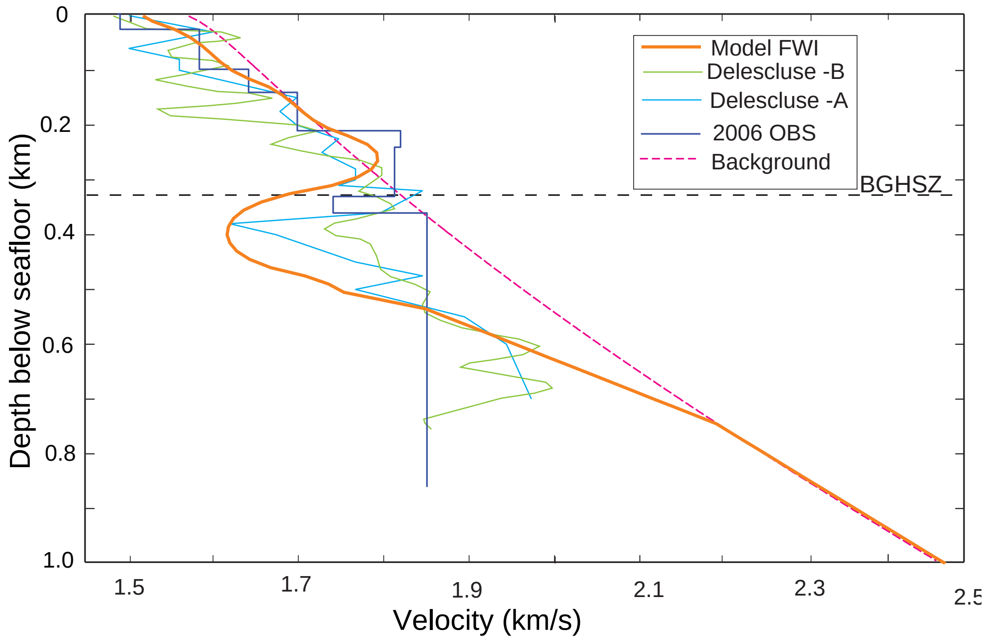

Fig. 4.1: Comparison of 1-D profiles of the original velocity model used in the waveform modeling (orange) with results from travel-time inversion on the 2006 data of this study (blue), and the FWI results obtained by *Delescluse et al.* (2011) for two profiles: A (cyan) and B (green). The background velocity profile (dashed pink) was calculated using simple rock physics models and modeling parameters taken from *Mosher* (2004).

LVZ, the target region of this study. Hence, the shot and receiver numbers were increased to allow wider offsets.

In water depths of 1.6 km, the velocity increases from ~1.5 km/s at the seafloor to a maximum of 1.79 km/s at 250 mbsf. The velocity drops to 1.62 km/s at 400 mbsf and then steadily increases with increasing depth (Fig. 4.1). The thickness of the LVZ is ~150 m. Below the velocity increases with depth to a maximum of 2.8 km/s at 3 km below sealevel. The background velocity profile that corresponds to the shallower and deeper part of the model was derived using effective medium theory approaches based on rock-physics models (*Helgerud et al.*, 1999). However, there are no borehole data or core-samples available to constrain lithologies or velocities.

To generate synthetic seismograms, velocities are uniform laterally and the above velocity-depth profile occurs at all locations. This model represents the known target model, and synthetic seismograms through it represent the recorded data. As a starting model for the inversion, the velocity varied only within the LVZ at a target depth near 2 km. Here, the velocity was increased by five percent (80 m/s) relative to the original velocity value of 1.62 km/s (Fig. 4.2).

According to equation (4.13) the maximum grid sampling rate was calculated as 17.6 m using a maximum frequency of 21 Hz and a minimum velocity of 1.48 km/s. The maximum of the frequency spectrum was chosen according to the frequency content of the source-signal, a Ricker wavelet with a peak-frequency of 10 Hz and a frequency band up to 40 Hz (Fig. 4.3). For the modeling the chosen grid spacing was set to 15 m.

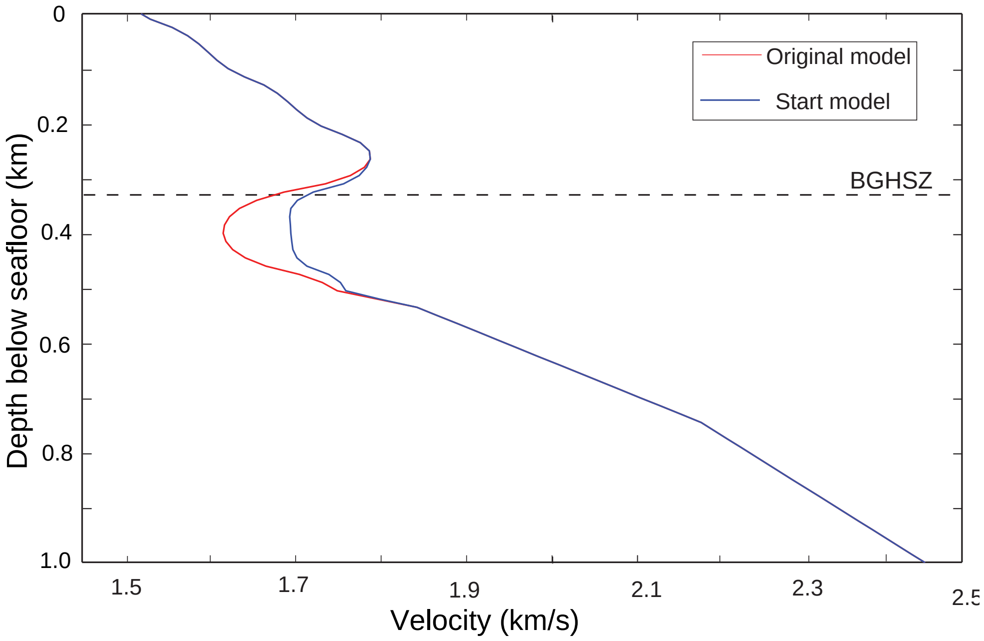

Fig. 4.2: Comparison of 1-D profiles of the upper sections from the 2-D velocity models of the original model (orange) and the starting model (blue) with 5% velocity increase (80 m/s) in the low-velocity region.

Model geometries

The modeling requirements of equation (4.16) in chapter (4.1.3) were considered while selecting the source and receiver geometry using a minimum model velocity of 1.48 km/s

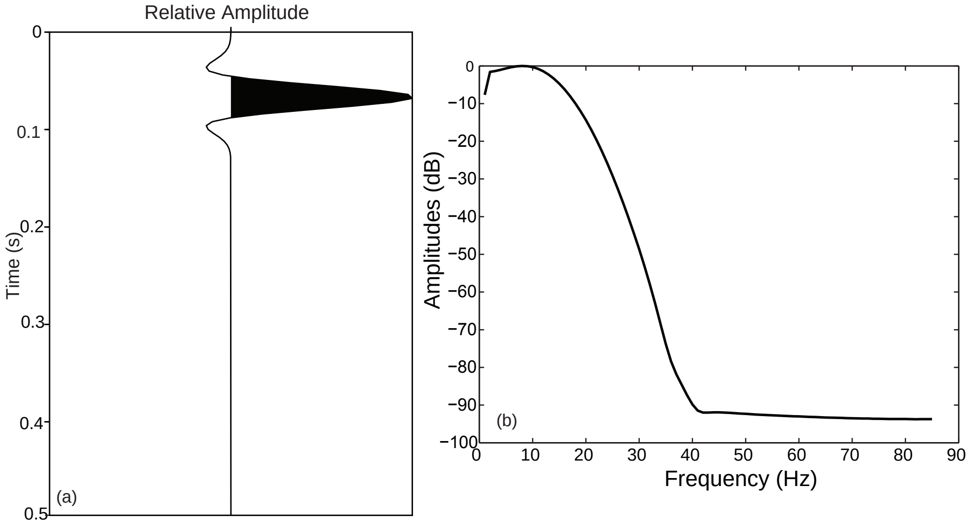

Fig. 4.3: (a) Source signature and (b) amplitude spectrum of the modeled seismic source. A Ricker wavelet was chosen with a peak-frequency of 10 Hz and a frequency range up to 40 Hz.

and a maximum frequency of 21 Hz (Table 4.1). The OBS survey geometry is obviously different from MCS survey configurations that were recently used in waveform modeling (*Pratt*, 1999; *Shipp and Singh*, 2002; *Sirgue and Pratt*, 2004; *Brenders and Pratt*, 2007a; *Delescluse et al.*, 2011). While receiver numbers are smaller for OBS surveys compared to MCS surveys, the receiver spacings are much wider (>100's m).

Throughout all subsequent models presented in this chapter the number of shots (779) and the shot-spacing (25 m) were kept constant. The receivers are positioned between 12.225 km and 17.225 km profile distance. The receiver spacings and instrument numbers varied for the different modeling scenarios (100 m, 200 m, 500 m, and 1 km). The instrument spacing is dependent on the main frequency (Eq. 4.16, Chapter 4.1.3) and decreases with increasing frequency (Table 4.1). To avoid alias effects from the model boundaries, the first and last shot were set at 5 km and 24.45 km, respectively, leaving a ~5 km distance to the absorbing model boundaries. To avoid boundary reflections, the velocity model was padded with 15 grid points to each side and absorbing boundaries were implemented.

c_{min} (m/s)	f (Hz)	λ (m)	$\Delta_{samp} = \lambda/2$ (m)	2 Δ_{samp} (m)
1480	3	493	247	494
1480	5	296	148	296
1480	7	211	106	212
1480	9	164	82	164
1480	11	135	67	134
1480	13	114	57	114
1480	15	96	49	98
1480	17	87	44	88
1480	19	78	39	78
1480	21	70	35	70

Tab. 4.1: Comparison of frequency ranges and instrument sampling according to equation (4.16) in section 4.1.3.

Frequency selection for the forward modeling

For each different shot-receiver configuration forward modeling was carried out to generate synthetic data from the original model and the starting model for the inversion. A total of 84 frequencies were used from 0.25 Hz to a maximum of 21 Hz. According to the Nyquist sampling theorem (Eq. (4.17)) a frequency sampling rate of Δf of 0.25 Hz for a total seismic record length of $T_{max} = 4s$ was applied. A reduction velocity of 2.4 km/s is applied to the seismic data in the recorded time-window of 4 s. Reduced time is applied to decrease the recorded time-window length and the number of frequencies used by increasing the frequency interval.

4.2.1 Forward modeling and inversion

In an initial forward modeling step, synthetic seismic data (Fig. 4.4 a) were generated with the velocity model (orange - Fig. 4.1) and the selected geometry for 51 OBSs. To simulate real seismic surveys, the 51 OBSs were placed along the 30 km long profile with a 100 m instrument separation. The first OBS was placed at 12.225 km profile distance and the last

OBS was set at 17.225 km profile distance. All receivers were located in a water depth of 1.65 km. This configuration produces a maximum shot-receiver offset of 12.225 km for the outer-most instruments.

To identify the arrivals in the synthetic seismograms (Fig. 4.4 a) the ray-tracing forward modeling approach by *Zelt and Smith* (1992) was applied to a velocity model derived from the original model (Fig. 4.4 c,d). The model that was used in the ray-tracing approach was generated with interfaces and velocities based on the original model used for the waveform forward modeling and inversion (Fig. 4.4 d). The turning wave arrivals from the high-velocity region above the LVZ are modeled at a depth of ~240 mbsf with an apparent velocity of 1.8 km/s (Fig. 4.4 (b-yellow arrivals)). A number of turning waves are modeled from the region below the LVZ generated from the velocity gradient starting in a depth range of 450 mbsf (Fig.4.1). These arrivals have apparent velocities of 2.3 to 2.6 km/s (Fig. 4.4 (c) - green, magenta, rose) and appear at 1.5 s in the seismograms. The reflected arrival generated at the depth of the LVZ (450 mbsf) was modeled with 1.6 km/s velocity (Fig. 4.4 b,c - blue). However, a deeper arrival starting off at 2.1 s from the direct arrival (Fig. 4.4 a - (4)) has a similar velocity. This arrival is most likely a delayed wave-effect arrival due to the decreasing velocity in the LVZ. This can be shown when modeling the original velocity model with a smooth gradient instead of the LVZ for the ~150 m thick layer (Appendix - 6.3.2). The delayed LVZ arrival arrives earlier in time (1.7 s) and merges into the arrivals generated from HVZ (Appendix - 6.3.2 b). The difference between both data sets is shown in a residual plot (Appendix - 6.3.2 c).

In the next step the starting model (Fig. 4.2-blue) was used to generated synthetic seismic data with the forward modeling through the waveform approach. Comparing forward modeled data and the original synthetic data shows that the arrivals from the direct wave and the waves generated at the top of the LVZ (Fig. 4.5) are within 1/2 of the wavelength. The arrivals generated from the velocity gradient (2.3-2.6 km/s) below the LVZ also fulfill

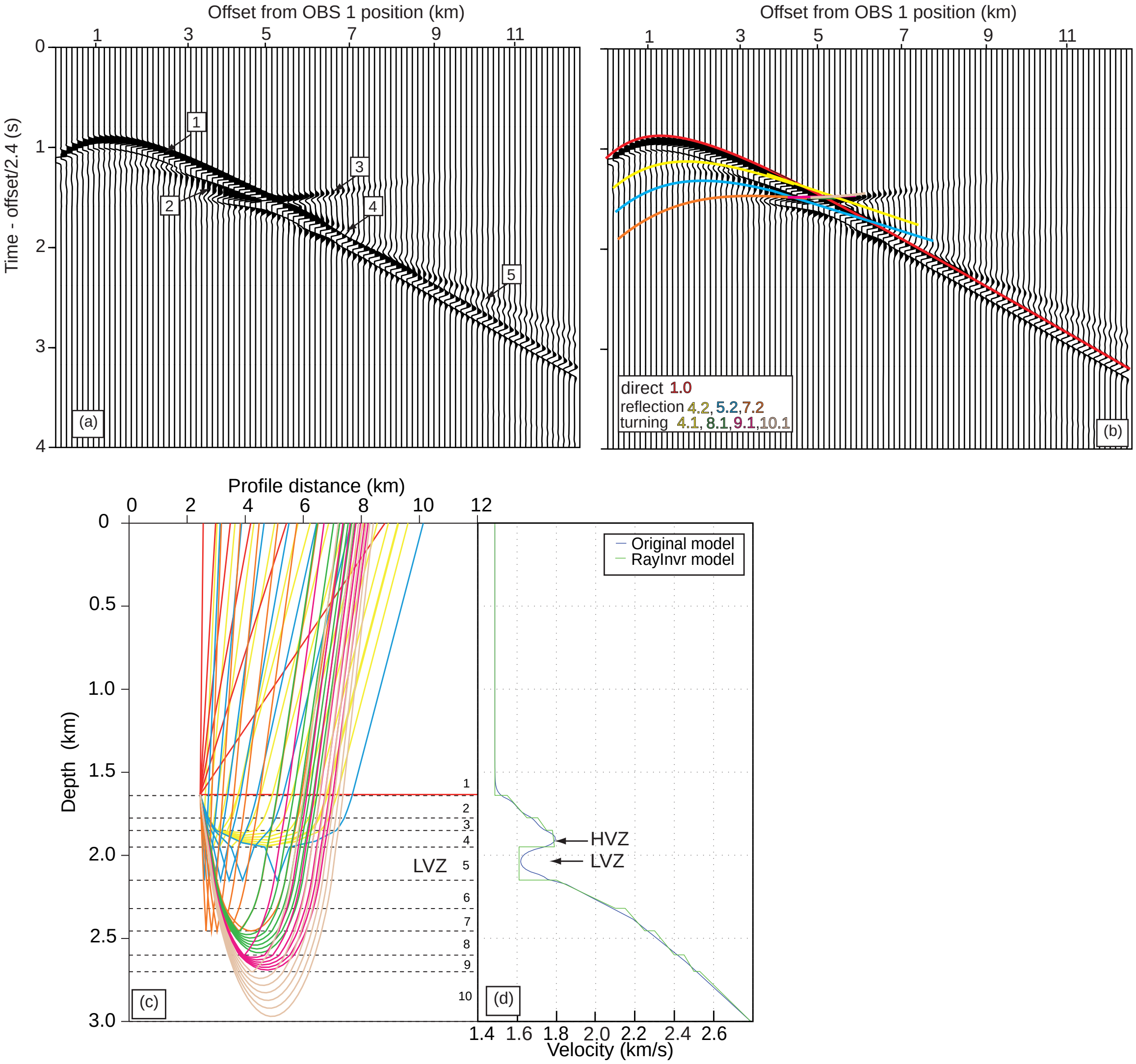

Fig. 4.4: (a,b) Synthetic seismic data in reduced time (2.4 km/s) for OBS 1 (at 12.225 km profile distance) using the original velocity model (orange-Fig. 4.1). The significant arrivals are labeled: (1) direct arrival (red), (2) reflections and refractions (1.8 km/s apparent velocity) generated from the top of the LVZ (yellow), (3) turning waves from the deeper part of the model below the LVZ (orange), (4) reflections from the bottom of the LVZ (blue) (5) delayed wave-effects related to the LVZ. The modeled travel-time arrivals were generated through forward modeling with *Zelt and Smith* (1992) routine using a velocity model (d-green) derived from the original model (d-blue). (c) Ray-tracing through a layered model derived from the original waveform model (d-blue) with the routine of *Zelt and Smith* (1992) was applied to identify the arrivals in (a,b). (d) 1-D profiles of the original model (blue) and the model used for the forward modeling ray-tracing approach (green).

the requirement. The delayed LVZ arrivals are barely within half a wavelength, but still eligible for the inversion (Fig. 4.5).

Frequency domain input data

The synthetic data were generated through forward modeling using the original model and the frequency-domain data input were generated through Fourier-Transformation of the time-domain data containing both amplitude and phase. Figure 4.6 shows the real part of the frequency-domain data for different frequency components. The diagonal shows the maximum values for near-offset shots for each receiver and the values decrease with increasing offset (off-diagonal values). The frequency domain data of frequencies between 4 and 10 Hz have higher values than the data for frequencies lower than 4 Hz and larger than 14 Hz. These amplitude differences are related to the frequency spectrum of the source.

Inverse modeling

Previous modeling tests and studies by *Sirgue and Pratt* (2004) and *Brenders and Pratt* (2007a) have shown that using the "whole" frequency range or a large number of frequencies for the inversion is not necessary. In *Sirgue and Pratt* (2004) a so-called "efficient" frequency selection method was introduced based on the maximum shot-receiver offset of the survey (see section 4.1.6). With the shot-receiver geometry of this study, only three frequencies (2, 6.25, and 19.5 Hz) were needed for the "efficient" waveform inversion method. However, similar to the approach chosen by *Delescluse et al.* (2011) a more conservative frequency selection was applied using 16 frequencies from 2 to 17 Hz with a 1 Hz interval. Each frequency was inverted individually. The velocity model obtained after four iterations was applied as startmodel for the inversion using the next higher frequency.

The inversion result on 100-m-spaced OBSs shows that the velocity update over the target depth range (1.9 - 2.1 km) was achieved between 9 and 21 km profile distance (Fig.

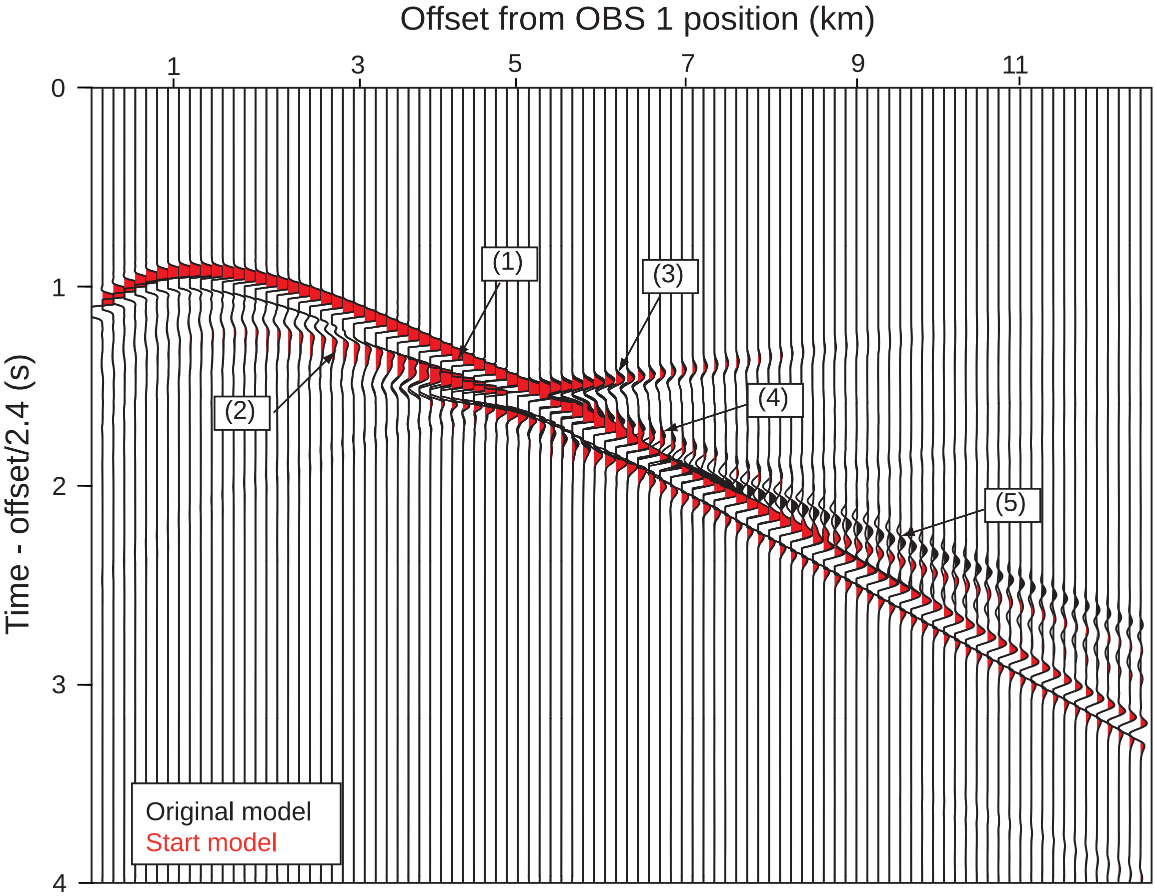

Fig. 4.5: Comparison of the synthetic data generated with the original model (red) and generated with the starting model (black) using frequencies up to 21 Hz with a 0.25 Hz frequency interval. The direct wave (2), arrival from the top and bottom of the LVZ (2), and the turning wave arrivals from the deep part of the model (3) are within 1/2 cycle. However, the arrivals from the bottom of the LVZ (4) and the delayed arrivals due to the LVZ (5) differ because of the differences in LVZ velocities. The delayed arrivals are barely within half a wavelength of each other.

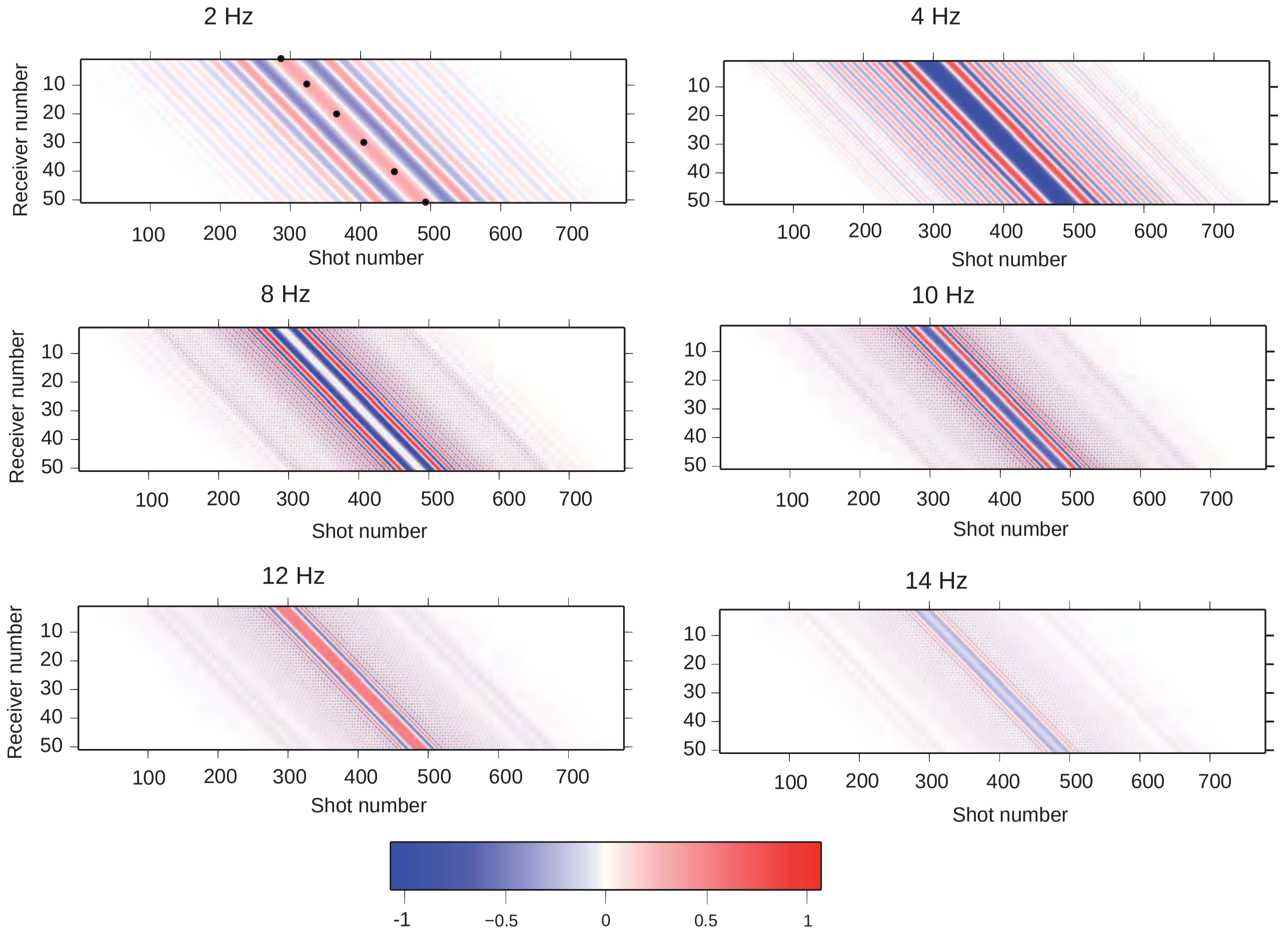

Fig. 4.6: Frequency domain data of 2, 4, 8, 10, 12, and 14 Hz components. The maximum values of each frequency component are concentrated along the diagonal in the middle of the profile (shots 300 to 500) where the OBS positions are located (2 Hz - black dots indicate every 20th receiver position). The values decrease for increasing shot-receiver offsets (off-diagonal values). The highest values are for frequencies between 4 and 10 Hz.

4.7 (a) - black box). The recovered target area (black box) shows a smooth velocity distribution.

To investigate the limits of instrument spacing, three experiments with wider receiver spacings were configured using the same velocity models. As mentioned in section (4.1.3)) and according to *Brenders and Pratt* (2007a) the limits of instrument spacing shown by equation 4.16 and in table 4.1 are too conservative. Hence, OBS instruments were chosen with 200 m, 500 m, and 1 km instrument separation.

The previous modeling with 51 instruments and a receiver spacing of 100 m resulted in an instrument coverage of 5.1 km profile length (Fig. 4.7 a). However, during the inversion ~12 km profile length could be recovered. In the next steps the region of the OBS array was kept constant (12.225 to 17.225 km profile distance), but the number of instruments was decreased while the instrument spacing was increased in each step.

The final model result using 26 OBSs with a 200 m spacing (Fig. 4.7 b) shows a very similar velocity update as in the previous run with 100-m spaced instruments, where the black box indicates the model update range (9 to 21 km) from the previous modeling. Increasing the instrument spacing to 500 m and 1 km shows that the smoothness of the model within the target region (black box) is decreasing (Fig. 4.7 c,d). Modeling with 6 OBSs using a 1-km spacing (Fig. 4.7 d) shows a strong velocity perturbation at greater depths (below 2.2 km), where both the original and starting model have the same velocity values.

4.2.2 Average velocity profiles from the different modeling schemes

To compare the final model results from all four instrument spacings, individual 1-D profiles were taken from the 2-D velocity models (Fig. 4.8). Within the range where the target region (LVZ) was well recovered (Fig. 4.7 - black box) 1-D vertical velocity profiles were taken every 150 m. Each plot of figure 4.8 shows a 1-km window of the profile between 9

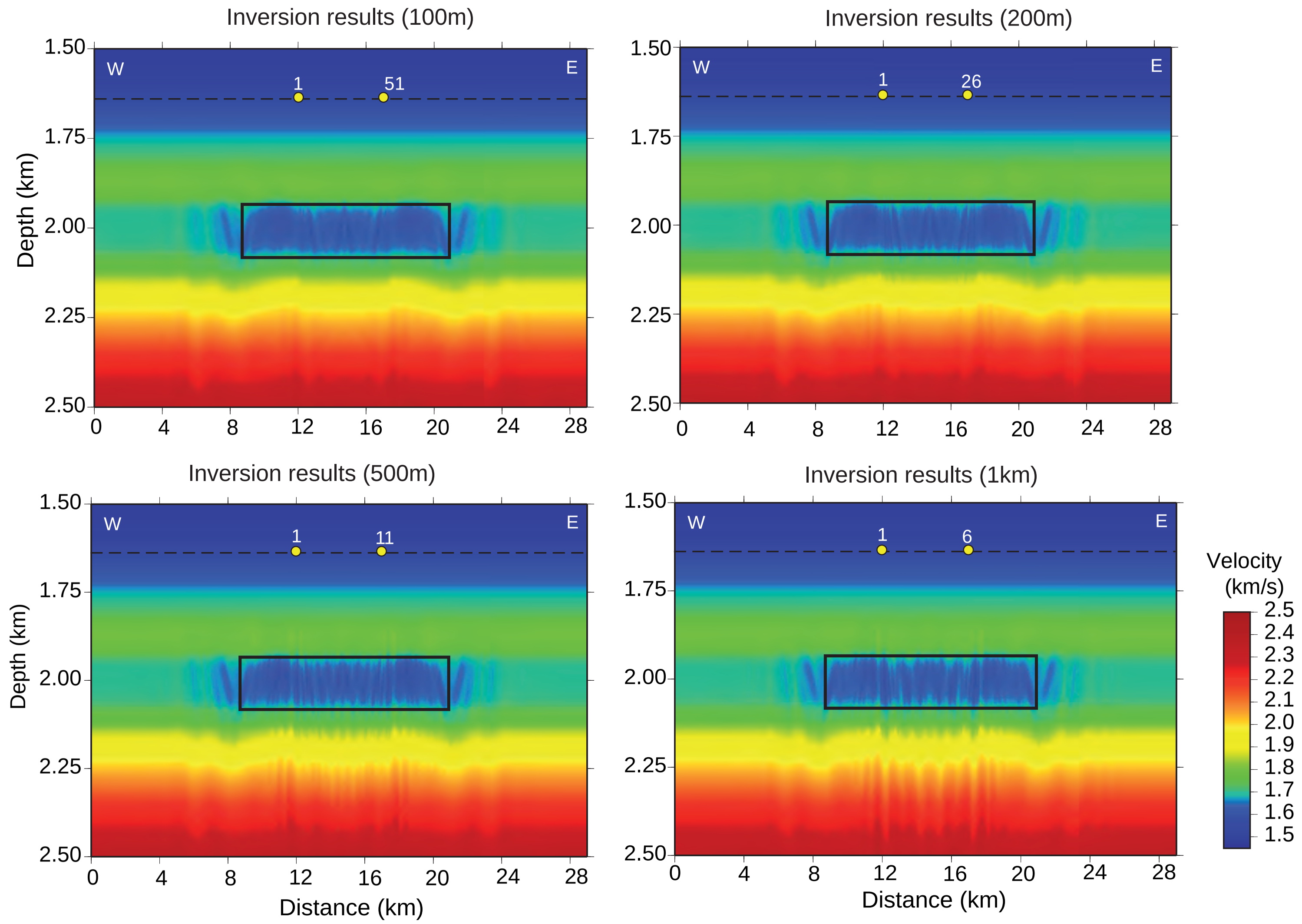

Fig. 4.7: Final velocity model result from waveform inversion on (a) 51 OBSs (100-m spacing), (b) 26 OBSs (200-m spacing), (c) 11 OBSs (500-m spacing) and (d) 6 OBSs (1-km spacing) using 779 shots and 16 frequencies (2-17 Hz). The main model update was achieved near the target depth (2 km) between 9 and 21 km profile distance (black box). The smoothness of the model update decreases with increasing instrument spacing.

and 21 km profile distance where six 1-D profiles were averaged. The comparison shows that the model results from all spacings fit the true model (red) reasonably well within ± 0.02 km/s, where the difference between starting and original model was a maximum of 0.08 km/s.

4.2.3 Verification of the Inversion Results

In order to investigate the reliability of the inversion, the velocity model result was applied in a forward modeling run to generate synthetic seismic data using only the frequency range that was applied in the inversion (2-17 Hz). These data were compared to the original synthetic seismic data (Fig. 4.4), that were bandpass filtered (2-17 Hz) for comparison. The residuals between the original modeled data and the forward modeled data using the inversion result show the main differences between those two data sets. While the residuals for 100-m spaced OBSs between the original data and the modeled data with the starting model show main amplitude difference for the turning wave and the delayed LVZ arrival (Fig. 4.9 top), the residuals from the original and modeled data using the inverse velocity result show mainly amplitude differences for the critical angle at ~5 km offset from the OBS position. Final residuals for the 200-m spaced and 500-m spaced OBS arrays (Fig's. 4.10, 4.11) show that the main amplitudes are associated with the arrivals from below the LVZ. The final residuals for the 1-km spaced OBS array (Fig. 4.12) show the main difference in amplitude for the critical angle.

4.2.4 Source Estimates

Source signatures were calculated using the waveform routine and the final velocity models from inverting with the different OBS spacings. The inverted source was compared to the

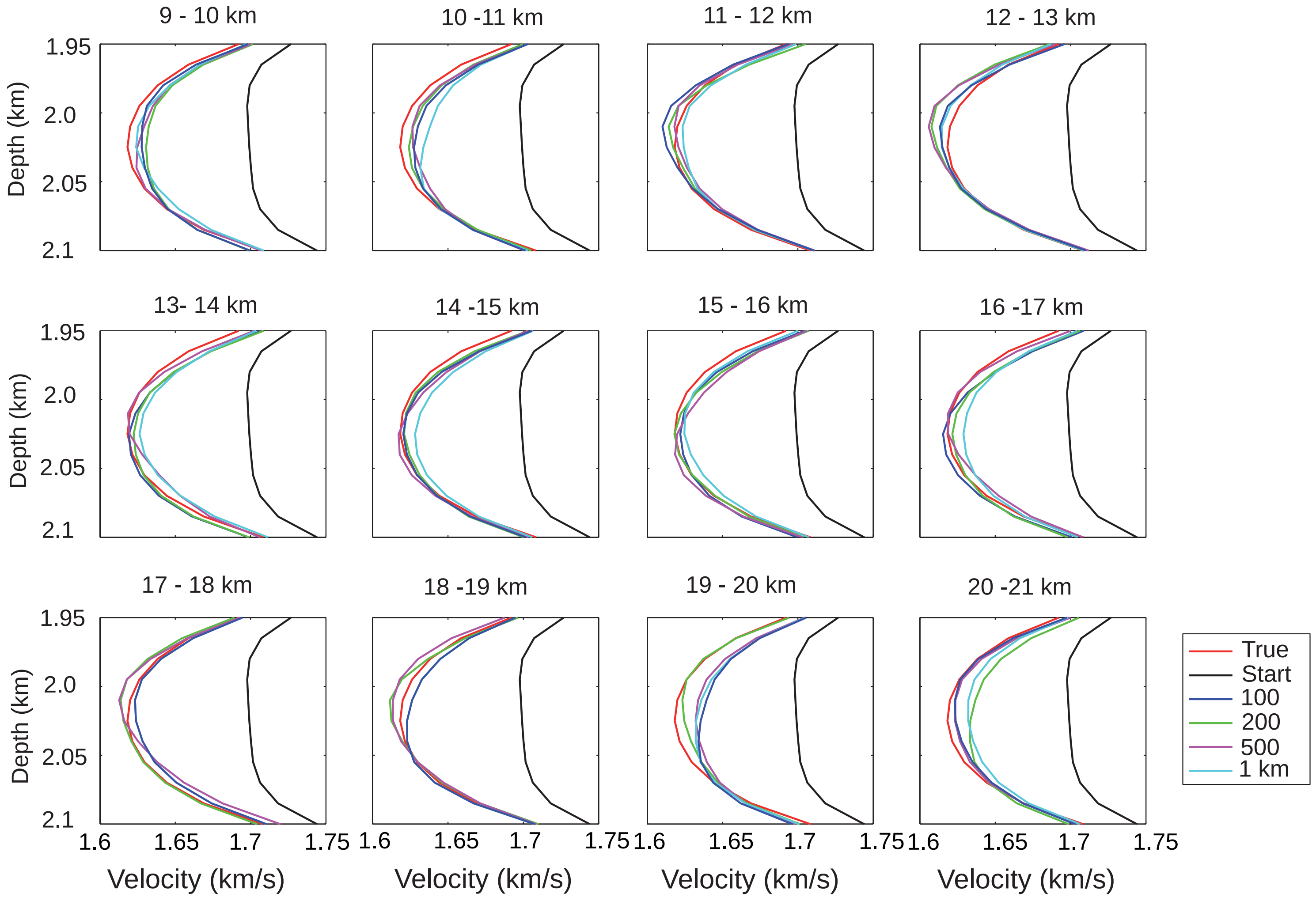

Fig. 4.8: Comparison of averaged 1-D profiles for OBS spacing along the 2-D velocity profile within a range of 9 to 21 km profile distance. Vertical velocity profiles were taken every 150 m and averaged over a 1 km range. The velocity results from all OBS spacing runs seem to fit the true model (red) reasonably well within ± 0.02 km/s.

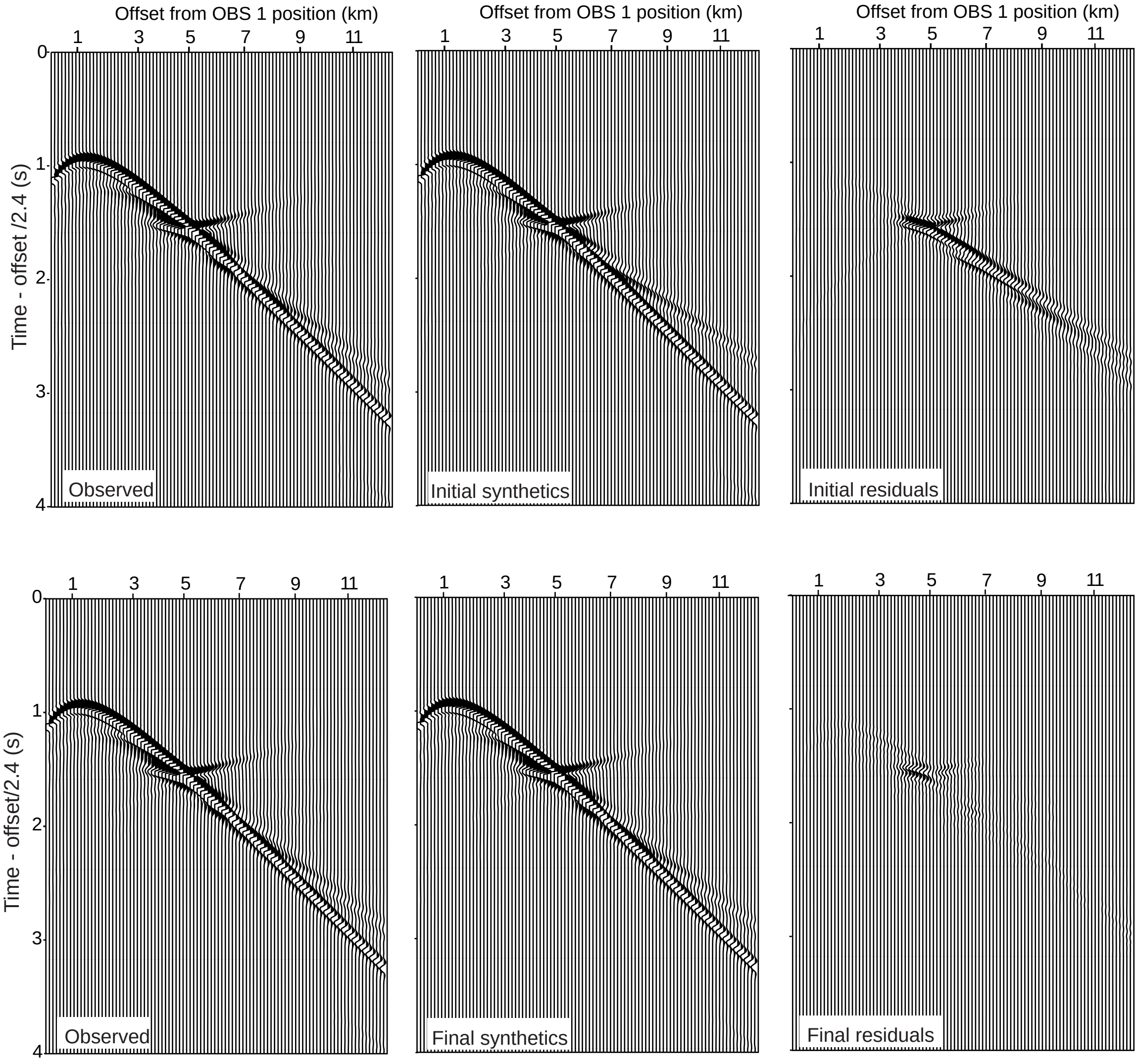

Fig. 4.9: Comparison of bandpass filtered (2-17 Hz) modeled OBS 1 data (100-m-spaced array) that were generated with the original model (observed), synthetic data generated with the starting model (initial synthetics), and the final synthetic data generated with the inversion result model (Fig. 4.7 a). The initial residuals and final residuals are plotted as well to better compare the inversion results.

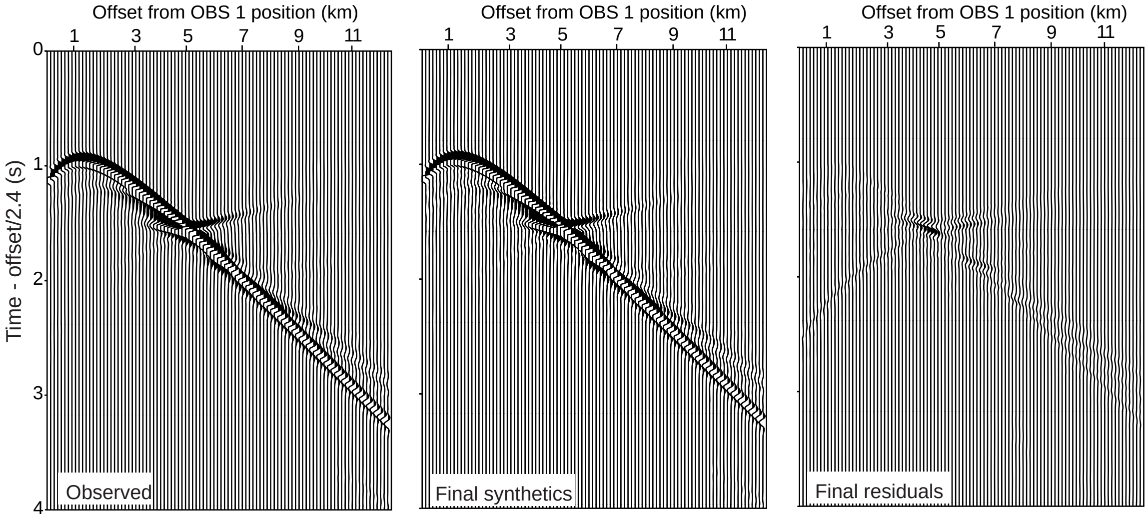

Fig. 4.10: Comparison of bandpass filtered (2-17 Hz) modeled modeled OBS 1 data (200-m-spaced array) data that were generated with the original model (observed) and the synthetic data generated with the final inversion result (Fig.4.7a). The final residuals between these data sets are shown.

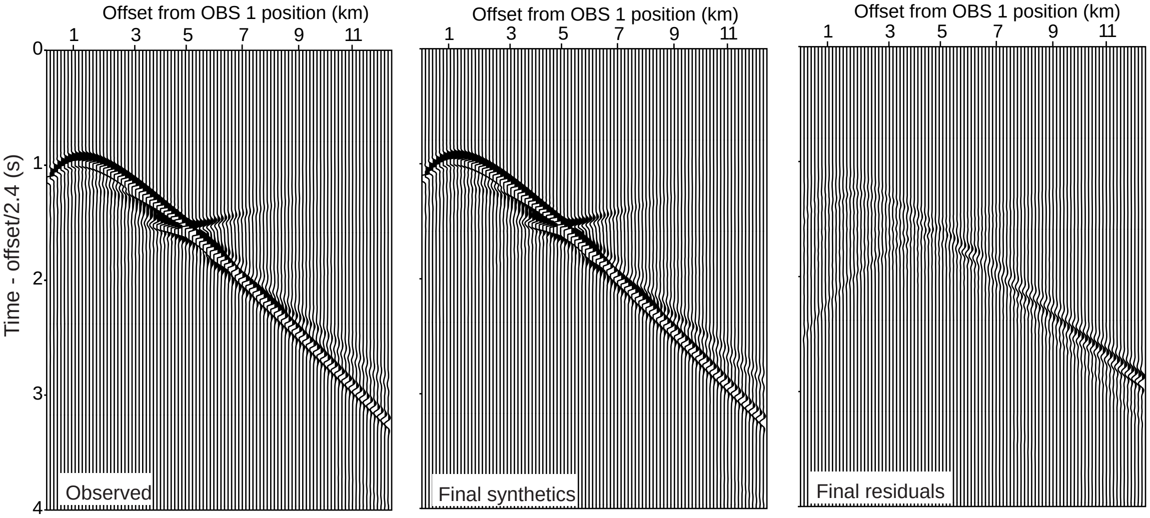

Fig. 4.11: Comparison of bandpass filtered (2-17 Hz) modeled modeled OBS 1 data (500-m-spaced array) data that were generated with the original model (observed) and the synthetic data generated with the final inversion result (Fig.4.7b). The final residuals between these data sets are shown.

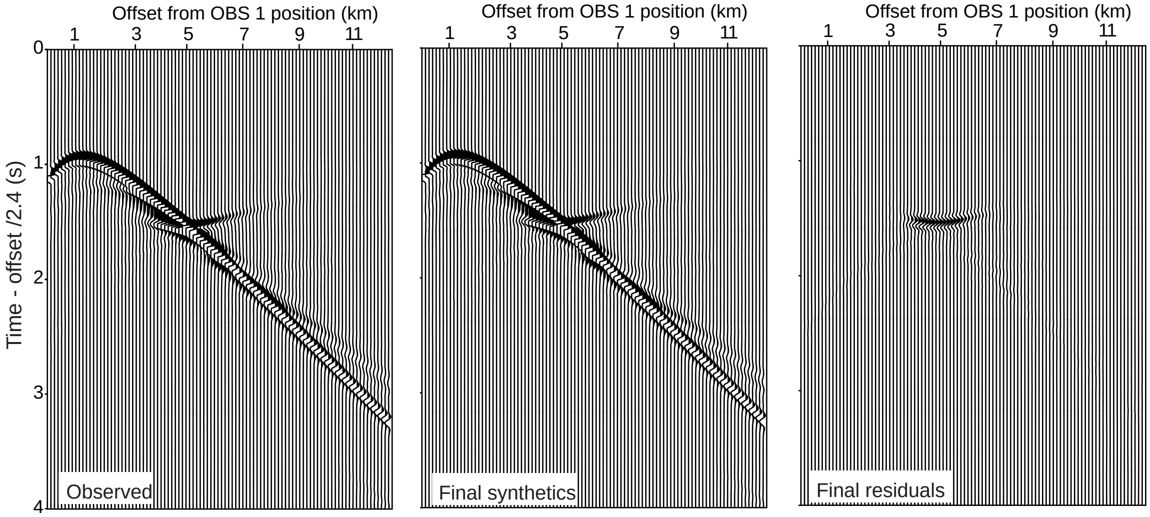

Fig. 4.12: Comparison of bandpass filtered (2-17 Hz) modeled modeled OBS 1 data (1-km-spaced array) data that were generated with the original model (observed) and the synthetic data generated with the final inversion result (Fig.4.7c). The final residuals between these data sets are shown.

original Ricker wavelet (Fig. 4.13). The comparison shows that the generated wavelets are recovering the original wavelet (red). However, the bandwidth of the wavelets is limited by the frequencies used for the modeling (2 to 17 Hz), whereas the original source wavelet contains more frequency information ($\leq$1 Hz to 21 Hz).

4.2.5 Inverse modeling with noisy synthetic OBS data

In real seismic data, noise can play an important role for identifying seismic arrivals and the original waveforms. Since the original data used in this study are very noisy with a S/N ratio of 1.25 (80 $\%$ noise) for the refracted data arrivals, several noise levels were tested in this section. Noise was added to the synthetic data generated with the original model (Appendix 6.4) for the 1-km-spaced OBS array. This setup was chosen to be comparable with the real 2006 OBS data from this study.

The inversion results using data with small amounts of added noise (2 $\%$) show a regeneration of the low velocity region (Fig. 4.14 a) similar to the results with noise-free

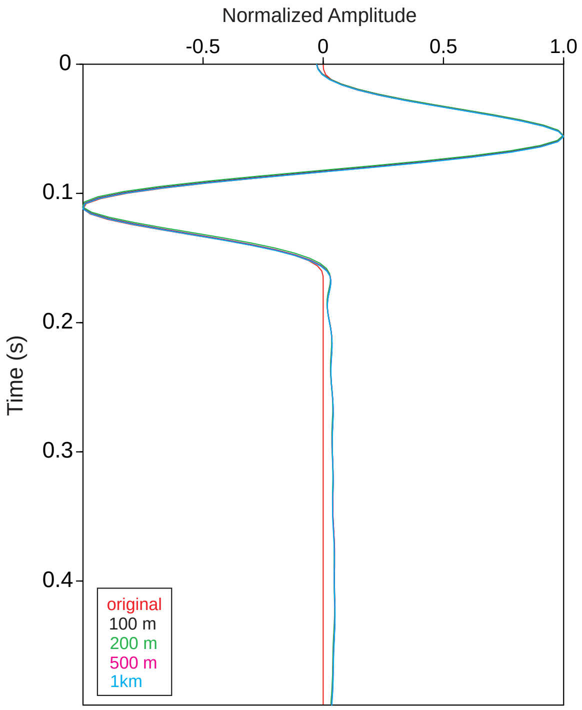

Fig. 4.13: Comparison of the original source wavelet (red) with the calculated source wavelets for inversion results using 51 OBSs (black), 26 OBSs (green), 11 OBSs (magenta), and 6 OBSs (cyan). The calculated wavelets are similar to each other, but slightly differ from the original source wavelet (after 0.17 s) which is due to the limited frequency band of 2 to 17 Hz.

data (Fig. 4.7 d). Additional model test with 5 %, 10 %, 20 %, 40 %, and 80 % noise on the original noise-free data were run. While the inversion result for data with 10 % added noise shows still a reasonable well recovered target region (Fig. 4.14 b - black box), the inversion result from data with a noise level of 20 % shows a loss in velocity smoothness of the recovered low-velocity region (Figs. 4.14 c). An increase in noise level to 80 % decreases the model smoothness (Figs. 4.14 d) and Appendix 6.3.4 a,b). Inversion results of 80 % additional noise on the data shows velocity structures above the target depth (1.9 km) with higher velocities (>1.9 km/s) than the surrounding region (1.75 km/s) (Fig. 4.14 d).

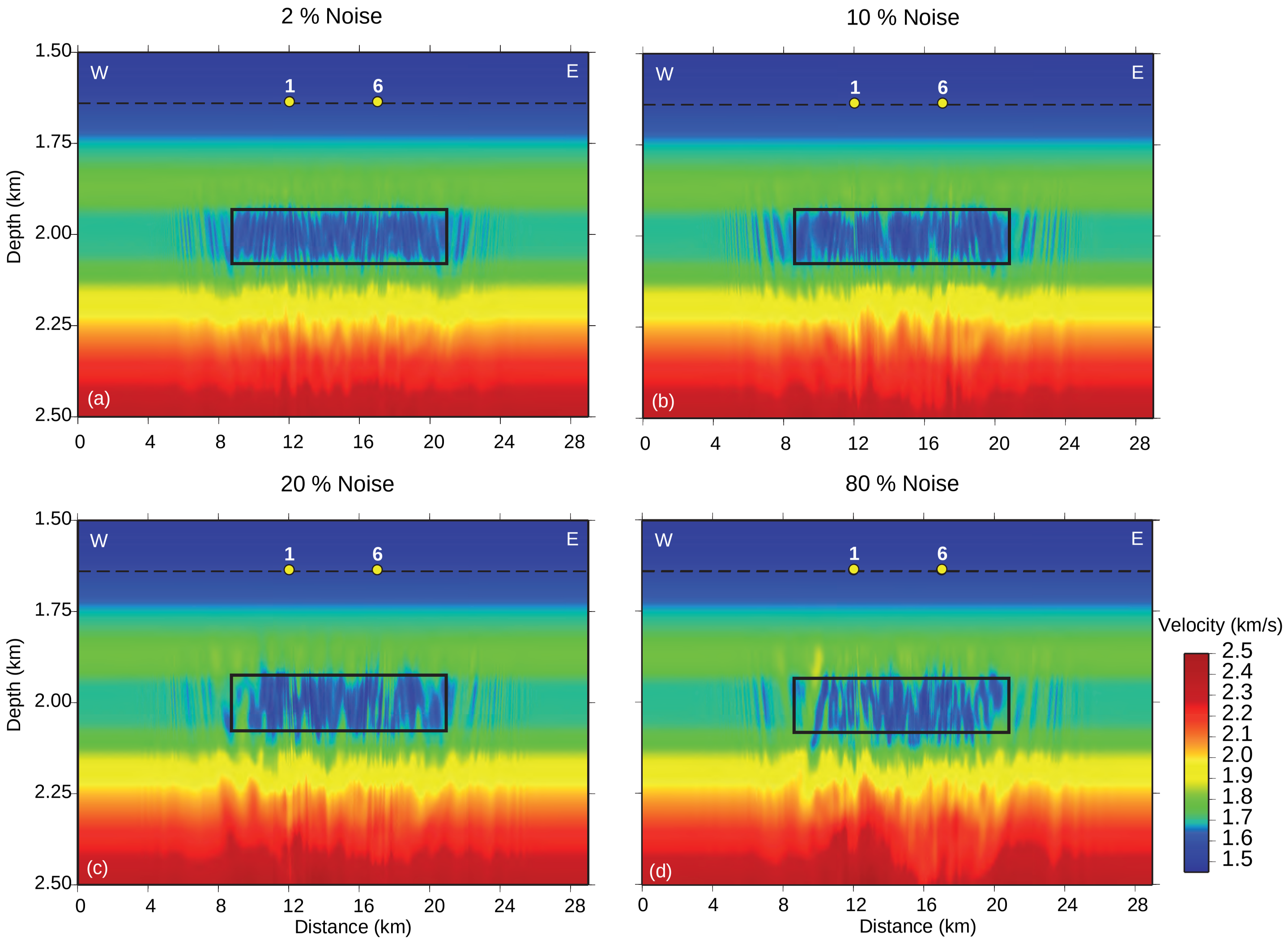

Fig. 4.14: Comparison of inversion results using synthetic seismic data for the 6 OBSs (1 km) with (a) 2 % , (b) 10 %, (c) 20 % , and (d) 80 % additional noise on the data (inversion results of 5 % and 40 % added noise are shown in Appendix 6.3.4). The increase of noise reduces the level of smoothness and the width of the target zone (black box). Inversion on data with 80 % added noise (d) shows higher velocity values (>1.9 km/s) than the surrounding region (1.75 km/s).

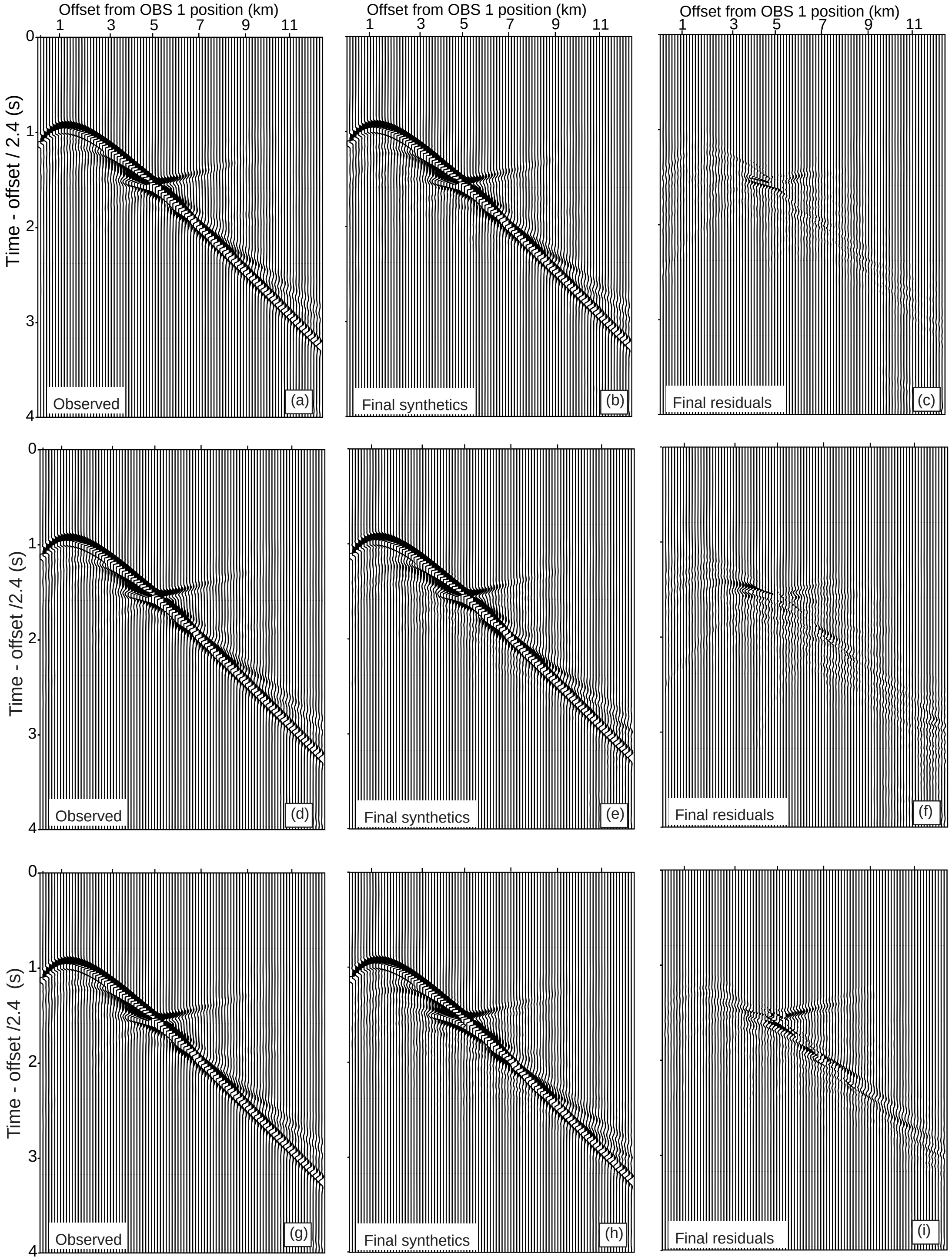

Fig. 4.15: Comparison of noise-free OBS 1 data (1-km spaced array) with synthetic data generated with the final results using (a-c) 2 % noise on the original data, (d-f) 10 % on the original data, (g-i) 80 % on the original data.

Similar to the inversion results with noise-free data (Fig.4.12), the inversion results from the noisy data were applied in forward modeling to generate synthetic data (2-17 Hz). Residuals from the original noise-free data and the data modeled with the inversion results from noisy data (Fig. 4.14) were calculated. The results show that a small amount of noise (2 %) already has an impact on the inversion result (Fig. 4.15 b,c). The synthetic data residuals show higher amplitudes for the critical angle and the turning wave compared to the residuals from noise-free data (Fig. 4.12). Residuals from modeled data using the inversion result of 80 % noisy data (g-i) show an increase in residual amplitude for the arrivals from below the LVZ and the turning wave).

4.2.6 Resolution tests: 100 m, 600 m, and 1 km

Corrugation patterns are perturbations of the original velocity field to test the lateral resolution of the model. In this study the low velocity region between 1.9 and 2.1 km depth was perturbed with a velocity change of ±80 m/s (5 %) from the original velocity (1.62 km/s). The positive perturbation of +80 m/s was already applied to the starting model for the inversion (Fig. 4.2). Within this study the corrugation patterns were applied with 100 m, 600 m, and 1 km cells (Fig. 4.16). With those perturbed velocity models, synthetic data were generated using 1-km spaced OBS geometry and 779 shots (25 m). Inversion on the original model were run using these generated data and the 16 frequencies from 2 to 17 Hz, with the original velocity model.

The difference between the original model and the inversion results for the corrugation test using a 100 m wide cell-pattern (Fig. 4.16a) shows that only a range of 300 m directly below each instrument's position was recovered in the target depth (black box). Increasing the cell-width to 600 m shows that the corrugation pattern can be recovered over the whole 5 km range below the OBS positions (Fig. 4.16b - black box). However, the vertical cell structure seems to be tilted for most of the cells outside the range of the instruments

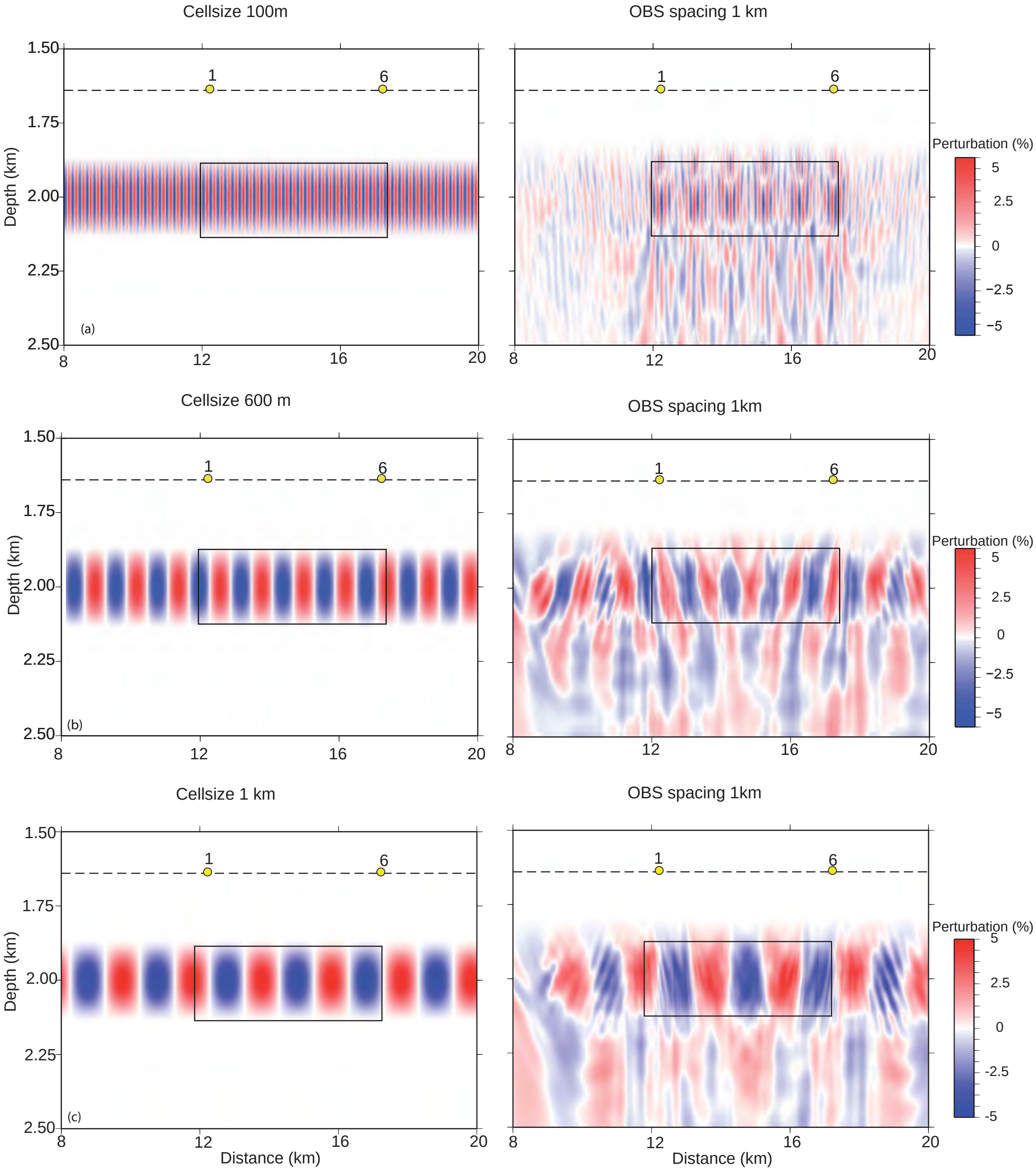

Fig. 4.16: Corrugation tests using (a) 100 m, (b) 600 m, and (c) 1 km cells with a ±80 m/s (5 %) velocity change of the low-velocity region (1.62 km/s) in a depth range of 1.9 to 2.2 km. The left plots show the target corrugation pattern with amplitude of ± 5 %, and the right plots show the success of the waveform inversion with 779 shots recorded on six 1-km-spaced OBSs.

positions. The 1-km-cell-size inversion shows that the cells could be recovered below the instruments positions (black box) and up to 3 km outside that range where the cells were slightly tilted (Fig. 4.16c). The comparison of all three model runs also shows that despite recovering the cell-pattern, the cell-amplitudes (perturbation size) were not fully recovered for 100-m spaced and 600-m spaced cells.

4.2.7 Misfit Evaluation

Within the inverse modeling the misfit value (objective function) between the modeled and original data was calculated in the frequency domain. We applied the phase-only waveform inversion to the synthetic OBS data, for which the calculated misfit is the imaginary part of the complex misfit function (for further details see *Kamei*, 2012). Since the frequencies are inverted sequentially one at the time, the objective function is calculated at the beginning of the inversion and after every iteration. Figure 4.17 shows the misfit reduction values for each iteration for each frequency in four different plots corresponding to the four different OBS spacings (100 m, 200 m, 500 m, and 1 km). The comparison shows that the misfit was already reduced by more than 90 % for the first frequency (2 Hz) for all OBS settings (Fig. 4.17). The misfit for all frequencies up to 10 Hz was reduced to below 50 %.

4.3 Waveform inversion of noisy OBS data from 2006

4.3.1 The starting model

The final travel-time tomography result (Fig. 3.10 - Chapter 3) obtained while inverting the 2006 OBS and 2-D SCS reflection data was taken as the starting model for the waveform inversion. The velocity model was extended from 12 km profile length to 30 km length to be comparable with the synthetic test shown earlier. The original model was placed in the middle of the 30 km profile and the OBS and shot positions were adjusted accordingly. The velocity model was smoothed using Seismic UNIX (SU) routines (Fig. 4.18). The maximum model depth was set to 3 km, which is slightly greater than the model depth of

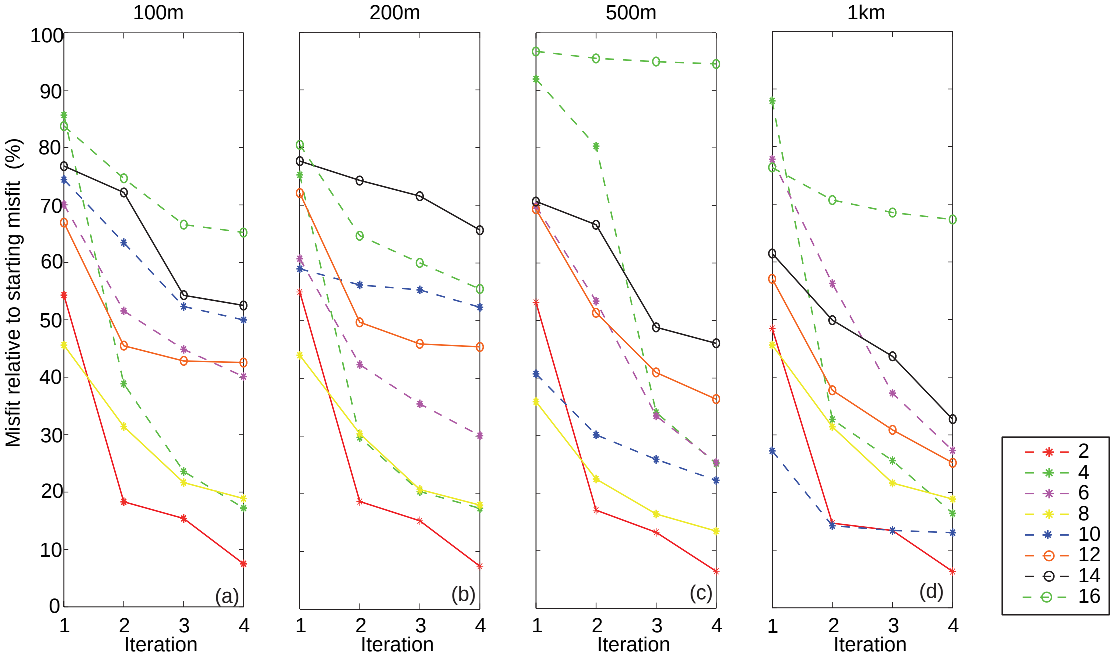

Fig. 4.17: Comparison of misfit as percentage of the starting misfit value after each iteration for a selection of frequencies for (a) 51 OBSs (100 m), (b) 26 OBSs (200 m), (c) 11 OBSs (500 m), and (d) 6 OBSs (1 km).

2.3 km of the travel-time inverse results (Fig. 3.10 - Chapter 3). Hence, a smooth velocity gradient from 1.9 km/s to 2.4 km/s was applied for the depth range below 2.3 km (Fig. 4.18).

4.3.2 The seismic source

The seismic source spectrum has a dominant frequency of 12 to 16 Hz, with a minimum frequency (30 dB down) of 5 Hz and a maximum frequency of 250 Hz. However, the main frequency content of the data including the refracted arrivals is concentrated at frequencies less than 25 Hz. Hence, a bandpass filter was applied to both receiver and source data (Fig. 4.19).

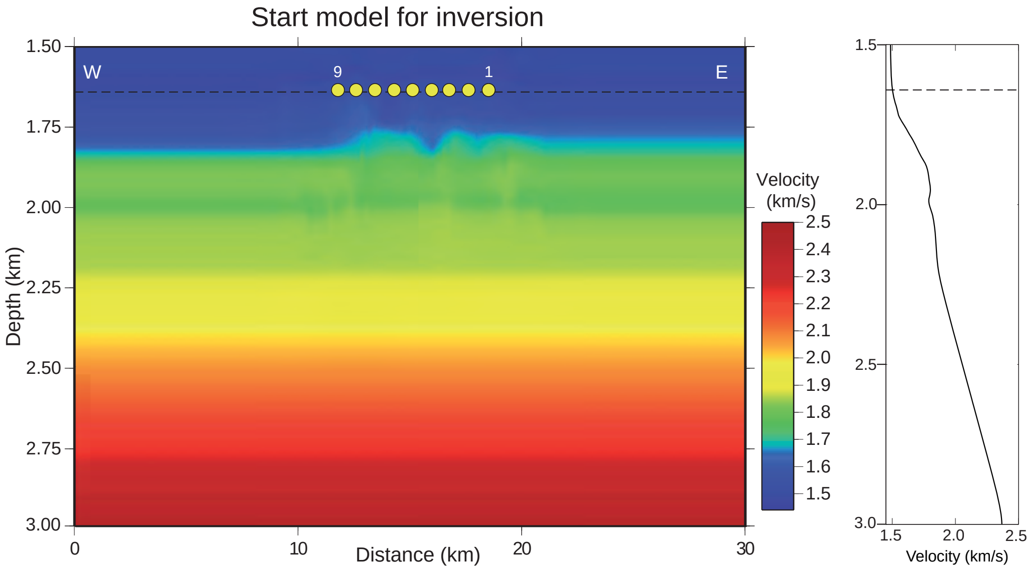

Fig. 4.18: The final velocity model from travel-time inversion of the 2006 data (Chapter 3; Fig. 3.10) was used as starting model for the waveform inversion. The velocity model was extended to 30 km profile length, where the original 12 km model was positioned in the middle of the profile. The model was smoothed and the average profile from the 2-D model is shown on the right.

4.3.3 Preconditioning of the observed 2006 OBS data

First, a reduction velocity of 1.9 km/s was applied to the 2006 data to identify the refracted arrivals more easily. The data were filtered with a bandpass up to 25 Hz according to the main frequency content in the data. The recorded trace-length of 8 s was reduced to 2 s as the main arrivals fall into that time-window. The amplitudes of all instruments were scaled trace-by-trace to the maximum amplitude of the OBS 2 data, on which the signal-to-noise ratio (S/N = 1.25) was the highest for refracted arrivals (Fig. 4.20- red boxes). All observed OBS data were muted to suppress most of the background noise and the multiple arrivals that were interfering with the first arrivals (Fig. 4.20). The time-mute was applied to a window of 300 ms above and below the first-arrivals including the refracted arrivals.

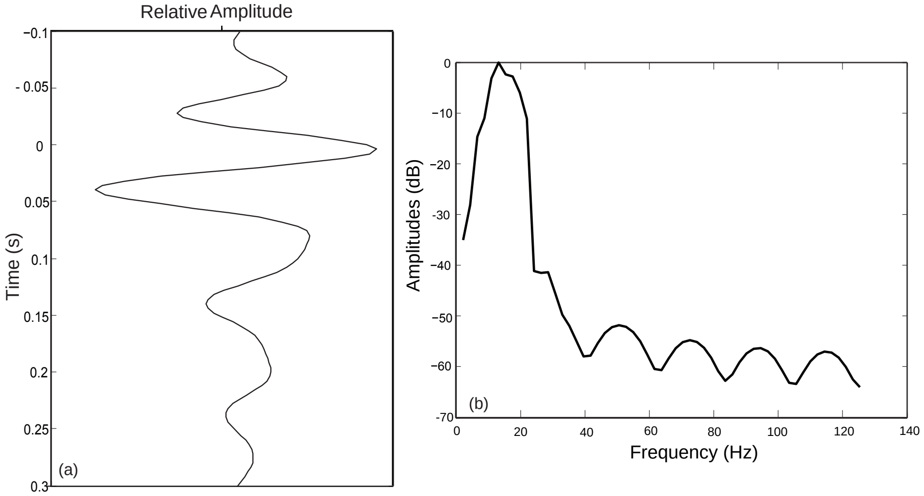

Fig. 4.19: (a) Seismic wavelet and (b) frequency spectrum of the GI gun array bandpass filtered to 25 Hz for waveform modeling.

4.3.4 Forward modeling

Synthetic seismic data were generated through a starting model based on the final travel-time inversion results, with the same geometry and source signature as used for recording the 2006 OBS data set. The objective was to refine the velocity model obtained in travel-time inversion and extend it to those regions where no ray-coverage or ray-tracing was achieved, e.g. the low velocity zone (LVZ) below the BSR. Forward modeling was carried out on 700 shots with a shot-spacing of ~15 m, and nine OBSs with an approximate instrument spacing of 900 m.

Similar to modeling the synthetic data described in the first part of this chapter, the forward modeling frequencies were chosen according to the Nyquist sampling theorem (Eq. 4.17) with a frequency sampling rate of Δf of 0.3 Hz for a total seismic record length of Tmax=3 s. The number of frequencies increased to 81 (0.3 to 24 Hz).

The first-arrival refractions are poorly visible in the 2006 OBS data (Fig. 4.21) due low signal-to-noise ratio (S/N = 1.25; 80 % noise). Ray-tracing was applied to identify the main arrivals in the seismic data (Fig. 4.21). The first refracted arrival with an apparent velocity

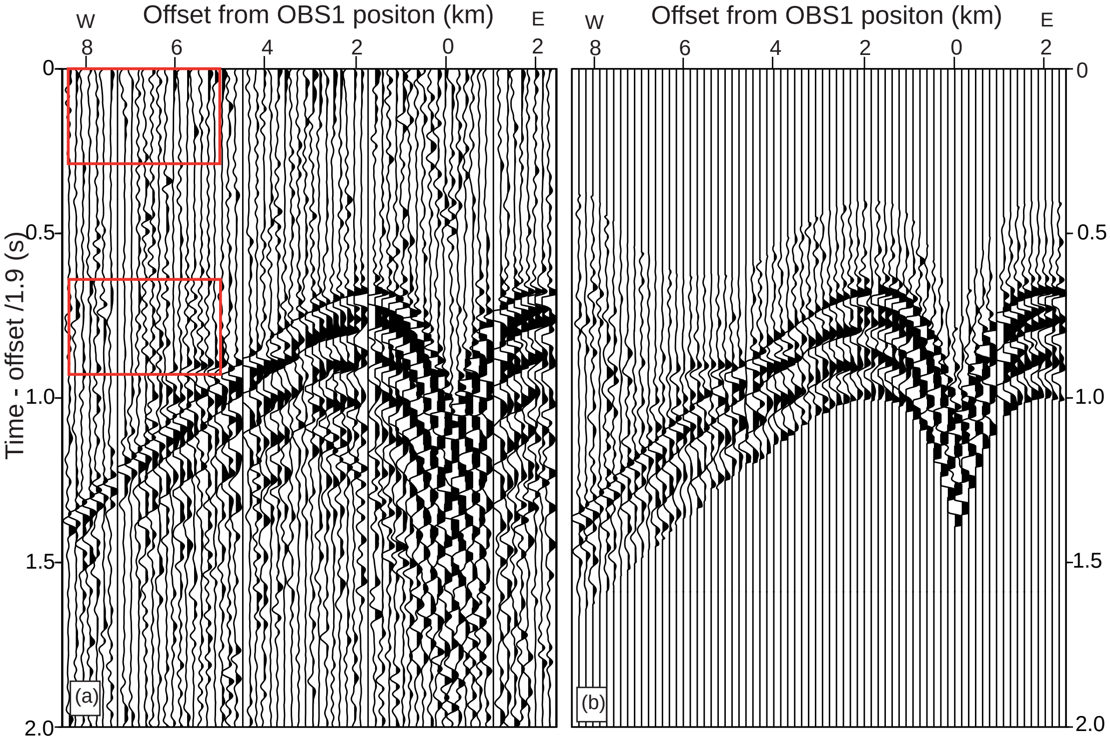

Fig. 4.20: Comparison of (a) original and (b) muted (300 ms above and below the first-arrivals) OBS 1 data. Bandpass filtering (7-25 Hz), re-sampling to 2 s, and amplitude scaling were applied on both data examples. Red boxes show the chosen amplitude ranges for estimating the S/N ratio for the refracted arrivals (S/N=1.25).

of 1.82 km/s was modeled at the top of the high velocity region. The secondary refracted arrival with an apparent velocity of ~2.4 km/s could not be modeled through ray-tracing as the origin is below the LVZ where no data constrains the depth of these arrivals. The multiple arrivals start below 2 s and were not used for the modeling approach.

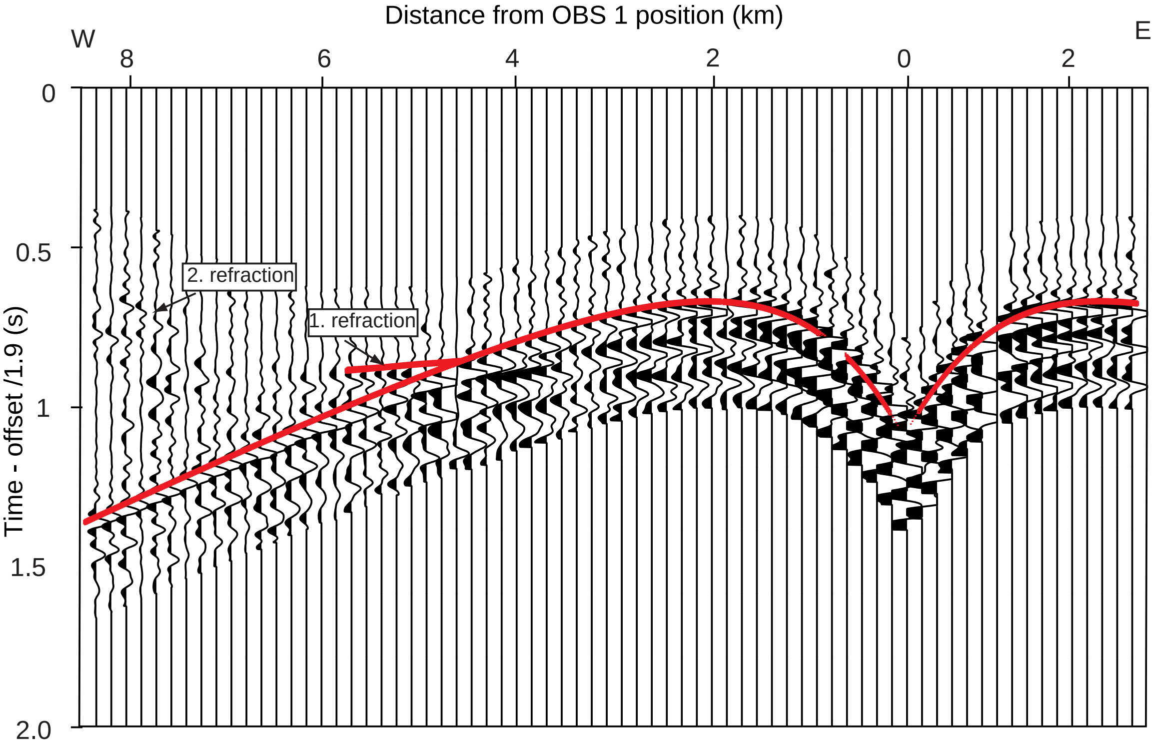

Fig. 4.21: Comparison of filtered (BP: 7-24 Hz) OBS 1 data and ray-traced arrivals. The refracted arrivals are indicated with numbers. The first refracted arrival (1.) was modeled for the top of the high velocity region with an apparent velocity of 1.82 km/s. The secondary refracted arrival was recognized on some OBSs (see chapter 3.2.3) and has an apparent velocity of 2.4 km/s. It was not modeled in the travel-time approach as the origin is deeper than the LVZ and no constraints on the depth were available. The seismic data are plotted with a reduced velocity of 1.9 km/s and multiple arrivals appear below 2 s.

The superposition of traces of the real filtered (BP: 7-24 Hz) OBS 2 data with the synthetic generated OBS 2 data (Fig. 4.22) using the final velocity model from the travel-time inversion (Fig. 4.18) shows that the first-arrival refractions are barely within 1/2 of the wavelength (*Pratt*, 1999). The refracted arrivals can be clearly seen in the forward modeled synthetic OBS data (black) emerging from the direct arrival at 5.4 km offset from the OBS 2 position (Fig. 4.22).

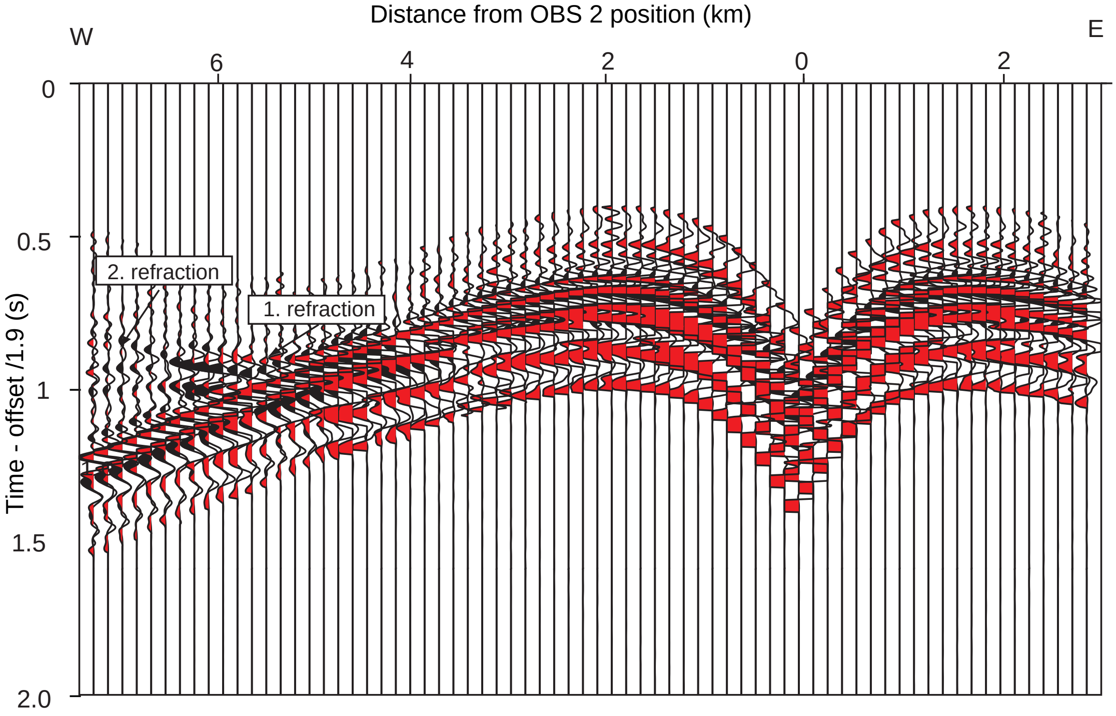

Fig. 4.22: Real (muted) OBS 2 data (red) were bandpass filtered to 24 Hz to be compared with the synthetic forward modeled data (black) generated with a starting model based on the final travel-time inversion results. The refracted arrivals (arrows) can be detected on some of the OBS data (1- refraction from top of high velocity region (v = 1.82 km/s); 2- refraction/turning wave from below the low velocity region (v ~2.4 km/s)). The first refracted arrival emerges from the direct arrival at ~5.2 km, but can be first clearly identified at 5.4 km offset on the synthetic data. The seismic data are displayed with a reduced velocity of 1.9 km/s.

4.3.5 Inverse modeling

The results from the synthetic modeling show that using the full range of frequencies according to the Nyquist sampling theorem is not necessary for a sufficient model update. Using the "effective" waveform method by *Sirgue and Pratt* (2004) and equations (4.22) and (4.27), a maximum shot-receiver offset of 9.3 km would result in a frequency selection of 8, 44, 247 Hz. Since 8 Hz is the lowest available frequency in the data, we followed a more conservative approach for the frequency selection for the inversion similar to that used in the synthetic modeling. The 17 selected frequencies range from 8 to 24 Hz with a frequency interval of 1 Hz. Studies by *Delescluse et al.* (2011) using only nine frequencies between 8 and 24 Hz with a frequency interval of 2 Hz have already shown the sufficiency of the selected frequencies for successfully updating the velocity model within the target region.

However, as mentioned in section 2.2, the observed 2006 OBS and 2-D SCS reflection data have high amplitude noise around 8 Hz. Thus frequencies lower than 8 Hz were not available for the inversion. The frequency domain data show that amplitudes of the lowest available frequencies (8 Hz, 9 Hz) are non-uniformly distributed over all the OBS data (Fig. 4.23 a). The maximum amplitudes are concentrated around the first two OBS positions between 11.25 km and 12.75 km of the profile length. For comparison, the frequency domain data for 12 and 15 Hz show that the amplitudes are equally distributed over a wide range of shots and receivers (Fig. 4.23 b), but the amplitude strength is weaker than for frequency data of 8 and 9 Hz. The high frequencies (18 Hz, 22 Hz) show a non-uniform amplitude distribution over the OBS data, but the amplitude values are smaller than those for the lowest frequencies (8, 9 Hz).

Since the gradient image is less reliable near the source and receiver locations due to singularities in the Green's functions (e.g. *Brenders and Pratt*, 2007a), the gradient had to be preconditioned. The gradient was tapered in depth to avoid singularities around the receiver locations.

The velocity model updates achieved after each frequency step were compared to the model updates from the previous frequency (Fig. 4.24). The inversion started with the lowest available frequency (8 Hz). Velocity irregularities, e.g, at 2.25 km depth, where the velocity has a minimum of 1.8 km/s for the center part of the OBS array (~15 km profile distance), show up already in the low frequency results. With increasing frequencies the amplitude of those anomalies is increasing. However, the target region of 2 km depth shows

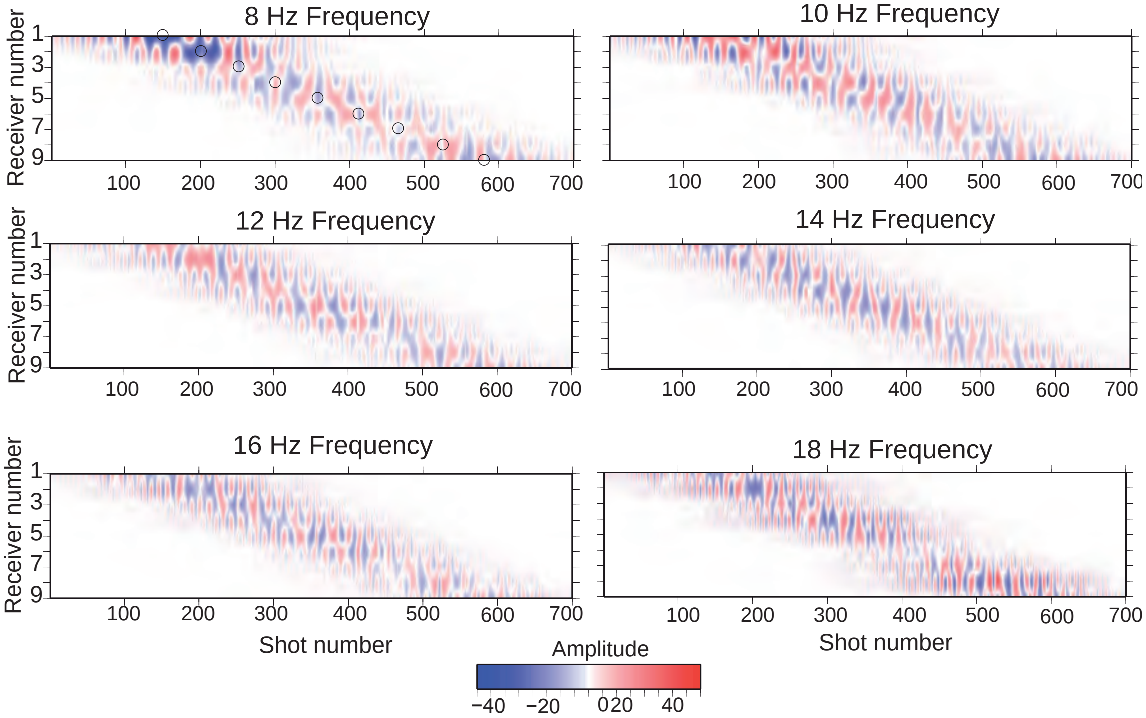

Fig. 4.23: Frequency domain data for (a) 8 Hz (a), (b) 10 Hz, (c) 12 Hz, (d) 14 Hz, (e) 16 Hz, and (f) 18 Hz extracted from the real OBS data. The lowest frequencies (a,b) that were used show a non-uniform distribution of the amplitudes with the highest peak around the first two OBSs. The black circles in (a) indicate the OBS positions along the shot profile.

no systematic velocity change, but only irregular fluctuations.

The final velocity model result (Fig 4.25) shows an increase in velocity in a region above (1.85 to 2.0 km - high-velocity zone (HVZ)) the LVZ. Vertical stripe structures similar to ray-paths can be seen in the model. The 2-D velocity model was averaged over a ten kilometer profile distance (10 to 20 km) and the resulting 1-D profile (blue) was compared with the averaged 1-D profile of the starting model (red - Fig. 4.25). The 1-D profiles also show the increase in velocity within the modeled HVZ. However, the inversion produced no velocity changes within the low velocity zone itself.

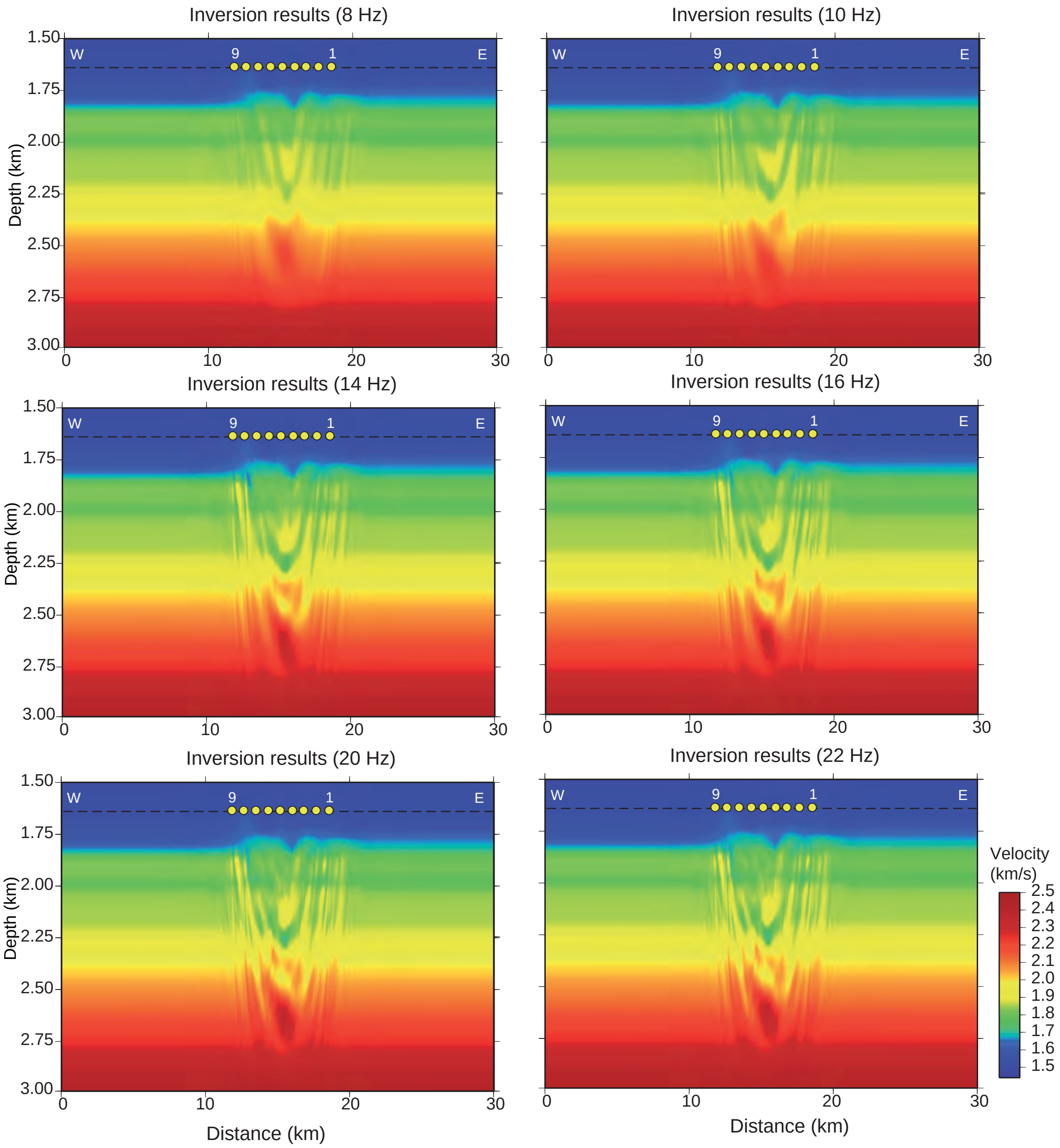

Fig. 4.24: Intermediate results for selected frequencies for the inversion on the 2006 OBS data using 16 frequencies between 8 and 24 Hz. The result from the previous frequency is used as a starting model for inverting the next frequency. The lowest available frequency was 8 Hz.

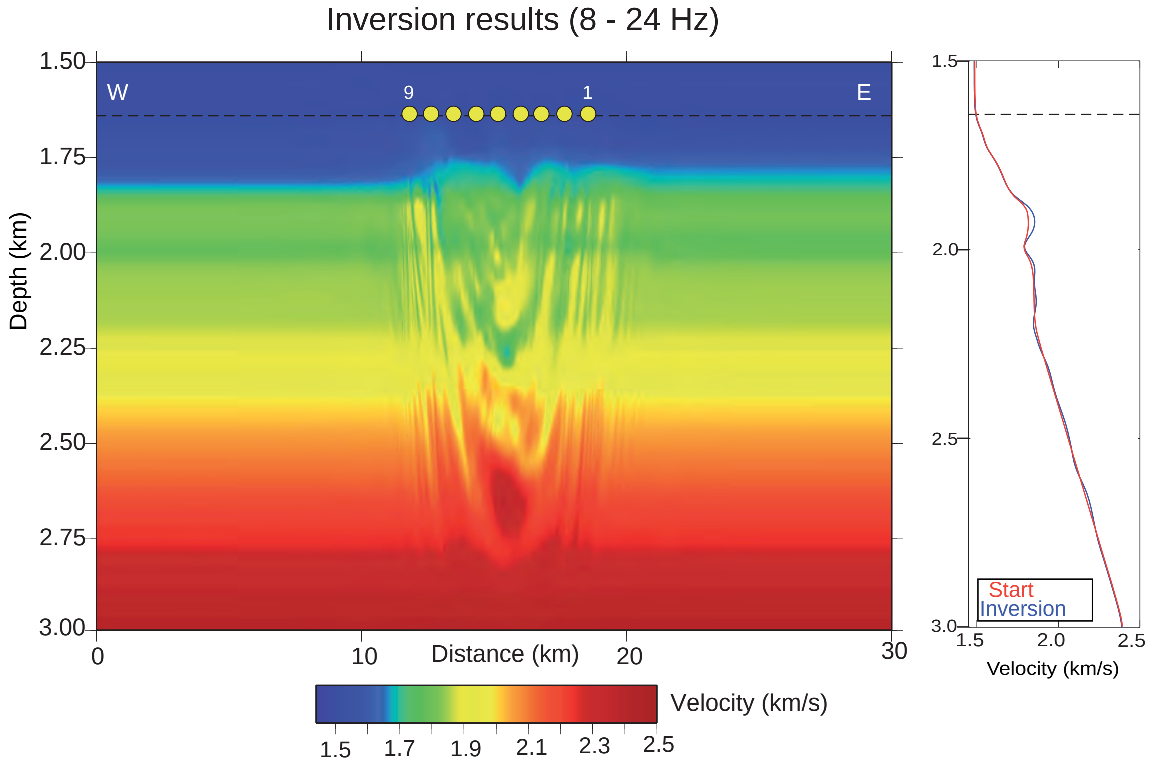

Fig. 4.25: Final velocity result of inverting 17 frequencies (8-24 Hz). It is clear from the intermediate results (Fig. 4.24) that the singularities appear early on in the inversion procedure and are significantly increasing with increasing frequencies. The target region (2 km depth) is hidden behind the artifacts introduced by the inversion.

4.3.6 Verification of inversion results

Similar to the synthetic modeling in the previous section of this chapter, the inversion results were verified with the generation of synthetic data using the final velocity model result. The observed seismic data and synthetic data are both limited to the frequency band of 8-24 Hz that was used for the inversion (Fig. 4.26). Compared to figure 4.22 the synthetic data are similar to the synthetic data of the starting model. However, the first-arrival refractions are barely within 1/2 wavelength of the original data.

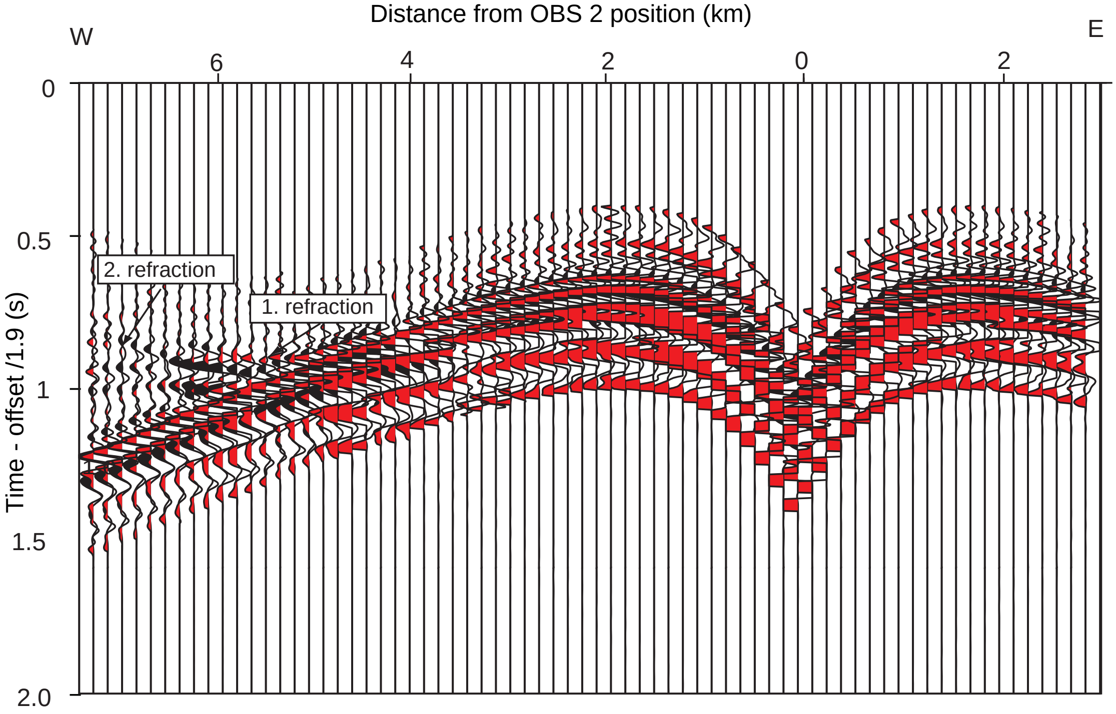

Fig. 4.26: (a) Comparison of observed (red) and modeled OBS 2 data (black) using the inversion result from the 2006 OBS data. The arrows show the refracted arrivals from the observed data.

4.4 Discussion

The modeling tests with synthetic seismic OBS data have shown three important results. First, an increase in instrument spacing leads to an increasing loss of the overall model smoothness within the target region (LVZ). The 1-km-spaced OBS that covers 5 km of profile distance recovers a 12 km wide low-velocity zone. However, the shot-receiver offsets have to be large enough (~12 km) to record the refracted arrivals from below the target region. Inversion with a smaller OBS spacing (100 m) shows that the recovered velocity structure is smoother than for the 1-km-spaced OBS array, but it requires almost ten times more instruments to recover the same profile distance (12 km).

Second, the OBS instrument spacing depends on the target dimensions. As the modeling tests show, seismic surveys using large instrument spacings ($\geq$ 500 m) have the advantage of covering a wide area with only a few instruments. However, the recognition of targets smaller than the size of the OBS spacing is difficult and ambiguous. Using smaller OBS spacings ($\leq 100\,\mathrm{m}$) has the advantage of resolving smaller target structures, but again a large number of instruments is required to cover an appropriate profile distance. The corrugation tests have shown that the half-width of the instrument spacing defines the lower boundary for lateral object resolution.

The third result shown by the modeling with synthetic OBS data is the effect of noise on data. A good signal-to-noise ratio (S/N=50; $2\,\%$ noise) already provides slightly different results compared to noise-free data. The study shows that noise levels of up to $10\,\%$ in the seismic data are tolerable for recovering the "true" velocity structure. However, lower S/N ratios are more common for marine seismic data, and the effect of that noise on the velocity result during the inversion will increase.

The main advantage of waveform inversion compared to travel-time inverse methods is definitely the recovery of the low-velocity region in the model. The LVZ was recovered during the inversion on all models where different OBS spacings where applied. The synthetic data generated with the original model clearly show arrivals from the bottom of the LVZ and from below the LVZ that could not be modeled with the ray-tracing approach. Hence, the waveform modeling approach adds significant information to the velocity model.

The inversion of real data is usually more complicated than an inversion of synthetic seismic data (e.g., as shown in *Brenders and Pratt*, 2007a). In this study the inversion of the 2006 OBS data shows that a number of factors play an important role in the outcome of the inversion. An averaged 1-D profile of the final velocity model (Fig. 4.25) shows a small model update within the target region of the high-to-low velocity contrast at 350 mbsf (1.95 km depth). However, the lateral velocity distribution of the final 2-D velocity model is non-uniform. The velocity structure is comparable with the final result of the synthetic modeling using 80 $\%$ of noise on the data (Fig. 4.14d). Within this velocity model result artificial structures were modeled that were probably matched to the noise signal rather than the real data signal.

The waveform modeling requires low frequencies for the background velocity model, while the higher frequencies refine the model and resolve small-scale structures. Within this study the lowest available frequency was only 8 Hz. However, other studies by *Delescluse et al.* (2011) and *Takam-Takougang and Calvert* (2011) have shown that starting with frequencies as "high" as 8 Hz will show an improvement of the velocity model if the starting velocity model is close to the true model. Comparisons of observed 2006 OBS data with the modeled OBS data using the starting model show that the first-arrival refractions are barely within 1/2 wavelength. This in turn means that the starting model for the inversion may not be close enough to the true model. The starting model of the 2006 OBS data lacks the large velocity contrasts that were expected for the base of the GHSZ and they cannot be modeled with the waveform approach.

Studies by *Brenders and Pratt* (2007b) and *Kamei et al.* (2012) have shown that careful gradient filtering applied within the individual model iterations can improve the final velocity smoothness. However, it is uncertain if the gradient filtering would improve the final modeling results of this study. The final gradient filter parameters are found after a number of time-consuming modeling tests as stated by*Kamei* (2012). Hence, we assume that the effects of the noisy data and the "poor" fit of the modeled data with the observed data due to the startmodel on the first inversion step are already greater than the effects of gradient filtering which would have to be applied to the modeling. *Kamei* (2012) also state that the smoothed gradient image has less resolution in the shallow subseafloor section (500 mbsf), which is our target region. However, the gradient was weighted in depth to avoid singularities at the near-seafloor locations within this study.

This results from this thesis chapter contribute to the knowledge of OBS survey requirements to investigate marine gas hydrate occurrences. The modeling of synthetic data has shown that it is possible to recover the low velocity region of a gas hydrate environment such as the passive Scotian margin. The modeling of the real OBS data from 2006 has shown that it is important to have a good S/N ratio in the data and a good starting model for the inversion. For future OBS surveys, four main factors should be considered: (1) the survey geometry (OBS spacing, shot-receiver offsets), (2) sufficient data quality (S/N ratio), (3) the available source frequency spectrum, and (4) the accuracy of the starting model.

5. CONCLUSIONS

The major focus of this thesis was to define the distribution of natural marine gas hydrates and free gas occurrences along the western/central Scotian slope. The velocity structure beneath the Scotian margin off eastern Canada was modeled in a travel-time inversion approach using ocean-bottom seismometer and single-channel seismic data. Careful analysis and modeling permitted the small velocity anomalies associated with low concentrations of gas hydrate and free gas to be resolved. Modeled velocity increases of 140 and 300 m/s for the 2006 and 2004 OBS array, respectively, correspond to gas hydrate concentrations of 2 to 18 %.

The geographical location of the OBS arrays to the Mohican channel plays an important role for the velocity model results. The 2004 OBS array, located east of the Mohican channel following a SW/NE direction along the channel wall, shows larger velocity values for the gas hydrate zone and therefore a larger estimate on gas hydrate concentration than the 2006 OBS array, which extends in a W/E direction away from the channel wall.

The OBS instrument spacings are different for the two studied data sets and the final velocity results show significant velocity differences for both data. The narrow 100-m-spaced OBS array from 2004 covers only 4 km of profile length, whereas the wider 900-m-spaced OBS array from 2006 covers 9 km of profile length. However, the modeled velocity for the 2004 data is more uniform along the profile distance than the velocity modeled with the 2006 data, where the velocity can vary with ~ 150 m/s laterally within one layer. Therefore, the lateral model resolution obtained with a smaller spaced OBS array is better due to more ray-coverage, than the resolution obtained while modeling with a larger OBS spacing.

Hence, not only the location of the OBS arrays plays a significant part in determining the free gas and gas hydrate concentration, but also the instrument spacing and therefore the ray-coverage between the individual instruments. Overall gas hydrate estimates from previous studies could be refined and substantiated within this thesis study and new insights into the distribution and restriction of gas hydrate occurrences are given.

The frequency-domain waveform inversion method applied to closely spaced (≤ 1 km) OBS data in this thesis study is the first of its kind to investigate marine natural gas hydrate occurrences. The waveform inverse modeling on synthetic generated OBS data has shown that the OBS instrument spacing is crucial for the velocity model results and the lateral resolution. The model smoothness and lateral resolution decreases with an increasing OBS instrument spacing. In general it can be said structures smaller than the half-width of the OBS spacing most likely cannot be resolved within the OBS survey. However, this is difficult to accomplish when the width of the target structure is unknown. Hence, within an OBS survey the number of OBSs and the smallest available spacing should be considered compared to the desired shot profile length. Instrument spacings smaller than 500 m and large numbers (20) of instruments are an appropriate choice when investigating shallow subseafloor ($<$500 mbsf) structures. For regions with low concentrations of gas hydrate or sparsely distributed gas hydrate occurrences those requirements are beneficial for a successful velocity analysis. The source spectrum is important for both travel-time and waveform inverse modeling. Low frequencies ($<$5-8 Hz) are crucial for obtaining arrivals from the deeper part of the velocity model that can be picked and applied in the travel-time inversion approach. The low frequencies also provide the background velocity model needed for the waveform inversion. A good signal-to-noise ratio is important for both identifying the seismic arrivals for travel-time inversion and for avoiding inversion on noise-artifacts in the waveform modeling. This thesis study shows that noise levels of up to 10 % are tolerable for recovering the velocity model in the waveform approach.

Recommendations for future work with ocean-bottom instruments

The OBS instrument spacing and shot-receiver offsets are crucial for gaining information from regions below the low-velocity zone. The travel-time inversion will benefit from using a smaller OBS spacing with a larger number of instruments. Based on several factors such as water depth, target dimensions, and seafloor morphology, the recommended ideal instrument spacing for the Scotian margin should be 100 m. However, this requires 100 instruments to cover the 10 km profile that was acquired with the 2006 OBS data. The study shows that larger spacings up to 500 m would be tolerable. However, the instrument type and the seismic source are an important factor in analyzing gas hydrates with low concentrations such as at this study site. A larger gun-volume would produce a larger signal strength, and would also contribute to a broader range of frequencies, especially adding more low frequencies into the data. The appearance of the BSR in the 3-D MCS reflection data (ENCANA Ltd.) shows that result. With lower frequencies in the OBS data the BSR would be more visible and the phase and amplitude of this reflection would contribute to the waveform modeling.

The incorporation of attenuation into the waveform modeling is inevitable for future work as studies by e.g., *Takam-Takougang and Calvert* (2011) and *Jaiswal et al.* (2012) have shown. The seismic amplitudes are sensitive to attenuation and are necessary to understand the complex gas hydrate and free gas system.

6. APPENDIX

6.1 Regional Geology

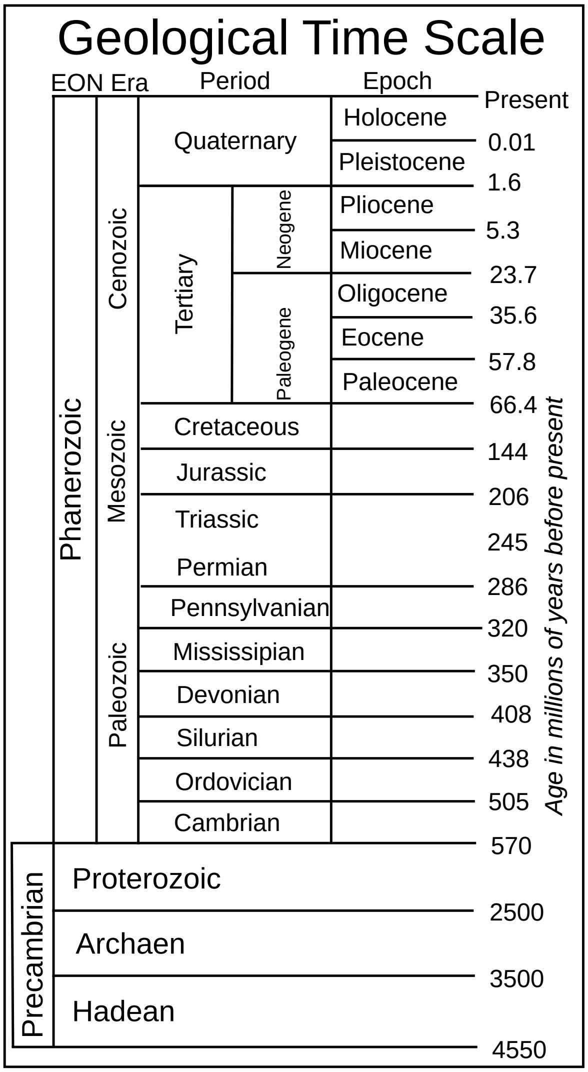

Fig. 6.1: Geological Timescale modified from U.S. Geological Survey 2012.

6.2 Seismic travel-time inversion

interface	data picks	pick uncert. (ms)	NTR	rms^a (ms)	χ^2
1	6300	1.5	11953	1.2	0.67
2	4622	2.0	18160	1.8	0.80
3	2805	2.5	15045	2.5	0.99
4	3091	2.5	16215	2.9	1.38
5	2118	2.5	14494	2.1	0.68
6	1768	2.5	13833	1.5	0.35
7	1953	2.5	14204	2.3	0.82
8	1972	2.5	14260	2.2	0.75
9	1058	2.5	12184	2.6	1.11

Tab. 6.1: Comparison of data input (picks) for travel-time inversion of the 2006 OBS data for different layers. (NTR - number of traced rays; a - rms: root-mean-square of travel-time residuals)

interface	data picks^a	pick uncert.^{b}	NTR	rms ^{c} (ms)	χ^2
1	6878	2.0	367526	1.5	0.75
2	5222	2.5	725370	2.3	1.02
3	3382	2.5	328021	2.8	1.10
4	3631	2.75	341177	3.0	1.38
5	2169	2.75	316638	3.9	1.83
6	2208	2.75	278658	4.2	2.00
7	2539	2.75	366889	3.7	1.68

Tab. 6.2: Comparison of data input for combined travel-time inversion of the 2006 OBS and vertical incidence data for different layers. (a - SCS data and OBS data combined; b - average uncertainty for SCS and OBS data; c - rms of combined residuals)

interface	av. pick uncert. (ms)	$^{(1)}$rms (ms)	$^{(2)}$rms (ms)	$^{(3)}\chi^2$	$^{(4)}\chi^2$
1	2.5	1.9	3.3	0.9	2.2
2	2.5	2.5	3.5	1.6	2.3
3	3.0	3.6	4.4	1.4	3.8
4	3.5	5.7	6.9	3.6	4.4
5	3.5	5.3	5.7	3.1	3.6
6	3.5	4.2	4.3	1.9	2.1
7	3.5	5.1	5.3	2.9	3.1
8	3.5	4.0	4.7	1.8	2.1

Tab. 6.3: Comparison of misfit values obtained for travel-time inversion with the 2004 OBS data and in a combined modeling with the vertical incidence data for different layers. The rms and χ^2 misfit values are shown for OBS data only (1,3) and in a combined modeling with the SCS data (2,4).

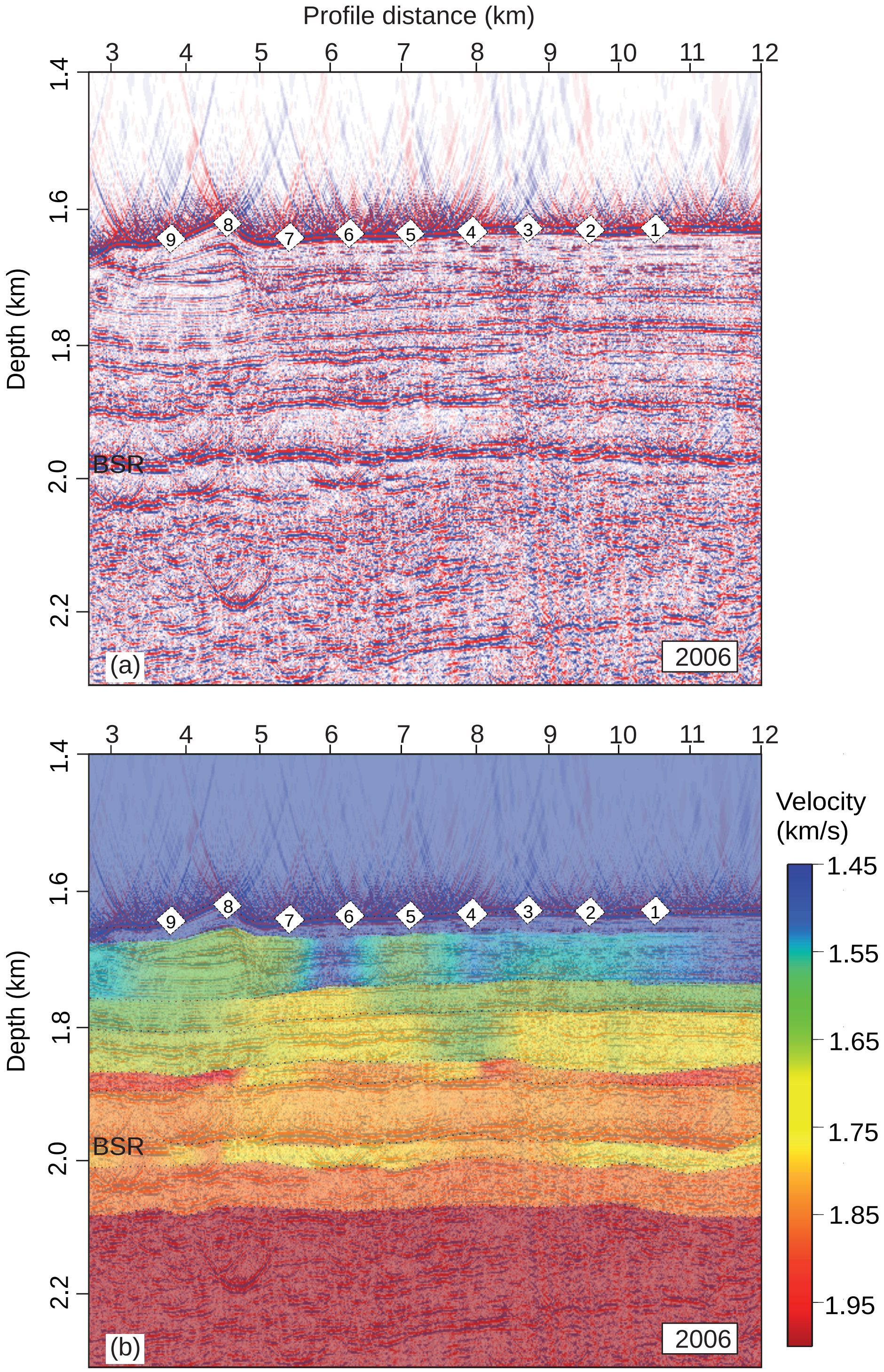

Fig. 6.2: (a) The 2006 2-D SCS reflection data (Fig. 2.7) was depth-migrated using the Finite-Difference migration algorithm and an average velocity-depth function from the 2006 travel-time inversion result. (b) Overlay of the 2006 2-D velocity model obtained from the travel-time inversion (Fig. 3.10) and migrated 2-D SCS section (a).

6.3 Waveform tomography

6.3.1 Definition of the eikonal equation and asymptotic ray-theory

The wave equation is defined as a pressure function U(**x**,t) of position and time:

$$\frac{\partial^2 U(\mathbf{x},t)}{\partial t^2} = c^2 \nabla^2 U(\mathbf{x},t) \tag{6.1}$$

and the Fourier transformation of this function into the frequency domain is:

$$-\omega^2 u(\mathbf{x},\omega) = c^2 \nabla^2 u(\mathbf{x},\omega) \tag{6.2}$$

The initial pulse is defined as a delta function:

$$U(\mathbf{x},t) = A(\mathbf{x})\delta(t - \tau(\mathbf{x})) \tag{6.3}$$

with the Fourier transform:

$$u(\mathbf{x},\omega) = A(\mathbf{x}) e^{i\omega\tau(\mathbf{x})} \tag{6.4}$$

Substitution of Eq. 6.4 into Eq. 6.2 and dividing by ω^2:

$$-Ae^{i\omega\tau} = c^2 [\frac{1}{\omega^2} \nabla^2 A + \frac{2i}{\omega} \nabla A \cdot \nabla\tau + \frac{iA}{\omega} \nabla^2 \tau - A \nabla\tau \cdot \nabla\tau] e^{i\omega\tau} \tag{6.5}$$

The key approximation is that the frequency ω approaches infinity or becomes very large. This assumption leads to the following result:

$$\boxed{\nabla\tau \cdot \nabla\tau = |\nabla\tau|^2 = \frac{1}{c^2}} \tag{6.6}$$

the **Eikonal equation**

6.3.2 Synthetic data generated with the original model and with a non-LVZ model

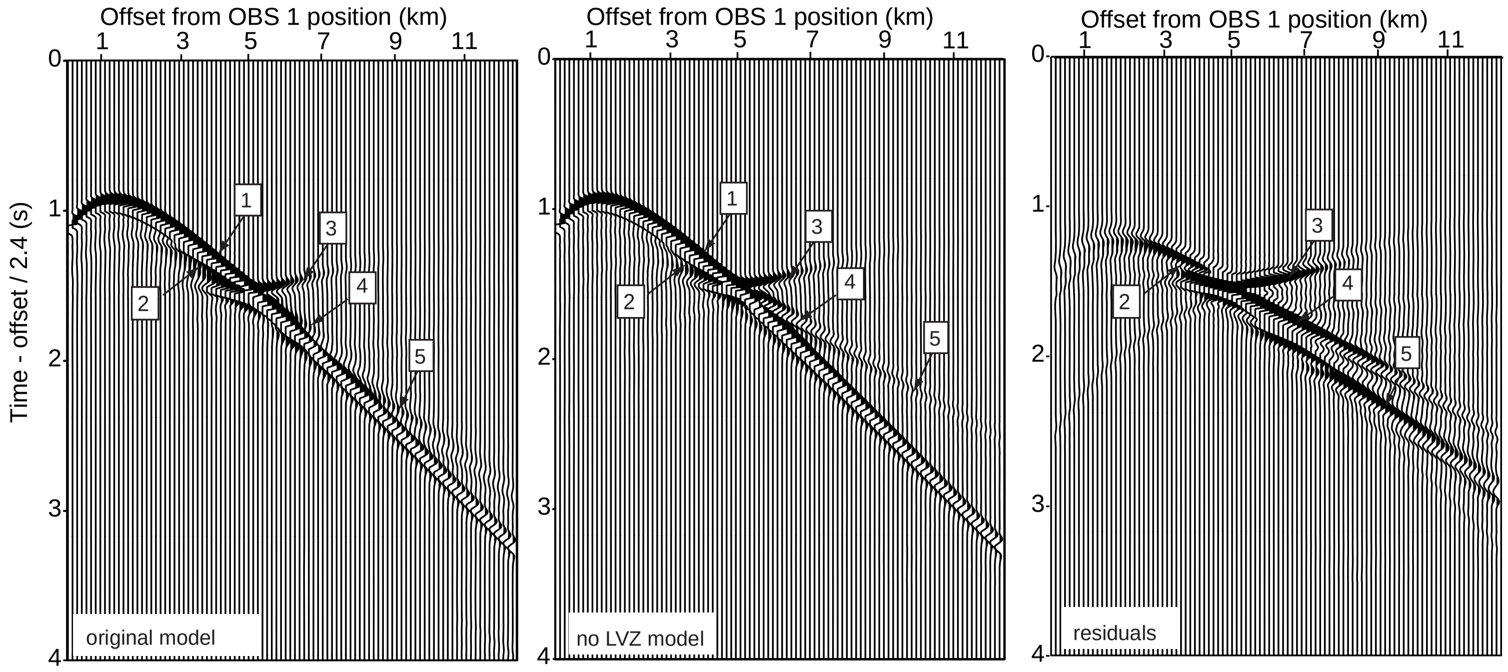

Fig. 6.3: Comparison of synthetic OBS 1 data for (a) the original model, (b) the model without a LVZ, and (c) the residuals of (a) and (b). The numbers refer to: (1) direct arrival, (2) refracted/reflected from top of LVZ, (3) turning wave arrivals from the deeper part of the model, (4) reflection from the bottom of the LVZ, (5) delayed arrival from the LVZ.

6.3.3 Different noise levels added to the synthetic data

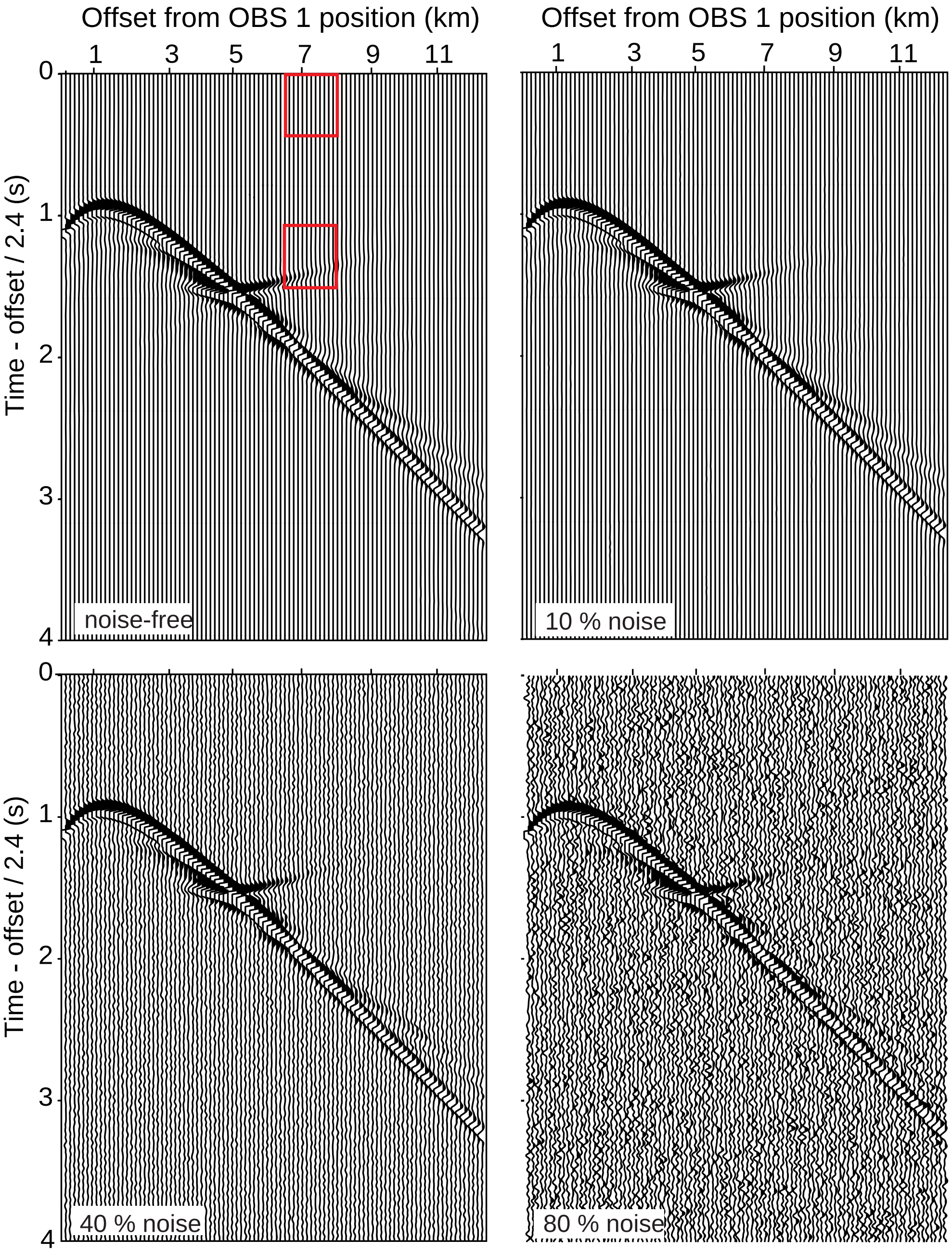

Fig. 6.4: Original synthetic data (a) noise-free, (b) with 10 %, (c) with 40 %, and (d) with 80 % additional noise. Red boxes show the chosen background amplitudes and signal amplitude values for the calculation of the S/N ratios that were applied.

6.3.4 Inversion results for different noise levels added to the 1-km-spaced synthetic data

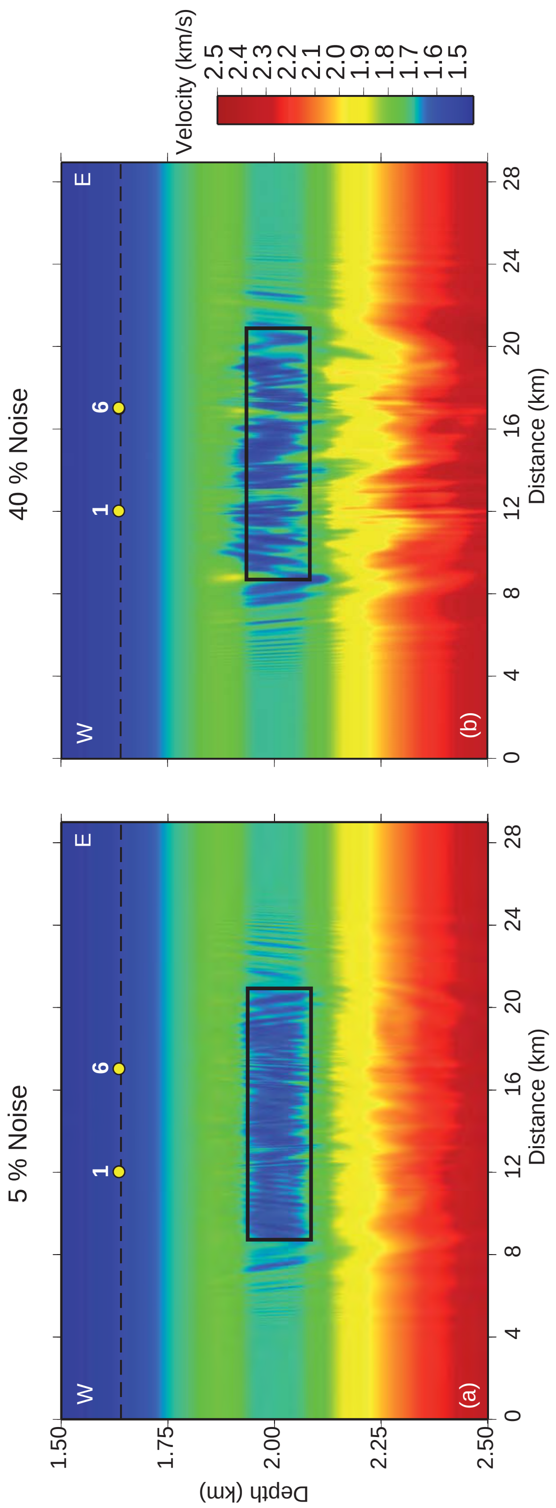

Fig. 6.5: Inversion results of the 1-km-spaced synthetic OBS data for the 6 OBSs with (a) 5 % and (b) 40 % additional noise on the data.

BIBLIOGRAPHY

Archer, D., The role of methane hydrates in the earth system: Burps of the depth or seductive irrelevance?, *National Energy Technology Laboratory (NETL- Fire in the Ice) Newsletter*, *August*, 12–14, 2010.

Archer, D., B. Buffett, and V. Brovkin, Ocean methane hydrates as a slow tipping point in the global carbon cycle, *Proceedings of the National Academy of Science of the United Stated of America*, *106*, 20,596–20,601, 2009.

Bennet, J., Near-surface faults on the Scotian Slope, eastern Canada, Master's thesis, Saint Mary's University, 2000.

Bleibinhaus, F., Application of full waveform tomography to active-source surface seismic data, in *Full seismic waveform modelling and inversion*, edited by K. Hutter, pp. 267–280, Springer, 2011.

Bleibinhaus, F., J. Hole, T. Ryberg, and G. Fuis, Structure of the California Coast Ranges and San Andreas Fault at SAFOD from seismic waveform inversion and reflection imaging, *Journal of Geophysical Research*, *112*, B06,315, 2007.

Bleibinhaus, F., J. Hole, and R. Lester, Applying waveform inversion to wide-angle seismic surveys, *Tectonophysics 472*, *472*, 238–248, 2009.

Boswell, R., and T. Collett, The Gas Hydrates Resource Pyramid, *U.S. DOE-NETL Fire in the Ice Newsletter*, *6*, 5–7, 2006.

Boswell, R., R. Hunter, T. Collett, S. Digert, S. Hancock, M. Weeks, and M. E. S. Team, In vestigation of gas hydrate-bearing sandstone reservoirs at the Mount Elbert stratigraphic test well, Milne Point, Alaska, in *Proceedings of the 6th International Conference on Gas Hydrates (ICGH 2008)*, 2008.

Brenders, A., and G. Pratt, Full Waveform Tomography for lithospheric imaging: Results from a blind test in a realistic crustal model, *Geophysical Journal International*, *168*, 133–151, 2007a.

Brenders, A., and G. Pratt, Efficient waveform tomography for lithospheric imaging: implications for realistic, two dimensional acquisition geometrie and low frequency data, *Geophysical Journal International*, *168*, 150–170, 2007b.

Brown, H., W. Holbrook, M. Hornbach, and J. Nealon, Slide structure and role of gas hydrate at the northern boundary of the Storegga Slide, offshore Norway, *Marine Geology*, *229 (3-4)*, 179–186, 2006.

Bunks, C., F. Saleck, S. Zaleski, and G. Chavent, Multiscale seismic waveform inversion, *Geophysics*, *60, No.5*, 1457–1473, 1995.

Campbell, D. C., The late Cretaceous and Cenozoic Geological History of the Outer Continental Margin off Nova Scotia, Canada: Insights ino the Margin Evolution from a Mature Passive Margin, Ph.D. thesis, Dalhousie University, Halifax, NS, Canada, 2011.

Campbell, D. C., D. Mosher, and J. W. Shimeld, Erosional unconformities, megaslumps and giant mud waves: insights into passive margin evolution from the continental slope off Nova Scotia, *Central and North American Conjugate Margins Conference: Rediscovering the Atlantic, New Winds from an Old Sea*, *4*, 37–41, 2010.

Cerveny, V., *Seismic Ray Theory*, Cambridge University Press, 2001.

Chand, S., T. A. Minshull, D. Gei, and J. Carcione, Elastic velocity models for gas-hydrate-bearing sediments - a comparison, *Geophysical Journal International*, *159*, 573–590, 2004.

Chapman, N., J. Gettrust, R. Walia, D. Hannay, G. D. Spence, W. T. Wood, and R. D. Hyndman, High resolution, deep towed, multichannel seismic survey of deep sea gas hydrates off western Canada, *Geophysics*, *67*, doi:10.1190/1.1500,364, 2002.

Claypool, G., and I. R. Kaplan, The origin and distribution of methane in marine sediment, in *Natural Gases in Marine Sediments*, edited by I. Kaplan, pp. 99–139, New York : Plenum, 1974.

Collett, T., R. Boswell, G. Guerin, S. Mrozewski, A. Cook, M. Frye, B. Shedd, R. Dufrene, P. Godfriaux, and D. McConnell, The National Methane Hydrates R&D Program 2009 Gulf of Mexico JIP Expedition, *Tech. rep.*, http://energy.usgs.gov/other/gashydrates/gulfmexico.html, 2009a.

Collett, T. S., Alaska north slope gas hydrate resources, *Tech. rep.*, U.S. Geological Survey, 2004.

Collett, T. S., M. Riedel, R. Boswell, J. cochran, P. Kumar, A. Sethi, A. Sathe, and N. E. . S. Party, International team completes landmark gas hydrate expedition in the offshore of India, *National Energy Technology Laboratory (NETL- Fire in the Ice) Newsletter*, *Fall*, 1–4, 2006.

Collett, T. S., A. H. Johnson, C. C. Knapp, and R. Boswell, Natural Gas Hydrates: A Review, in *Natural gas hydrates - Energy resource potential and associated geologic hazards*, edited by T. S. Collett, A. H. Johnson, C. C. Knapp, and R. Boswell, pp. p. 146 – 219., AAPG Memoir 89, 2009b.

Cullen, J., D. Mosher, and K. Louden, The Mohican channel gas hydrate zone, Scotian Slope, geophysical structure, in *Proceedings of the 6th International Conference on Gas Hydrates (ICGH 2008)*, 2008.

Dallimore, S., and T. Collett, Gas hydrates associated with deep permafrost in the Mackenzie Delta , N.W.T., Canada: Regional overview, in *Permafrost, Seventh international Conference, June 23 - 27. Yellowknife, Canada*, edited by A. Lewkowicz and M. Allard, pp. 196 – 206, Universite Laval, Collection Nordicana, 1998.

Dallimore, S., and T. Collett, Summary and implications of the Mallik 2002 gas hydrate production research well, in *Scientific results from the Mallik 2002 gas hydrate production research well, MacKenzie Delta, Northwest Territories, Canada*, edited by S. Dallimore and T. Collett, Bulletin of Geological Society of Canada,585, 2005.

Dallimore, S., T. Uchida, T. Collet, and et al., *Scientific results from JAPEX/JNOC/GSC Mallik 2L-38 Gas Hydrate Research Well, Mackenzie Delta, Northwest Territories, Canada*, Natural Resources Canda, GSC Bulletin 544, 1999.

Dallimore, S. R., J. F. Wright, F. M. Nixon, M. Kurihara, K. Yamamoto, T. Fujiii, K. Fujiii, M. Numasawa, M. Yasuda, and Y. Imasato, Geologic and porous media factors affecting the 2007 production response characteristics of the JOGMEC,NRCAN,AURORA Mallik Gas Hydrate Production Research Well, in *Proceedings of the 6th International Conference on Gas Hydrates (ICGH 2008)*, 2008.

Dash, R., and G. Spence, P-wave and S-wave velocity structure of northern Cascadia margin gas hydrates, *Geophysical Journal International*, *187*, 1363–1377, 2011.

Delescluse, M., M. Mnedimovic, and K. Louden, Case History 2-D waveform tomography applied to long-streamer MCS data from the Scotian Slope, *Geophysics*, *76*, B151–163, 2011.

Dillon, W. P., and M. D. Max, Oceanic gas hydrate, in *Natural Gas Hydrate in Oceanic and Permafrost Environments*, edited by M. Max, Kluwer Academic Publications, 2000.

Domenico, S. N., Effect of brine-gas mixture on velocity in an unconsolidated sand reservoir, *Geophysics*, *41*, 882–894, 1976.

Dvorkin, J., M. Prasad, A. Sakai, and D. Lavoie, Elasticity of marine sediments: Rock physics modeling, *Geophysical Research Letters*, *26(12)*, 1781 –1784, 1999.

Forster, P., and V. Ramaswamy, Changes in atmospheric constituents and in radiative forcing, in *Contribution of Working Group I to the Fourth Assessment Report of the Intergovernmental Panel on Climate Change, 2007*, edited by D. Q. M. M. Z. C. M. M. K. A. M. T. Solomon, S. and H. M. (eds.), pp. 129–235, Cambridge University Press, Cambridge, United Kingdom and New York, NY, USA., 2007.

Funk, T., R. Jackson, L. K.E., S. Dehler, and W. Yue, Crustal structure of the northern Nova Scotia rifted continental margin (eastern Canada), *Journal of Geophysical Research*, *109*, 2004.

Gauley, B.-J., Lithostratigraphy and sediment failure on the Central Scotian Slope, Master's thesis, Dalhousie University, Halifax, Nova Scotia, 2001.

Ginsburg, G. D., and V. A. Soloviev, Submarine gas hydrate estimation: Theoretical and empirical approaches, *Proceedings of the 27th Annual Offshore Technology Conference*, pp. 513–518, 1995.

Ginsburg, G. D., V. A. Soloviev, T. Matveeva, and I. Andreeva, Sediment grain-size control on gas hydrate presence, sites 994, 995, and 997., in *Proc. ODP, Sci. Results, 164: College Station, TX (Ocean Drilling Program)*, edited by C. K. Paull, R. Matsumoto, P. J. Wallace, and M. Dillon, pp. 237–245, 2000.

Grace, J., T. Collett, F. Colwell, P. Englezous, E. Jones, R. Mansell, P. Meekinson, R. Ommer, M. Pooladi-Darwisch, M. Riedel, J. Ripmeester, C. Shipp, and E. Willoughby, *Energy from Gas Hydrates: Assessing the opportunities and challenges for Canada*, Council of Canadian Academies, 2008.

Gray, W., and J. Golden, Velocity determination in a complex Earth, *Society of Exploration Geophysics (SEG) - Conference Paper*, 1983.

Grevemeyer, I., A. Rosenberger, and H. Villinger, Natural gas hydrates on the continental slope of Pakistan: constraints from seismic technics, *Geophysical Journal International*, *140*, 295–310, 2000.

Grist, A., P. Reynolds, M. Zentilli, and C. Beaumont, The Scotian Basin offshore Nova Scotia: thermal history and provenance of sandstones from apatite fission track and 40Ar/39Ar data, *Canadian Journal of Earth Sciences*, *29*, 16, 1991.

Haacke, R., G. Westbrook, and R. Hyndman, Gas hydrate, fluid flow and free gas: formation of the bottom-simulating reflector, *Earth and Planetary Science letters*, *261(3-4)*, 407–420, 2007.

Haacke, R., G. Westbrook, and M. Riley, Controls on the formation and stability of gas hydrate related bottom-simulating reflectors (BSRs): A case study from the west Svalbard continental slope, *Journal of Geophysical Research*, *113*, 17 pp, 2008.

Haeckel, M., E. Suess, K. Wallmann, and D. Rickert, Rising methane gas bubbles form massive hydrate layers at the seafloor, *Geochimica et Cosmochimica Acta*, *68(21)*, 4335–4345, 2004.

Hamilton, E., Geoacoustic modeling of the sea floor, *Journal of the Acoustical Society of America*, *68*, 1313–1340, 1980.

Hansen, D., J. Shimeld, M. Williamson, and H. Lykke-Andersen, Development of a major polygonal fault system in Upper Cretaceous chalk and Cenozoic mudrocks of the Sable Subbasin, Canadian Atlantic margin, *Marine and Petroleum Geology*, *21*, 1205–1219, 2004.

Helgerud, M., J. Dvorkin, A. Nur, A. Sakai, and T. Collett, Elastic-wave velocity in marine sediments with gas hydrates: Effective medium modeling, *Gephysical Research Letters*, *26(13)*, 2021–2024, 1999.

Helgerud, M., W. Waite, S. Kirby, and A. Nur, Measured temperature and pressure dependence of Vp and Vs in compacted, policrystalline sI methane and sII methane-ethane hydrate, *Canadian Journal of Physics*, *81*, 47–53, 2003.

Hicks, G., and R. Pratt, Reflection waveform inversion using local descent methods: Estimating attenuation and velocity over a gas-sand deposit, *Geophysics*, *66*, 598–612, 2001.

Holbrook, W., H. Hoskins, R. Wood, W.T.and Stephen, and L. D., Methane hydrate, bottom-simulating reflectors, and gas bubbles: Results of vertical seismic profiles on the Blake Ridge, *Science*, *273*, 1840–1843, 1996.

Hornbach, M., D. Saffer, W. Holbrook, H. Van Avendonk, and G. A.R., Three-dimensional seismic imaging of the Blake Ridge methane hydrate province: Evidence for large, concentrated zones of gas hydrate and morphologically driven advection, *Journal of Geophysical Research*, *113, B07101*, doi:10.1029/2007JB005,392, 2008.

Hovland, M., and J. Judd, Seabed pockmarks and seepages: Impact on geology, *Biology and Marine Environment*, *293*, 565, 1988.

Hyndman, R., and E. Davis, A mechanism for the formation of methane hydrate and seafloor bottom-simulating reflectors by vertical fluid expulsion, *Journal of Geophysical Research*, *97(B5)*, 7025–7041, 1992.

Hyndman, R., G. Moore, and K. Moran, Velocity, porosity, and pore-fluid loss from the Nankai subduction zone accretionary prism, in *Proceedings of the Ocean Drilling Program, Scientific Results, vol. 131, College Station, TX, pp. 211e220*, vol. 131, edited by I. A. Hill, A. Taira, and J. V. Firth, 1993.

Hyndman, R., G. Spence, N. Chapman, M. Riedel, and N. Edwards, Geophysical studies of marine gas hydrate in Northern Cascadia, *GEOPHYSICAL MONOGRAPH SERIES*, *124*, 273–295, 2001.

Jaiswal, P., P. Dewangan, T. Ramprasad, and C. Zelt, Seismic characterization of hydrates in faulted, fine-grained sediments of Krishna-Godavari Basin: Full waveform inversion, *Journal of Geophysical Research*, *117*, B10,305, 2012.

Jarrard, R., M. MacKay, G. Westbrook, and E. Screaton, Log-based porosity of ODP sites on the Cascadia accretionary prism, in *Proceedings of the Ocean Drilling Program,Scientific Results*, vol. 146, edited by B. Carson, G. K. Westbrook, R. J. Musgrave, and E. Suess, pp. 313 – 335, 1995.

Jo, C.-H., C. Shin, and J. Suh, An optimal 9-point, finite -difference, frequency space, 2-D scalar wave extrapolator, *Geophysics*, *61*, 529–537, 1996.

Kamei, R., Strategies for visco-acoustic waveform inversion in the Laplace-Fourier Domain, with application to the Nankai subduction zone, Ph.D. thesis, University of Western Ontario, 2012.

Kamei, R., G. Pratt, and T. Tsuji, Waveform tomography imaging of a megasplay fault system in the seismogenic Nankai subduction zone, *Earth and Planetary Science Letters*, *317-318*, 343–353, 2012.

Kastner, M., and I. MacDonald, Controls on gas hydrate formation and dissociation, Gulf of Mexico: In-Situ field study with laboratory characterizations of exposed and buried gas hydrates, *Tech. rep.*, US Department of Energy, National Energy Technology Laboratory (NETL), 2006.

Katzman, R., W. Holbrook, and C. Paull, Combined vertical-incidence and wide-angle seismic study of a gas hydrate zone, Blake Ridge, *Journal of Geophysical Research*, *99 (B9)*, 17,975–17,995, 1994.

Keen, M. J., and D. J. Piper, *Geology of the Continental Margin of Eastern Canada*, chap. Geological and Historical Perspective, pp. 5–30, Geological Survey of Canada, Geology of Canada, No.2, 1990.

Kennett, J., K. Cannariato, I. Hendry, and R. Behl, *Methane Hydrates in Quaternary Climate Change: The Clathrate Gun Hypothesis*, American Geophysical Union, 2003.

Korenaga, J., W. Holbrook, S. Singh, and T. Minshull, Natural gas hydrates on the southeast U.S. margin: Constraints from full waveform and travel time inversions of wide-angle seismic data, *Journal of Geophysical Research*, *102*, 15,345–15,365, 1997.

Kurihara, M., K. Funatsu, H. Ouchi, Y. Masuda, M. Yasuda, K. Yamamoto, M. Numasawa, T. Fujii, H. Narita, and J. F. Dallimore, S. R.and Wright, Analysis of the JOGMEC/NRCAN/AURORA MALLIK Gas Hydrate production test through numerical simulation, *Proceedings of the 6th International Conference on Gas Hydrates (ICGH 2008), Vancouver, British Columbia, CANADA, July 6-10, 2008*, 2008.

Kurihara, M., H. Ouchi, A. Sato, Y. Masuda, K. Yamamoto, S. Noguchi, and J. Nagao, Prediction of performances of Methane Hydrate production tests in the eastern Nankai Trough, 2011.

Kvenvolden, K. A., Methane hydrate - a major reservoir of carbon in the shallow geosphere?, *Chemical Geology*, *71*, 41–51, 1988.

LeBlanc, C., K. Louden, and D. Mosher, Gas hydrates off Eastern Canada: Velocity models from wide-angle seismic profiles on the Scotian Slope, *Marine and Petroleum Geology*, *24*, 321–335, 2007.

Lee, M., Elastic velocities of partially gas-saturated unconsolidated sediments, *Marine and Petroleum Geology*, *21*, 641–650, 2004.

Lee, M., Amplitude variation of bottom-simulating reflection with respect to frequency - transitional base or attenuation, *USGS Scientific Investigation Report*, *2007-5091*, 1–16, 2007.

Lee, M., D. Hutchinson, W. Dillon, J. Miller, W. Agena, and B. Swift, Method of estimating the amount of in-situ gas hydrates in deep marine sediments, *Marine and Petroleum Geology*, *10(5)*, 493–506, 1993.

Lee, S., Second Ulleung Basin gas hydrate expedition (UBGH2): Findings and implications, *USDOE-newsletter, Fire in the Ice, US Department of Energy, Office of Fossil Energy, National Energy Technology Laboratory,*, *1*, 5–9, 2011.

Lewis, J., and R. Hyndman, Oceanic heat flow measurements over the continental margins of eastern canada, *Canadian Journal of Earth Sciences*, *13(8)*, 1031–1038, 1976.

Liu, X., and P. Flemings, Dynamic multiphase flow model of hydrate formation in marine sediments, *Journal of Geophysical Research*, *112, B03101*, doi:10.1029/2005JB004,227, 2007.

Lopez, C., G. Spence, R. Hyndman, and D. Kelley, Frontal ridge slope failure at the northern Cascadia margin: Margin-normal fault and gas hydrate control, *Geology*, *38*, 967–970, 2010.

Majorowicz, J. A., and K. G. Osadetz, Gas hydrate distribution and volume in Canada, *AAPG Bulletin: Gas hydrates in Canada*, *85(7)*, 1211–1230, 2001.

Makogon, Y., *Hydrates of natural gas*, Penn Well Books,Tulsa, OK, 1981.

Makogon, Y. F., F. A. Trebin, A. A. Trofimuk, V. P. Tsarev, and N. V. Cherskiy, Detection of a pool of natural gas in a solid (hydrate gas) state, *Doklady Academy of Sciences U.S.S.R., Earth Science Section*, *196*, 197–200, 1972.

Malinverno, A., Marine gas hydrates in thin sand layers that soak up microbial methane, *Earth and Planetary Science Letters*, *292*, 399–408, 2010.

Malinverno, A., M. Kastner, M. Torres, and U. Wortmann, Gas hydrate occurrence from pore water chlorinity and downhole logs in a transect across the northern Cascadia margin (Integrated Ocean Drilling Program Expedition 311), *Journal of Geophysical Research*, *113,B08103*, doi:10.1029/2008JB005,702, 2008.

McGinnis, D. F., J. Greinert, Y. Artemov, S. E. Beaubien, and A. Wuest, Fate of rising methane bubbles in stratified waters: How much methane reaches the atmosphere?, *Journal of Geophysical Research*, *111*, 15 pp, 2006.

Micallef, A., C. Berndt, D. G. Masson, and D. A. Stow, Scale invariant characteristics of the Storegga Slide and implications for large-scale submarine mass movements, *Marine Geology*, *247*, 46–60, 2008.

Minshull, T. A., S. C. Singh, and G. K. Westbrook, Seismic velocity structure at a gas hydrate reflector, offshore western Columbia, from full waveform inversion, *Journal of Geophysical Research*, *99(B3)*, 4715–4743, 1994.

Mora, P. R., Nonlinear two-dimensional elastic inversion of multi-offset seismic data, *Geophysics*, *52*, 1211 – 1228, 1987.

Mosher, D. C., Hudson 2004-030 Cruise Report: July 10-20, 2004; Geological Survey of Canada, Open File, 72 p., *Tech. rep.*, Geological Survey of Canada (Atlantic); Dalhousie University, 2004.

Mosher, D. C., Bottom simulating reflectors on Canada's East Coast margin: Evidence for gas hydrate, in *Proceedings of the 6th International Conference on Gas Hydrates (ICGH 2008)*, 2008.

Mosher, D. C., A margin-wide BSR gas hydrate assessment: Canada's Atlantic margin, *Marine and Petroleum Geology*, *28*, 1540–1553, 2011.

Mosher, D. C., D. W. Piper, D. C. Campbell, and K. Jenner, Near surface geology and sediment failure geohazards of the Central Scotian Slope, *AAPG Bulletin*, *88(6)*, 703–723, 2004.

Mosher, D. C., K. Louden, C. LeBlanc, J. W. Shimeld, and K. Osadetz, Gas hydrate offshore eastern Canada - fuel for the future?, *OTC 17588 - Offshore Technology Conference. Houston, Tx. 2-5 May 2005.*, 2005.

Neave, K. G., Shallow seismic velocities on the eastern Grand Banks and Flemish Pass, *Unpublished report Prepared for Alan Judge of the Terrain Sciences Division, Geological Survey of Canada*, p. 19, 1990.

Nolet, G., Seismic wave propation and seismic tomography, in *Seismic Tomography*, pp. 1–23, Springer, 1987.

Operto, S., J. Virieux, J. Dessa, and G. Pascal, Crustal seismic imaging from multifold ocean bottom seismometer data by frequency domain full waveform tomography: application to the eastern Nankai trough, *Journal of Geophysical Research*, *111*, B09,306, 2006.

Ostrander, W. J., Plane-wave reflection coefficients for gas sands at nonnormal angles of incidence, *Geophysics*, *49 (10)*, 1637–1648, 1984.

Park, K. P., Gas hydrate exploration activities in Korea, in *Proceedings of the 6th International Conference on Gas Hydrates (ICGH 2008)*, p. 10 pp., 2008.

Paull, C. K., W. Ussler, and W. S. Borowski, Source of methane to form gas hydrates: in situ production or upward migration ?, in *Natural Gas Hydrates*, edited by E. D. Sloan, J. Happel, and M. A. Hnatow, pp. 392 – 409, N.Y. Academy of Sciences, 1994.

Paull, C. K., R. Matsumoto, P. J. Wallace, and et al., Proceedings ODP, Initial Reports, Leg 164, *Tech. rep.*, College Station, TX (Ocean Drilling Program), 1996.

Petersen, C., C. Papenberg, and D. Klaeschen, Local seismic quantification of gas hydrates and BSR characterization from multi-frequency OBS data at northern Hydrate Ridge, *Earth and Planetary Science Letters*, *255,Issues 3-4*, 414–431, 2007.

Piper, D. W., and W. Normak, Late Cenozoic sea level changes and the onset of glaciation: impact on continental slope propagation off eastern Canada, *Marine and Petroleum Geology*, *6*, 336–347, 1989.

Piper, D. W., P. J. Mudie, G. B. Fader, and J. H. W., Quaternary geology, in *Geology of the Continental Margin of Eastern Canada*, edited by M. J. Keen and G. L. Williams, pp. 475–607, Geological Survey of Canada, 1990.

Pohlman, J. W., E. A. Canuela, N. R. Chapman, G. D. Spence, M. J. Whiticar, and R. B. Coffin, The origin of thermogenic gas hydrates on the northern Cascadia Margin as inferred from isotopic (13C/12C and D/H) and molecular composition of hydrate and vent gas, *Organic Geochemistry*, *Stable isotope applications in methane cycle studies Volume 36*, 703–716, 2005.

Pratt, R. G., Seismic waveform inversion in the frequency domain: Part 1: Theory and verification in a physical scale model, *Geophysics*, *64*, 888–901, 1999.

Pratt, R. G., Waveform tomography - success, cautionary tales, and future directions, in *70th EAGE Conference and Exhibition, Rome, Italy, 9 to 12 June 2008*, 2008.

Pratt, R. G., and M. H. Worthington, The application of diffraction tomography to cross-hole seismic data, *Geophysics*, *53*, 1284–1294, 1988.

Pratt, R. G., and M. H. Worthington, Inverse theory applied to multi-source cross-hole tomography. part i: Acoustic wave-equation method, *Geophysical Prospecting*, *38*, 287–310, 1990.

Pratt, R. G., Z. M. Song, P. Williamson, and M. Warner, Two-dimensional velocity models from wide-angle seismic data by wavefield inversion, *Geophysical Journal International*, *124*, 323–340, 1996.

Ravaut, C., S. Operto, L. Improta, J. Virieux, A. Herrero, and D. Dell'Aversana, Multiscale imaging of complex structures from multifold wide-aperture seismic data by frequency-domain full- tomography: application to a thrust belt, *Geophysical Journal International*, *159*, 1032–1056, 2004.

Reagan, M. T., and G. M. Moridis, Dynamic response of oceanic hydrate deposits to ocean temperature change, *Journal of Geophysical Research*, *113, C12023*, 21 pp., 2008.

Riedel, M., T. S. Collett, M. J. Malone, and the Expedition 311 Scientists, Proceedings of the Integrated Ocean Drilling Program, *Technical report, IODP Management International Inc., Washington,*, *311*, DC, doi:10.2204/iodp.proc.311.2006., 2006a.

Riedel, M., I. Novosel, G. Spence, and R. Hyndman, Geophysical and geochemical signatures associated with gas hydrate-related venting in the northern Cascadia Margin, *Geological Society of America Bulletin*, *118*, 2006b.

Riedel, M., T. S. Collett, M. Malone, and the Expedition 311 Scientists, Expedition 311 synthesis: scientific findings., in *Proc. IODP, 311: Washington, DC (Integrated Ocean Driling Program Management International, Inc.)*, 2010.

Ripmeester, J. A., Hydrate research -from correlations to a knowledge-based discipline- the importance structure, in *Gas Hydrates - Challenges for the Future*, vol. 912, edited by G. D. Holder and P. R. Bishnoi, Annals New York Academy of Science, 2000.

Royden, L., and C. E. Keen, Rifting process and thermal evolution of the continental margin of Eastern Canada determined from subsidence curves, *Earth and Planetary Science Letters*, *51*, 343–361, 1980.

Rutqvist, J., and G. Moridis, Evaluation of geohazards of in-situ gas hydrates related to oil and gas operations, *National Energy Technology Laboratory (NETL- Fire in the Ice) Newsletter*, *August*, 2010.

Ryu, B., M. Riedel, J. Kim, R. D. Hyndman, Y. Lee, B. Chung, and I. Kim, Gas hydrates in the western deep-water Ulleung Basin, East Sea of Korea, *Marine and Petroleum Geology*, 2009.

Schlesinger, A., J. Cullen, G. Spence, R. Hyndman, K. Louden, and D. Mosher, Seismic velocities on the Nova Scotian margin to estimate gas hydrate and free gas concentrations, *Marine and Petroleum Geology*, *35, Issue 1*, 105–115, 2012.

Schoderbek, D., and R. Boswell, Ignik Sikumi -1, Gas Hydrate Test Well, Successfully Installed on the Alaska North Slope, *USDOE-NETL Fire in the Ice Newsletter*, *11*, 1–4, 2011.

Sheridan, R. E., Site 533 and 534 (leg 76), in *Proceedings of the Deep Sea Drilling Project, initial reports, v. 76, pages 35 - 80*, 1980.

Sheriff, R. E., *Encyclopedic Dictionary of Applied Geophysics*, Society Of Exploration Geophysicists, 2002.

Shimeld, J. W., D. C. Mosher, K. Louden, C. LeBlanc, and K. Osadetz, Bottom simulating reflectors and hydrate occurrences beneath the Scotian Slope, offshore eastern Canada, *AAPG Hedberg conference on "Gas Hydrates: Energy Resource Potential and Associated Geologic Hazards", September 12-16,2004 , Vancouver, BC, Canada*, p. 3, 2004.

Shin, C. S., Nonlinear elastic wave inversion by blocky parameterization, Ph.D. thesis, University of Tulsa, OK, 1988.

Shipp, R. M., and S. C. Singh, Two dimensional full wavefield inversion of wide aperture marine streamer data, *Geophysical Journal International*, *51*, 325–344, 2002.

Sirgue, L., Inversion de la forme d'onde dans le domaine frequentiel de donnees sismiques grands offsets, Ph.D. thesis, Queen's University, Canada, 2003.

Sirgue, L., and R. G. Pratt, Efficient waveform inversion and imaging: A strategy for selecting temporal frequencies, *Geophysics*, *69*, 231–248, 2004.

Sloan, E., Physical and chemical properties of gas hydrates and application to world margin stability and climate change, in *Gas hydrates: Relevance to world margin stability and climate change*, edited by J. P. Henriet and J. Mienert, pp. 31–50, Geological Society Special Publication Vol.137, 1998.

Spence, G. D., T. A. Minshull, and C. Fink, Seismic studies of methane gas hydrate offshore Vancouver Island, *Proceedings of the Ocean Drilling Program, Sci. Results*, *146*, 13–174, 1995.

Spence, G. D., R. R. Haacke, and R. D. Hyndman, Seismic indicators of natural gas hydrate and underlying free gas, *Society of Exploration Geophysicists*, *Special Volume*, 43, 2010.

Swift, S. A., Late Cretaceous-Cenozoic development of outer continental margin, southwestern Nova Scotia, *The American Association of Petroleum Geologists Bulletin*, *71(6)*, 678–701, 1987.

Takam-Takougang, E., Two-dimensional waveform tomography of the Queen Charlotte Basin of Western Canada and the Seattle Fault Zone, Ph.D. thesis, Simon Fraser University, 2011.

Takam-Takougang, E. M., and A. J. Calvert, Application of waveform tomography to marine seismic reflection data from the Queen Charlotte Basin of western Canada, *Geophysics*, *76*, B1–16, 2011.

Tarantola, A., Inversion of seismic reflection data in the acoustic approximation, *Geophysics*, *49(8)*, 1259–1266, 1984.

Trehu, A., G. Borhmann, F. Rack, M. Torres, and et al., Drilling gas hydrates on Hydrate Ridge, Cascadia continental margin, *Processdings of the Ocean Drilling Program, Initial Reports*, *204*, 2004.

Vidale, J. E., Finite-difference calculations of travel times in three dimensions, *Geophysics*, *55*, 1990.

Virieux, J., and S. Operto, An overview of full-waveform inversion in exploration geophysics, *Geophysics*, *74(6)*, WCC1–WCC26, 2009.

Wade, J. A., and B. C. MacLean, The geology of the southeastern margin of Canada, in *Geology of the continental margin of Eastern Canada*, edited by M. J. Keen and G. L. Williams, pp. 167–238, Geological Survey of Canada, Geology of Canada No.2, 1990.

Waite, W., M. B. Helgerud, A. Nur, J. C. Pinksto, L. Stern, and S. Kirby, Laboratory measurements of compressional and shear wave speeds through methane hydrate, in *Gas Hydrates: Challenges for the Future*, edited by G. D. Holder and P. R. Bishnoi, pp. 1003 – 1010, Annual . N.Y. Acad. Sci., 912, 2000.

White, M., Late Cenozoic seismic stratigraphy of the Mohican Channel area, Scotian Slope, Master's thesis, Dalhousie University Halifax, NS, Canada, 2005.

Williamson, P. R., A guide to the limits of the resolution imposed by scattering in ray tomography, *Geophysics*, *56*, 202–208, 1991.

Williamson, P. R., and M. H. Worthington, Resolution limits in ray tomography due to the wave behavior: Numerical experiments, *Geophysics*, *58*, 727–735, 1993.

Xu, W., and C. Ruppel, Predicting the occurrence, distribution, and evolution of methane gas hydrate in porous marine sediments from analytical models., *Journal of Geophysical Research*, *104*, 5081–5096, 1999.

Yuan, T., G. D. Spence, R. D. Hyndman, T. A. Minshull, and S. C. Singh, Seismic velocity studies of a gas hydrate Bottom-Simulating Reflector on the northern Cascadia continental margin: Amplitude modelling and full-waveform inversion, *Journal of Geophysical Research*, *104*, 11 pp., 1999.

Zelt, C. A., and P. J. Barton, Three dimensional seismic refraction tomography: A comparison of two methods applied to data from the Faroer Basin, *Journal of Geophysical Research*, *103*, 7187–7210, 1998.

Zelt, C. A., and R. B. Smith, Seismic traveltime inversion for 2-D crustal velocity structure, *Geophysical Journal International*, *108*, 16–34, 1992.

Zykov, M., 3-D travel time tomography of the gas hydate area offshore Vancouver Island based on OBS data, Ph.D. thesis, University of Victoria, BC, Canada, 2006.